Investigations of the υ_T=1 Exciton Superfluidic State in 2D Electron Bilayer Systems

**Von der Fakultät für Mathematik und Physik
der Universität Hannover
zur Erlangung des Grades
Doktor der Naturwissenschaften
- Dr. rer. nat. -
genehmigte Dissertation**

von

RODNEY DAVID WIERSMA

geboren am 9. Juni 1976 in Edmonton, Kanada

2006

Referent:	Prof. Dr. R. HAUG
Korreferent:	Prof. Dr. K. v. KLITZING
Tag der Promotion:	03.05.2006

Abstract

The question of the feasibility of a BEC of excitons in semiconductor systems was raised over 40 years ago by theoreticians [1, 2]. It was predicted that excitons due to their light mass should undergo condensation at temperatures of ~ 1 K, which is approximately 10^6 higher than the typical condensation temperature of more heavily alkali atom BECs ($T_c = 10^{-6}$ K). Two-dimensional bilayer systems in the quantum Hall regime have been predicted to be a suitable candidate for the formation of such an exciton condensate. Recent experiments in this area have led to some remarkable discoveries hinting towards exciton condensation. These include the observation of a zero interlayer bias Josephson like tunneling peak [3], the quantization of the Hall resistance in the drag layer [4], and possible excitonic flow in the counter-flow current configuration [5, 6, 7].

The focus of this thesis work is the investigation of this new ν_T=1 excitonic superfluidic state using two-dimensional bilayer electron systems. More specifically, this includes the reproduction of previous experimental claims and the further characterization of this relatively unknown bilayer quantum Hall state.

Bilayer systems consisting of two closely spaced GaAs quantum wells (QWs) separated by a high potential AlAs/GaAs superlattice barrier are grown using MBE techniques. Electrons supplied by Si-donor atoms located above and below the two QWs become trapped in the QWs leading to the formation of two 2DESs. These 2DESs show low intrinsic densities of n_s< 5.0×10^{10} cm^{-2} together with high mobilities of μ> 500000 $cm^2 V^{-1} s^{-1}$ at low temperatures (4.2 K). Selective area field gate depletion techniques [8, 9], using metallic top gates together with overgrown Si-doped GaAs back gates, allow for independent electrical contact to the individual 2DESs to be realized.

Interlayer tunneling conductance experiments are performed on a sample consisting of two 17 nm QWs separated by a 12.4 nm AlAs/GaAs superlattice barrier. The measured B= 0 T interlayer sample resistance is found to be several GΩ. No detectable resonance tunneling features at B= 0 T or at any other finite magnetic field value away from the ν_T=1 state is seen in the dI/dV vs. interlayer voltage measurements. Upon moving into the ν_T=1 state, for balanced layer electron densities, a large zero interlayer voltage tunneling peak suddenly emerges when d/ℓ_B is below a certain critical value, and increases in magnitude with lower d/ℓ_B ratios. This

is directly related to the coupled nature of the ν_T=1 state, where a positional uncertainty exists as to in which layer each electron is located.

Drag measurements are made by passing a current through one of the layers ("drive layer") and measuring the induced voltage drop in the other electrically isolated layer ("drag layer"). Upon entering in the vicinity of ν_T=1 state it is found that both the longitudinal $\rho_{drive,xx}$ and $\rho_{drag,xx}$ minima deepen, tending toward zero, and that the transverse component $\rho_{drive,xy}$ surprisingly drops down from the expected $\sim 2h/e^2$ to a quantization plateau of h/e^2. More surprisingly still is the sudden massive increase of the essentially zero Hall drag $\rho_{drag,xy}$ to a quantized value of h/e^2! This is claimed by theory to be a direct signature of the exciton condensate interlayer correlations [10, 11, 12, 13].

The asymmetric current configuration is probed by passing two oppositely directed currents of equal magnitude through the two layers. For matched layer electron densities the ν_T=1 state shows a pronounced minimum in ρ_{xx} while ρ_{xy} drops approximately to zero. Decreasing the d/ℓ_B ratio leads to a further deepening of the ρ_{xx} minimum and a widening of the zero in ρ_{xy}. Indeed, as previously observed [5, 6, 7], both the longitudinal and the Hall voltages in the layers tend to zero at the lowest experimental temperatures. The amazing disappearance of ρ_{xy} is credited to the formation of a neutral superfluid exciton condensate. Here the current is strictly carried by charge neutral interlayer excitons which are unaffected by the perpendicular magnetic field. Unlike the $\sigma \rightarrow 0$ conductivity intrinsic to the IQHE and FQHE states, the ν_T=1 state in the asymmetric current configuration indirectly points to a possible infinite conductivity $\sigma \rightarrow \infty$ as expected for a superfluid, since both ρ_{xx} and ρ_{xy} tend towards zero. This behavior is completely new to quantum Hall systems and has never been observed before.

Activation energies ($\Delta_{\nu=1}$) of the ν_T=1 state are obtained from temperature dependent measurements of the various resistivity components for two different type of bilayer samples consisting of 17 nm and 19 nm QWs, respectively. In all cases the activation energies shows a monotonous increase with decreasing d/ℓ_B below a certain $d/\ell_{B,crit}$ which is ~ 1.65 for the 17 nm QW sample and ~ 1.70 for the 19 nm QW sample. The activation energies for the 19 nm sample are approximately twice as large as seen in the 17 nm sample. This is quite surprising since the effective center-to-center QW spacing for the 17 nm and 19 nm samples are approximately the same (29.4 nm and 28.6 nm respectively) leading one to expect similar $\Delta_{\nu=1}$ vs. $d/\ell_{B,crit}$ behavior. Also for the 19 nm sample a saturation of $\Delta_{\nu=1}$ for d/ℓ_B below ~ 1.42 can be seen and may indicate a fully developed ν_T=1 state. For the 17 nm we have determined activation energies for transport in the balanced ν_T=1 state over a wide range of the coupling parameter d/ℓ_B for both the drag and counter-flow configurations. Here the activation energies obtained in the different configurations are approximately equal and increase monotonously with increasing coupling below d/l$_B$=1.64.

A phase diagram between the weakly coupled (ν_U=1/2, ν_L=1/2) phase and the strongly

coupled ν_T=1 phase is experimentally made as a function of d/ℓ_B vs. imbalance Δn ($\equiv[n_L$-$n_U]/n_T$). In the drag configuration, the transverse resistivity components at higher d/ℓ_B values reveal $\rho_{drive,xy}$ being $\approx 2h/e^2$ and $\rho_{drag,xy}$ being essentially zero as expected for two completely independent layers at ν=1/2. Moving to lower d/ℓ_B values, a phase transition from the weakly coupled phase to the strongly coupled ν_T=1 phase is seen to occur. Upon crossing this phase boundary, the ν_T=1 phase quickly strengthens with decreasing d/ℓ_B and the transverse resistivities of both $\rho_{drive,xy}$ and $\rho_{drag,xy}$ reach a quantized value of h/e^2. Moving away from the balanced electron density case towards imbalanced electron layer densities, drag measurements reveal that small interlayer balances lead to a strengthening of the excitonic phase. This is particulary apparent in the $\rho_{drag,xy}$ data where, even if one is not initially in the strongly correlated phase, it is possible to induce the ν_T=1 phase by imbalancing the system.

In the symmetrically imbalanced case, an asymmetry in the activation energies, $\Delta_{\nu=1}$, of the separate layers making up the ν_T=1 state is observed. In each layer, this activation energy increases approximately linearly with increasing the density of the respective layer. It indicates that the measured activation energies do not reflect the condensation energy of the excitonic state nor the binding energy of the excitons, both of which should be independent on whether it is measured in the upper layer or in the lower layer. Instead, it implies that the activation energy reflects a gap to charge-excitations in the *separate* layers that form the bilayer condensate and that the excitation spectrum of a layer is substantially different for positive and negative imbalance. As in the $\Delta_{\nu=1}$ vs. d/ℓ_B case, we find that with imbalance the activation energies obtained in the drag and counter-flow configurations are again approximately equal.

It has been speculated that the quantized Hall drag of h/e^2 observed for the ν_T=1 state may be used to construct a novel DC step-up voltage transformer [14, 15]. This work presents the first experimental attempt to produce such a device. Upon separating the upper 2DES into two regions through the use of a plunger gate it is found that in the ν_T=1 state the induced Hall drag voltage in the secondary layer (V_2) can be stepped up to approximately $V_2 = 2I_1h/e^2$ where I_1 is a current sent through the primary layer.

Zusammenfassung

Bereits Mitte des letzten Jahrhunderts befassten sich Theoretiker mit der Möglichkeit eines Bose-Einstein-Kondensates aus Exzitonen in Halbleitersystemen [1, 2]. Es wurde vorausgesagt, dass Exzitonen aufgrund ihrer geringen Masse bereits bei Temperaturen um 1 K in die kondensierte Phase übergehen sollten. Bei Temperaturen also, die 10^6 höher sind als bei Bose-Einstein-Kondensaten ($T_c = 10^{-6}$ K) aus den viel schwereren Alkali-Atomen.

Zwei-dimensionale Doppellagen Systeme im Bereich den Quanten-Hall-Effektes wurden u.a. als mögliche Kandidaten für solch ein Exziton-Kondensat vorgeschlagen und tatsächlich haben Experimente Anzeichen für ein Bose-Einstein-Kondensat liefern können. Zu den Beobachtungen gehören u.a. das Vorhandensein eines Maximums in der Tunnelleitfähigkeit um 0V, welches an den Josephson-Effekt erinnert [3], die Quantisierung des Hall-Widerstandes in der Drag-Schicht [4] und das Verschwinden des Hallwiderstandes in der Gegenstrom Konfiguration (Counterflow), der als Fluss von Exzitonen interpretiert wird [5,6,7].

Der Fokus dieser Dissertation ist die Untersuchung dieses neuartigen ν_T=1 exzitonischen superfluiden Zustandes mit Hilfe von zwei-dimensionalen Elektron-Doppellagensystemen. Im speziellen wurde versucht, vorherige experimentelle Beobachtungen zu bestätigen, sowie diesen bisher relativ unverstandenen Doppellagen-Quanten-Hall Effekt weiter zu charakterisieren.

Doppellagen-Systeme werden mittels MBE Technologie hergestellt und bestehen aus zwei dicht-angrenzenden GaAs Potentialtöpfen (quantum wells), getrennt durch ein AlAs/GaAs Übergitter als Barriere mit geringer Tunnelrate. Die Erzeugung der beiden zwei-dimensionalen Elektronengasen wird ermöglicht durch Si-Donatoratome, die sich in der Nähe der Potentialtöpfe befinden.

Die beiden zwei-dimensionalen Elektronengase besitzen eine intrinsische Elektronendichte von n_s< 5.0×10^{10} cm^{-2} in Verbindung mit hohen Mobilitäten von μ> 500000 $cm^2 V^{-1} s^{-1}$ bei Temperaturen von 4.2K. Die unabhängige Kontaktierung der beiden Elektronengase wird mittels des "selektiven Verarmungsprinzips" gewährleistet [8, 9], das metallische "top gates" und überwachsene Si-dotierte GaAs "back gates" verwendet.

Interlagen-Tunnelexperimente wurden an einer Probe mit 17nm breiten Potentialtöpfen, getrennt durch eine 12.4 nm AlAs/GaAs Barriere, durchgeführt. Der gemessenen Interlagen-Widerstand bei nicht vorhandenem Magnetfeld betrug mehrere GΩ. Es konnte kein Hinweis

auf resonantes Tunneln bei den Tunnelleitfähigkeitsmessungen bei B= 0 T oder irgendeinem anderen Magnetfeld um ν_T=1 gefunden werden. Bei Annäherung an den ν_T=1 Zustand konnte für gleiche Elektronendichten in beiden Lagen (matched densities) ein riesiges Maximum um 0V in der Interlagentunnelleitfähigkeit gefunden werden, das allerdings erst auftritt, wenn d/ℓ_B unter einen kritischen Wert fällt und das an Intensität zunimmt, sobald d/ℓ_B weiter verringert wird. Diese Beobachtung ist direkt mit starken Korrelation und der Ortsunsicherheit des Elektronenzustandes im ν_T=1 Zustand verknüpft.

"Drag"- Messungen wurden durchgeführt, indem der Spannungsabfall an einer nicht-stromführenden Schicht (Drag Layer) gemessen wurde, die elektrisch von der stromführenden Schicht (Drive Layer) getrennt ist. Bei Annäherung an den ν_T=1 Zustand konnte beobachtet werden, wie sowohl die Minima im Longitudinalwiderstand ($\rho_{drive,xx}$ und $\rho_{drag,xx}$) ausgeprägter wurden bzw. gegen Null tendierten als auch der Transversale-(Hall-)Widerstand $\rho_{drive,xy}$ vom erwarteten Wert $\sim 2h/e^2$ auf ein quantisiertes Plateau von h/e^2 abnahm. Überraschender ist allerdings die plötzliche Zunahme des Hall-"Drags" $\rho_{drag,xy}$ von annähernd Null auf einen quantisierten Wert von h/e^2! Dieses Verhalten wird in theoretischen Betrachtungen als direkter Nachweis eines Interlagen-Exziton Kondensates anführt [10, 11, 12, 13].

Werden zwei entgegengesetzte Ströme gleicher Stärke durch die beiden Lagen geschickt (Counterflow), kann bei gleichen Elektronendichten in der Umgebung von ν_T=1 ein ausgeprägtes Minimum bei ρ_{xx}, sowie ein nahezu vollständiges Verschwinden von ρ_{xy} beobachtet werden. Mit Abnahme von d/ℓ_B reduziert sich das Minimum von ρ_{xx} weiter und das Minimum von ρ_{xy} wird ausgeprägter. Es konnte also tatsächlich bestätigt werden [5, 6, 7], dass sowohl die Longitudinal- als auch die Hall-Spannungen bei den niedrigsten erreichbaren Temperaturen gegen Null tendieren. Die verblüffende Tatsache, dass ρ_{xy} verschwindend geringe Werte annimmt, wird der Bildung eines neutralen superfluiden Exzitonen-Kondensates zugeschrieben. In diesem Zustand besteht der Strom ausschließlich aus ladungsneutralen Interlagen-Exzitonen, welche von dem senkrechten Magnetfeld nicht beeinflusst werden. Im Gegensatz zur $\sigma \rightarrow 0$ Leitfähigkeit, welche eine intrinsische Eigenschaft des ganz- und gebrochenzahligen Quanten-Hall-Effektes ist, deutet das Verhalten des ν_T=1 Zustandes bei entgegengesetzten Strömen auf eine unendliche Leitfähigkeit $\sigma \rightarrow \infty$ hin, wie sie für ein Superfluid erwartet wird, da in diesem Fall ρ_{xx} und ρ_{xy} gegen Null tendieren. Dieses Verhalten ist völlig neuartig in Quanten-Hall Systemen und konnte bisher nicht beobachtet werden.

Aktivierungsenergien ($\Delta_{\nu=1}$) des ν_T=1 Zustandes konnten aus den spezifischen Widerständen mit Hilfe temperaturabhängiger Messungen für zwei Doppellagensysteme mit 17 nm und 19 nm breiten Potentialtöpfen berechnet werden. In beiden Fällen zeigten die Aktivierungsenergien einen monotonen Anstieg bei abnehmendem d/ℓ_B, sobald ein bestimmten $d/\ell_{B,crit}$ unterschritten wurde. Dieser kritische Wert betrug ~ 1.65 bei der Probe mit dem 17 nm breiten Potentialtopf und ~ 1.70 bei der Probe mit dem 19 nm breiten Potentialtopf. Die Ak-

tivierungsenergien bei der 19nm Probe sind ungefähr zweimal so groß wie bei der 17 nm Probe. Dies ist ziemlich überraschend, da der effektive Abstand zwischen den Zentren der Potentialtöpfe für beide Proben ungefähr gleich ist (29.4 nm und 28.6 nm). Daher sollte man auch ein ähnliches $\Delta_{\nu=1}$ vs. $d/\ell_{B,crit}$ Verhalten erwarten. Hinzu kommt, dass für die 19nm Probe eine Sättigung von $\Delta_{\nu=1}$ für d/ℓ_B unterhalb von ~ 1.42 auftritt, was man als einen voll ausgeprägten $\nu_T=1$ Zustand deuten könnte. Für die 17nm Probe konnten wir die Aktivierungsenergien über einen großen Bereich des Kopplungsparameters d/ℓ_B in der Drag- und Counterflow-Konfiguration aus Transportmessungen (bei gleichen Dichten in beiden Lagen) bestimmen. Die Aktivierungsenergien sind hierbei für die verschiedenen Konfigurationen vergleichbar und steigen monoton bei Erhöhung der Kopplungsstärke unterhalb von d/l$_B$=1.64 an.

Experimentell konnte ein eindrucksvolles Phasendiagramm (d/ℓ_B gegen Ungleichgewichtzustände der Dichten Δn ($\equiv[n_L-n_U]/n_T$)) erstellt werden, welches den Übergang zwischen der schwach-gekoppelten ($\nu_U=1/2$, $\nu_L=1/2$) Phase und der stark-gekoppelten $\nu_T=1$ Phase darstellt. In der Drag-Konfiguration zeigte sich, dass sich die transversalen Komponenten des spezifischen Widerstandes bei großen Werten von d/ℓ_B wie zwei unabhängige Quanten-Hall Systeme bei $\nu=1/2$ verhalten, d.h. $\rho_{drive,xy} \approx 2h/e^2$ und $\rho_{drag,xy} \approx 0$. Nähert man sich allerdings mit d/ℓ_B niedrigeren Werten, so findet ein Phasenübergang von einer schwach-gekoppelten Phase zur stark-korrelierten $\nu_T=1$ Phase statt. Beim Überschreiten der Phasengrenze, gewinnt der $\nu_T=1$ Zustand mit abnehmendem d/ℓ_B rapide an Stärke und die transversalen spez. Widerstände von sowohl $\rho_{drive,xy}$ und $\rho_{drag,xy}$ nehmen einen quantisierten Wert von h/e^2 an. Verändert man allerdings die relativen Elektronendichten in den beiden Lagen so gewinnt für Drag-Messungen die exzitonische Phase an Stärke. Dies Verhalten ist besonders auffällig in den $\rho_{drag,xy}$ Daten, wobei die $\nu_T=1$ Phase durch ein Ungleichgewicht der Dichten sogar erst hervorgerufen werden kann.

Für den Fall der symmetrischen Dichtenungleichheit (Gesamtdichte bleibt konstant), konnte jedoch eine Asymmetrie in den Aktivierungsenergien $\Delta_{\nu=1}$ der einzelnen Schichten beobachtet werden. Es zeigte sich, dass die Aktivierungsenergie in jeder Schicht näherungsweise linear mit der Elektronendichte (in der entsprechenden Schicht) zunimmt. Dies deutet darauf hin, dass die gemessenen Aktivierungsenergien weder die Kondensationsenergie des Exziton-Kondensates noch die Bindungsenergie der Exzitonen wiederspiegeln, da beide Werte unabhängig davon sein sollten, ob man sie aus Messungen an der oberen oder unteren Schicht bestimmt. Stattdessen deutet alles darauf hin, dass die Aktivierungsenergie eine Energielücke für Ladungsanregungen in der *jeweiligen* (Einzel-)Schicht darstellt, welche sich wesentlich für positive und negative Dichtenungleichheit unterscheidet. Wie im $\Delta_{\nu=1}$ gegen d/ℓ_B Fall, sind die Aktivierungsenergien in der Drag- und Counterflow-Konfiguration bei Dichtenungleichheit ungefähr gleich.

Vor nicht allzulanger Zeit wurde spekuliert, ob sich der quantisierte Hall-Drag von h/e^2, welcher im $\nu_T=1$ Zustand beobachtet werden kann, nicht zum Bau eines neuartigen Aufwärt-

stransformators eignen würde [14, 15]. Diese Dissertation umfasst den ersten experimentellen Versuch, solch ein Gerät zu realisieren. Unter Verwendung eines "Spalt-Gates", welches das obere zwei-dimensionale Elektronengas in zwei Regionen trennt, konnte gezeigt werden wie die induzierte Hallspannung im ν_T=1 Zustand in der Sekundärschicht (V_2) auf $V_2 = 2I_1h/e^2$ hochtransformiert wird, wobei I_1 Strom ist, der durch die Primärschicht geschickt wird.

Schlagworte: Doppellagensysteme, Exzitonen-Kondensat, Quanten-Hall-Effekt

Contents

Constants, Abbreviations and Symbols

Constants

$e^2/h = 0.3874045 \times 10^{-6} \ \Omega^{-1}$ conductance quantum

$m* = 0.067m_0$ effective mass in GaAs

$e = -1.6021917 \times 10^{-19} \ \text{C}$ electron charge

$m_0 = 9.109558 \times 10^{-31} \ \text{kg}$ electron mass

$\phi_0 = h/e = 2.41797 \ \text{Tm}^2$ magnetic flux quantum

$\epsilon_0 = 8.85418781762 \times 10^{-12} \ \text{F/m}$ permittivity constant

$\mu_0 = 1.25663706143 \times 10^{-6} \ \text{H/m}$ permeability constant

$h = 6.626196 \times 10^{-34} \ \text{Js}$ Planck constant

$\hbar = \frac{h}{2\pi} = 1.054573 \times 10^{-34} \ \text{Js}$ reduced Planck constant

$c = 2.99792458 \times 10^8 \ \text{m/s}$ speed of light in vacuum

$R_K = 25812.807 \ \Omega$ von Klitzing constant

Abbreviations

2DES	2-Dimensional Electron System
AC	Alternating Current
AlGaAs	Aluminium Gallium Arsenide
BEC	Bose-Einstein Condensate
CF	Composite Fermion
DC	Direct Current
DOS	Density Of States
DQW	Double Quantum Well
FWHM	Full Width at Half Maximum
FQH	Fractional Quantum Hall
FQHE	Fractional Quantum Hall Effect
GaAs	Gallium Arsenide
IQHE	Integer Quantum Hall Effect

LL	Landau Level
LLL	Lowest Landau Level
MBE	Molecular Beam Epitaxy
MC	Mixing Chamber
QH	Quantum Hall
QHE	Quantum Hall Effect
QW	Quantum Well
RHEED	Reflective High Energy Electron Diffraction
SdH	Shubnikov-de Haas
UHV	Ultra High Vacuum

Symbols

$\mathbf{A}$	vector potential
α	fine structure constant
B	magnetic field
B_c	critical magnetic field
B_eff, B^*	effective magnetic field
e-h	electron-hole pair
$B_\perp$, B_perp	perpendicular magnetic field
B_tot	total magnetic field
B_z	magnetic field in z-direction
Δ	activation gap
Δ_CF	CF cyclotron energy
E_subband	subband energy
E_C	Coulomb energy
E_exch	exchange energy
E_F	Fermi energy
E_Z	Zeeman energy
e	electron charge
e^*	fractional electron charge
ϵ_0	dielectric constant in vacuum
Φ_0, ϕ_0	magnetic flux quantum
Φ	magnetic flux
g_CF^*	composite fermion g-factor
g_e	free electron g-factor
g_s	spin degeneracy

H	Hamiltonian
$\mathbf{H}_{\mathrm{N}}$	Hermite polynomials
k_{B}	Boltzmann constant
k	wavevector
k_x, k_x	wavevector components in the plane of the 2DES
$k_{\mathrm{F,CF}}$	wavevector of the CF Fermi surface
ℓ_{B}	magnetic length
m	odd integer number
m^*_{CF}	composite fermion effective mass
m_{e}	free electron mass
m^*	effective electron mass in 2DES GaAs
μ, μ_{e}	mobility
μ_0	permeability constant
μ_{B}	Bohr magneton
N	Landau level index
N_T	total number of electrons
n, n_{e}	electron density
n_{CF}	CF density
n_{L}	degree of degeneracy in each LL
ν, ν_{e}	electron filling factor
ν_{CF}	CF filling factor
ν_{T}	total filling factor
R_{xx}	longitudinal resistance
$R_{\mathrm{xy}}, R_{\mathrm{H}}$	transverse or Hall resistance
$\hat{\rho}$	resistivity tensor
ρ_{s}	spin stiffness
ρ_{xx}	longitudinal resistivity
$\rho_{\mathrm{xy}}, \rho_{\mathrm{H}}$	transverse or Hall resistivity
$\hat{\sigma}$	conductivity tensor
σ_{xx}	longitudinal conductivity
$\sigma_{\mathrm{xy}}, \sigma_{\mathrm{H}}$	transverse or Hall conductivity
T	temperature
τ	scattering time
V_{xx}	longitudinal voltage
$V_{\mathrm{xy}}, V_{\mathrm{H}}$	Hall voltage
$\mathbf{v}_{\mathrm{D}}$	drift velocity
ω_{c}	cyclotron frequency

$\omega_c^*, \omega_{c,\mathrm{CF}}$	CF cyclotron frequency
z_i	position of electron i (complex number)

Chapter 1

Introduction

The quantum Hall effect (QHE) discovered in 1980 by Klaus von Klitzing [16] has reached its quarter century mark. Over these past years the quantum Hall field has continued to be a source of novel and new physical information that is challenging to researchers both on the experimental and theoretical fronts. Even with the rapid expansion of experimental and theoretical tools available to today's physicist the 25 year old integer quantum Hall effect (IQHE) still remains a mysterious phenomena that lacks a full theoretical description. This is a demonstration of the deep fundamental principles underlying quantum Hall physics, where connections to formally non-related high energy phenomena as black holes [17], quarks [18], and string theory [19] have been made. In addition to being a novel source for new physics, the quantum Hall effect has also contributed to the development of certain applications. For example, the observed quantization of the Hall resistance to a value of h/e^2, irrespective of microscopic details of the semiconductor system, has lead to its adoption in defining the SI unit Ohm. In 1990 the fixed value of R_{K-90}= 25812.807 Ω was accepted as the conventional value forming laboratory reference standards, where R_K=h/e^2 is known as the von Klitzing constant.

Technological improvements in the field of molecular beam epitaxy (MBE) have lead to the creation of two-dimensional electron systems (2DES) in GaAs quantum wells (QW) where electrons can travel over 200 μm before suffering from a scattering event. This is a three order magnitude improvement over the initial ~ 2 μm ballistic length for electrons in Si/SiO$_2$ systems used by von Klitzing 25 years earlier to measure the IQHE. In addition to these technological improvements in semiconductor growth, advances in refrigeration, high magnetic fields, and electronics equipment now allow for low noise measurements at milli-Kelvin (mK) temperatures and high magnetic fields (> 20 T) to be routinely made. It is precisely these technological advances that ushered in the discovery of the fractional quantum Hall effect (FQHE) in 1982 by Strömer and Tsui [20, 21, 22] where an AlGaAs/GaAs heterostructures was used. The non-interacting single electron picture used to explain the IQHE could no longer account for these new quantum Hall (QH) states and it was soon realized that the FQHE was a direct manifesta-

tion of electron-electron correlations mediated by the Coulomb interaction. Unfortunately, the massive number of electrons typically found in an experimental 2DES (10^9-10^{11} cm^{-2}) prevents an exact solution using conventional theoretical methods to be made. This was overcome by Laughlin, who in 1983 proposed a many-body ground state trial wavefunction that was able to account for the most pronounced ν=$1/q$ FQHE states [23, 24]. This brought into play many exotic physical concepts as fractionally charged quasiparticles, anyonic statistics, and composite fermions needed to properly to account for these FQHE states.

In addition to a single 2D charge carrier layer, technology allows for the creation of two closely spaced electron or hole layers with separate electrical contacts to each of the layers [8,9]. Typically formed using two closely spaced QWs, the average interlayer separation between the two charge carrier layers is parameterized by the center-to-center quantum well distance d. Subjecting such a bilayer system to a perpendicular magnetic field with respect to the layers brings about Landau quantization which effectively freezes out the kinetic energy degree of freedom of the electrons. This leads to a system where many electrons exist simultaneously at the same energy level as defined by the Landau level degeneracy $eB_\perp/h$. In the case of a sufficiently high $B_\perp$, all the electrons can be placed in the lowest spin split Landau level (LLL), and thus can all reside at the same energy, resulting in intralayer electron-electron interactions becoming very strong. The mean intralayer electron wavefunction spacing within such a layer is parameterized by the magnetic length $\ell_B = \sqrt{\frac{\hbar}{eB}}$. In the case when the intralayer Coulomb correlation energy $E_C = \frac{e^2}{4\pi\epsilon\ell_B}$ is much larger than the interlayer Coulomb correlation $E_d = \frac{e^2}{4\pi\epsilon d}$ the system will behave as two independent single layers having infinite separation between them. However, as E_C approaches E_d the two layers will interact with each other, producing a new novel state not seen in single layer systems. The relative importance of these energies can be related to each other by the ratio d/ℓ_B. At large d/ℓ_B one has the case where each electron has a unitary probability of only existing in the upper or lower layer, whereas at lower d/ℓ_B ratios a coupled layer state can form under appropriate experimental conditions. In bilayer samples having virtually zero interlayer tunneling, the tuning of the system to a total filling factor of ν_T=1 will bring about a new excitonic superfluidic state when d/ℓ_B is below a certain critical ratio. In this state a positional uncertainly now exists as to which layer each electron is located. This has lead to some remarkable discoveries as a zero interlayer bias Josephson like tunneling peak [3], quantized Hall resistance in the drag layer [4], and possible excitonic formation [5, 6, 7].

There are three different ways to view this ν_T=1 state: these include the Halperin (111) picture, the pseudospin picture, and the exciton picture. Although mathematically equivalent to each other, certain viewpoints nevertheless allow a more intuitive picture in understanding certain ν_T=1 experimental phenomena. The Halperin (111) picture is a reformulation of Laughlin's wavefunction by Halperin more than 20 years ago to account for systems with two different

electron spin Landau states existing at the same energy [25]. Here a replacement of the two spin levels by the two 2DES layers is found to offer a description of the ν_T=1 state. The pseudospin picture rewrites the ν_T=1 state in spin-1/2 language using pseudospin up ($|\uparrow\rangle$) and down ($|\downarrow\rangle$) to denote an electron in the upper or lower layer, respectively [26]. Finally the most exciting picture considers the ν_T=1 state as a Bose-Einstein condensate of electron-hole pairs [27,28,29]. At ν_T=1, with equal layer electron densities, one has the situation where each of the individual layer LLs is at ν=1/2 or half filled with electrons. By performing a particle-hole transformation, it is equivalent to interpret one of these single layer LLs as being half filled with empty states or holes. Due to Coulomb interactions the most energetically favorable state is one where each electron is maximally spaced from both the electrons within the layer and electrons in the other layer. This leads to the case where each electron is located directly opposite to an empty state or hole in the other layer. At ν_T=1 there will exist an equal number of electrons and holes, allowing electrons in one layer to bind with holes in the other layer forming electron-hole pairs (e-h) or excitons. Since e-h pairs are charge opposite particles the overall net charge will be neutral. Also since the electron and hole momentum vectors are equal but opposite in direction all excitons will have the same net $k = 0$ state. This fortunately does not violate the Pauli exclusion principle since both the electron and hole are both spin-1/2 fermionic particles that add to form an even spin composite boson particle. It was therefore predicted under appropriate conditions of dilute exciton densities and low temperatures a bilayer system can undergo Bose-Einstein condensation.

The feasibility of a BEC of excitons in semiconductor systems was raised over 40 years ago by theoreticians [1, 2]. It was predicted that excitons due to their light mass should undergo condensation at temperatures of ~ 1 K, which is approximately 10^6 greater than the typical condensation temperature of more heavily alkali atom BECs ($T_c = 10^{-6}$ K). Since the ground state of a pure semiconductor has no electrons or holes present, e-h pairs have been traditionally created by thermally or optically exciting electrons from the valence band into the conduction band leading to the creation of free electrons and free holes that can bind to form excitons. Unfortunately, these excitons exist in a highly non-equilibrium state where the electrons and holes will quickly recombine in relatively short times of ns or μs. The time needed for excitons to cool from their optical excited values to below the critical condensate temperature T_c is typically much longer than the recombination time, preventing condensation from occurring. In addition, other complications possibly hampering condensation arise due to the electrons and holes residing in separate bands, where the different band dispersion relations may lead to Fermi nesting [30]. Problems with short exciton lifetimes and different band dispersions in optically generated exciton systems are avoided in quantum Hall bilayer systems. At ν_T=1 e-h pairs can exist at equilibrium in the groundstate and thus have infinite lifetimes, foregoing any optical excitation requirements. In addition the e-h pair is now formed between two dispersionless

Landau bands located in the QW conduction bands, meaning that for different k-vectors the energy is completely degenerate avoiding any problems with Fermi nesting.

The focus of this work is the investigation of this new ν_T=1 excitonic superfluidic state in 2D bilayer electron systems. More specifically this includes the reproduction of previous experimental claims and the further characterization of this relatively unknown bilayer quantum Hall state.

- **CHAPTER 2: Two-Dimensional Electron Systems** - The basic physics and main experimental properties associated with single layer 2D electron systems are presented in this chapter. This includes an overview of some of the various semiconductor systems used to confine electrons in the xy-plane and the technology needed to create them. The core physics describing 2DESs at zero magnetic fields is presented before moving on to the case where a perpendicular magnetic field ($B_\perp$) is applied with respect to the xy-plane. For the weak $B_\perp$ case a description of the magneto-transport properties of a 2DES is given using a classical formulation. For the strong $B_\perp$ case a full quantum mechanical treatment is used to explain the formation of Landau levels (LLs). Finally, it is shown how LLs lead to the integer quantum Hall effect (IQHE) and, for higher sample quality, to the fractional quantum Hall effect (FQHE).

- **CHAPTER 3: Two-Dimensional Electron Bilayer Systems** - A bilayer system is formed when two charge carrier layers are brought in close proximity to each other. This chapter initially discusses the basic concepts needed to describe 2D electron bilayer systems. The case of bilayer systems with high interlayer tunneling is initially discussed before focusing on the more complex low interlayer tunneling systems. The three different viewpoints used to view the ν_T=1 state in low tunneling bilayer systems is presented. These include the Halperin (111) picture, the pseudospin picture, and the exciton picture.

- **CHAPTER 4: Samples and Processing** - The fabrication of high quality electron bilayer samples is a technology challenging task. Only quite recently progress in molecular beam epitaxy (MBE) has allowed for the possibility of growing epitaxial crystal structures showing the ν_T=1 excitonic effect with a highly resistive interlayer barrier [3]. In addition to crystal growth, other technical challenges include: development of annealing techniques to electronically contact the 2DESs, making separate electrical contacts to the individual layers, and fabricating electrostatic gates to control the layer electron densities. The first portion of this chapter presents details on the crystal structure used to confine electrons in two closely spaced 2DES. Next the method used to electrically contact the individual electron layers is discussed. Finally, different sample designs used in this work will be shown.

- **CHAPTER 5: Experimental Setup** - In addition to high quality bilayer samples, an investigation of the ν_T=1 excitonic state requires the use of highly specialized experimental equipment. The first half of this chapter discusses how the experimental conditions of low sample temperatures (T < 200 mK) and large perpendicular magnetic fields ($\sim$ 2 T) necessary to observe the ν_T=1 state are achieved. The second half discusses the techniques used to make low noise magneto-transport and tunneling measurements.

- **CHAPTER 6: The ν_T=1 State at Balanced Electron Layer Densities** - This chapter investigates the properties of the ν_T=1 state for balanced layers densities. Initially, the interlayer tunneling is investigated where a large zero interlayer voltage tunneling peak appears collaborating similar results as reported by Spielman et al. [3]. Also experimental magneto-transport data is presented using the drag and counter-flow current configurations. For the drag configuration the amazing quantization of both the "drive" and "drag" Hall resistivities to h/e^2 in the vicinity of ν_T=1 state is shown. Also in the counter-flow current configuration it is found that both longitudinal ρ_{xx} and transverse ρ_{xy} resistivities tend towards zero! This has been claimed to be a direct signature of the ν_T=1 state supporting the flow of neutral particle excitons. From measurements of the temperature dependence of the magneto-transport data of the ν_T=1 state, activation energies $\Delta_{\nu=1}$ vs. d/ℓ_B are presented for the first time.

- **CHAPTER 7: The ν_T=1 State at Imbalanced Electron Layer Densities** - In addition to the balanced electron layer density case the layers can also be symmetrically imbalanced through application of either an interlayer voltage bias or by using the upper and lower field gates. This chapter explores the role of imbalanced electron densities in the two layers making up the ν_T=1 state. The concept of imbalanced layers electron densities where the total system density is fixed to a constant value will be introduced. The phase boundary existing between the weakly coupled individual layer (ν_U=1/2, ν_L=1/2) case and the strongly coupled ν_T=1 state as obtained from magneto-transport data is shown as a function of imbalance Δn vs. d/ℓ_B. Finally, temperature dependent activation measurements of the ν_T=1 state as a function of imbalance are shown to have some unusual and unexpected effects not consistent with exciton condensate picture.

- **CHAPTER 8: Excitonic Superfluid DC Transformer** - With the drag configuration it is experimentally shown that in the vicinity of ν_T=1 state the essentially zero Hall drag $\rho_{drag,xy}$ component suddenly increases to a quantized value of h/e^2 with no current flowing in this layer! Girvin [14] has proposed using this strange effect to construct a DC transformer and it's first experimental attempt is presented in this chapter. Some of the basic theoretical aspects of a transformer built using the ν_T=1 state is initially discussed before the presentation is given of some new exciting experimental data obtained from a

constructed DC transformer.

Chapter 2

Two-Dimensional Electron Systems

In Sec. 2.1 the fundamental concepts needed to define a 2D electron system (2DES) are presented. The physics of applying a weak perpendicular magnetic field ($B_\perp$) to a 2DES is explored in Sec. 2.2.1 and later, in Sec. 2.2.2, the application of higher magnetic fields leading to the formation of Landau levels (LLs) is discussed. The formation of LLs leads to the integer quantum Hall effect (IQHE), and in the case of higher quality samples, to the fractional quantum Hall effect (FQHE). These two quantum Hall effects are presented in sections Sec. 2.2.3 and Sec. 2.2.4, respectively.

2.1 Basic Concepts of a 2DES

A 2DES is created whenever there is a confinement potential that restricts electron motion only to a plane [31]. Such a system has been experimentally realized in a wide variety of different ways. For instance, electrons deposited on the surface of ^{4}He will form a dilute 2DES, or planes of naturally occurring graphite will show a quasi-2D behavior along the plane direction, or even certain polymer sheets will display 2DES characteristics. Semiconductor systems also allow for the creation of 2DESs, and have the distinct advantage that the exact position of the 2DES can be tailor designed using common semiconductor growth and lithography techniques. Several of the more common semiconductor 2DES are displayed in Fig. 2.1. In a Si-MOSFET a bias voltage is applied to pull down the conduction band below the Fermi energy at the Si/SiO_2 interface creating a triangular QW leading to a 2DES. The Si/SiO_2 interface, however, is rough and leads to a low 2DES quality. A more ideal interface displaying high electron mobilities is found using III-V technology. As schematically shown in Fig. 2.1 a AlGaAs/GaAs heterojunction can be grown with an atomically precise interface. Here the dopant atoms are displaced away from the triangular QW as to avoid ionized impurity scattering. A similar heterojunction system, but with a square potential well, can be realized using a AlGaAs/GaAs/AlGaAs epilayer sequence. In this case electrons provided by donor atoms located on both sides of the QW become trapped

with in the QW at low temperatures. It is such wide square QW systems that currently hold the 2DES mobility record of 31×10^6 cm^2/Vs at 2×10^{11} cm^{-2} [32]. The refinement of semiconductor growth techniques over the years now allows for the possibility of growing tailored designed epitaxial crystal structures, which can incorporate a 2DES with atomic layer precision. Two of the more common crystal growth techniques include Molecular Beam Epitaxy (MBE) [33, 34] and Organic-Metallic Vapour Phase Epitaxy (OMVPE) [35]. In the case where low impurity densities and high electron mobilities are required MBE is the preferable technique due to its intrinsic ultra high vacuum (UHV) environment and ultra pure material sources.

The fundamental characteristics of a 2DES can be expressed as electrons being confined to a film of width w by infinitely high barriers at $z = 0$ and $z = w$ as shown for the 2D case in Fig. 2.2. Taking into consideration that the electron wavefunction is subjected to the boundary conditions at $z = 0$ and $z = w$ where $\Psi \to 0$, one obtains a wavefunction where the xy-plane electron motion is a free traveling wave and the z-motion is a standing wave as shown by the following wavefunction

$$\Psi(x, y, z) = e^{ik_x x} e^{ik_x y} sin(k_z z), \tag{2.1}$$

where k_x, k_y, and k_z are the momentum coordinates in the x, y, and z directions, respectively. Inserting this wave function into the Schrödinger equation and solving for the energy eigenvalues one obtains

$$\varepsilon = \frac{\hbar^2 (k_x^2 + k_y^2)}{2m^*} + \frac{\hbar^2 \pi^2 n^2}{2m^* w^2}. \tag{2.2}$$

Here m^* is the electron effective mass and $n = 1, 2, 3...$ are the subband quantum numbers along the z-direction. The first term in Eq. 2.2 corresponds to the free electron kinetic energy in the xy-plane and the last term defines the energy levels along the z direction, where it should be noted that the z direction eigen-energies are the same as those found in the Schrödinger solution for a 1D square potential well.

The $n = 2$ energy level is $\frac{3\hbar^2 \pi^2}{2m^* w^2}$ higher in energy than the $n = 1$ ground state level, therefore for a 10 nm GaAs QW with an electron effective mass of $0.067 m_e$, the energy required to excite an electron from the ground state to the next level is 168 meV, corresponding to a temperature of $T = E/k = 1953$ K! Hence, it can be assumed that all electrons are effectively frozen in the ground state at low temperatures. Even at room temperature most electrons will be confined to the ground state. The large confinement potential effectively quenches motion in the z-direction creating an almost ideal 2DES.

The density of states (DOS) is unique in the 2D case due to its independence from energy as shown in Fig. 2.2. The general DOS expression for d-dimensional systems with energy eigenvalues $\varepsilon = \hbar^2 k^2 / 2m$ and periodicity volume L^d is given by

$$\frac{dN}{dE}_d = D_d(E) = \frac{g_s \Lambda_d}{(2\pi)^2} \frac{2m}{\hbar^2} \left(\frac{2m}{\hbar^2} E \right)^{(d-2)/2}, \tag{2.3}$$
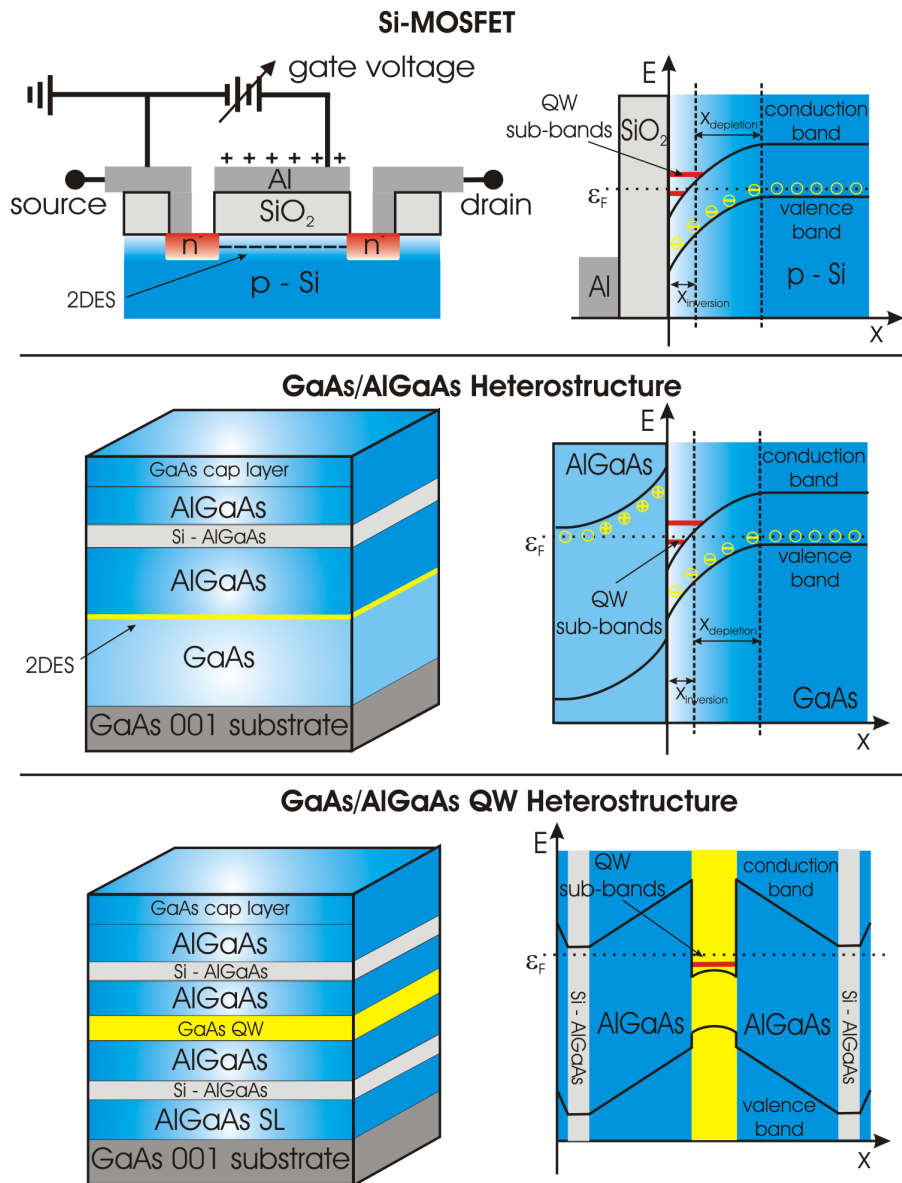
Figure 2.1: Three typical semiconductor systems used to confine electrons in the xy-direction by quantizing the motion along the z-axis as shown by the corresponding energy band configurations. Top: in a Si-MOSFET the 2DES is formed at the Si/SiO$_2$ interface by apply a positive bias to an Al top field gate. Middle: a GaAs/AlGaAs heterostructure showing the location of the triangular QW subband just below the GaAs/AlGaAs interface. Bottom: A square GaAs QW with spatially separated Si dopant regions on both sides.

where Λ_d is the surface area of the d-dimensional unit sphere. For the case of $g_s = 2$ and an
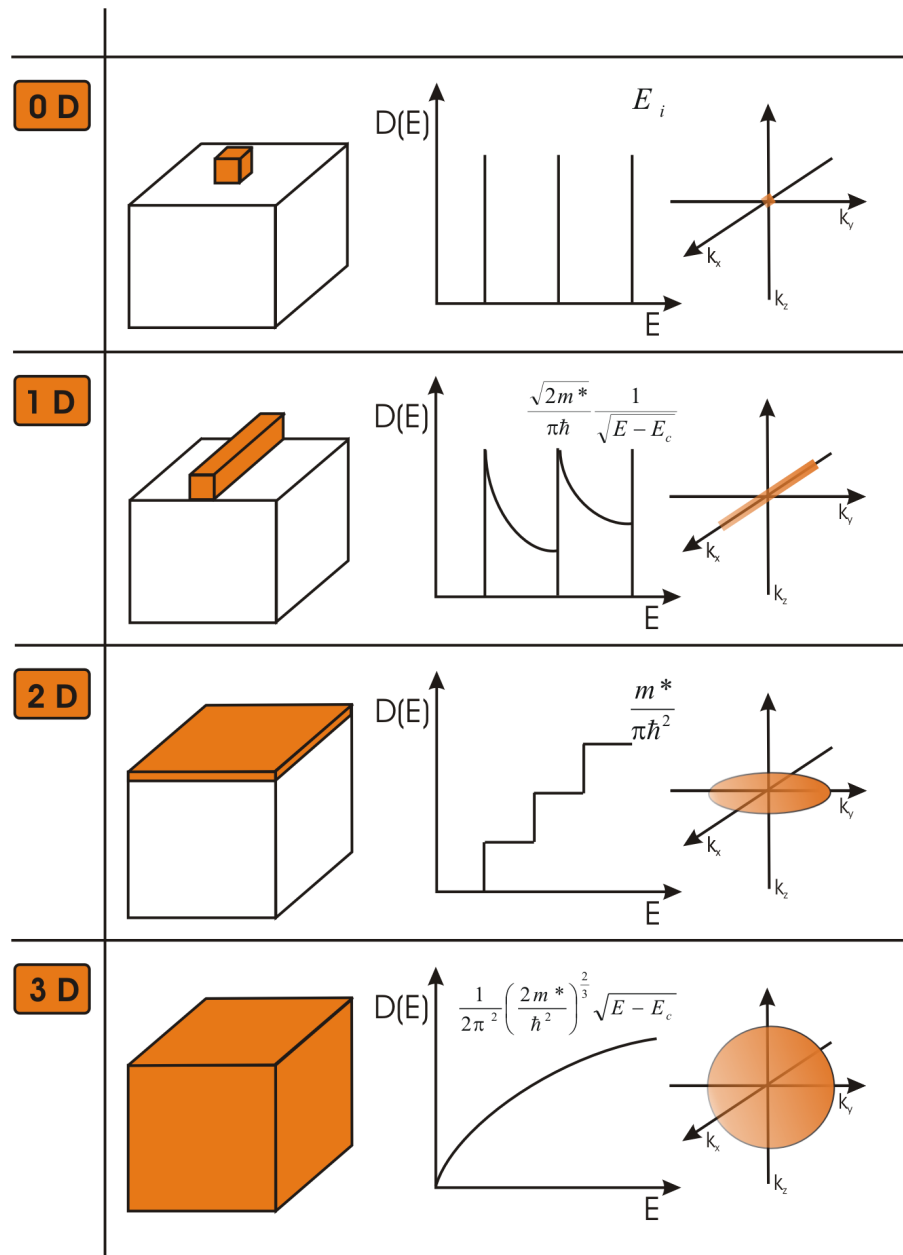
Figure 2.2: The DOS and corresponding Fermi surfaces for different dimensional systems. A 0D quantum dot/atomic system has electron confinement in all directions. A 1D wire system restricts motion to one direction and has an energy dependent DOS. In 2D motion is restricted to a plane and the DOS is uniquely energy independent. For 3D all spatial motion is allowed.

effective mass $m_{GaAs} = 0.067 m_e$ the 2D DOS is calculated to be,

$$D_2(E) = \frac{m^*}{\pi\hbar^2} = 1.75 \times 10^{32} cm^{-2}/J = 2.79 \times 10^{10}(meV\,cm^2)^{-1} \tag{2.4}$$

leading to a ground state that can easily accommodate most experimentally generated electron concentrations without fear of populating the next higher energy subband. Due to the energy independent DOS the Fermi energy E_F is directly proportional to the electron density n_s as given by

$$E_F = \frac{2\pi\hbar^2}{g_s m^*} n_s, \tag{2.5}$$

leading to the following Fermi vector

$$k_F = \sqrt{\frac{4\pi n_s}{g_s}} = \sqrt{\frac{4\pi n_s}{g_s}}. \tag{2.6}$$

Here all electrons reside in the lowest electronic subband, having a continuous kinetic energy spectrum within the xy-plane. This creates a 2DES even though the QW has a non ideal finite width.

2.2 2DES + Magnetic Field

2.2.1 Low B-Field Magneto-Transport
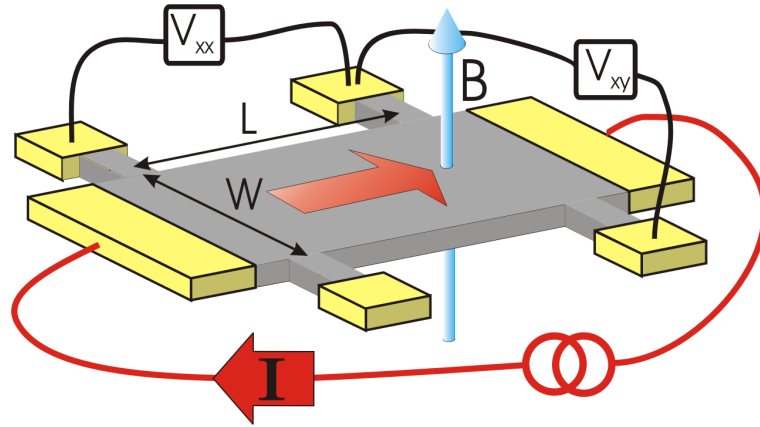
Figure 2.3: Sketch of a conventional Hall bar configuration. A current I is sent from source to drain through the Hall bar 2DES which is located in a perpendicular magnetic field B. The longitudinal resistivity ρ_{xx} is determined by a measurement of the longitudinal voltage V_{xx} where $\rho_{xx} = \frac{V_{xx}}{I_{xx}} \frac{W}{L}$. The Hall resistivity is ρ_H is related to $\rho_{xy} = \frac{V_{xy}}{I_{xx}}$.

At low magnetic fields a classical formulation can be used to treat the observed magneto-transport properties of a 2DES. In reference to Fig. 2.3 the experimentally measured transport observables are the longitudinal R_{xx} and transverse R_{xy} resistances. Due to the system having

local electric field vectors which are not parallel to the current flow I it becomes necessary to define a conductivity tensor that connects the local E field to the current density $\mathbf{j}$,

$$\mathbf{j} = \hat{\sigma}\mathbf{E}, \quad \text{where} \quad \hat{\sigma} = \begin{pmatrix} \sigma_{\text{xx}} & \sigma_{\text{xy}} \\ \sigma_{\text{yx}} & \sigma_{\text{yy}} \end{pmatrix}. \tag{2.7}$$

The resistivity tensor can be obtained by taking the inverse of the conductivity tensor

$$\hat{\rho} = \hat{\sigma}^{-1} = \begin{pmatrix} \rho_{\text{xx}} & \rho_{\text{xy}} \\ \rho_{\text{yx}} & \rho_{\text{yy}} \end{pmatrix}, \tag{2.8}$$

where the experimentally determined resistances can be related to the tensor resistivity components as follows

$$R_{xx} = \frac{V_{xx}}{I_{xx}} = \rho_{xx}\frac{L}{W} \quad \text{and} \quad R_{xy} = \frac{V_{xy}}{I_{xx}} = \rho_{xy}, \tag{2.9}$$

with L being the sample length and W the sample width. Assuming an isotropic system (Onsager relation), where $\rho_{xx} = \rho_{yy}$ and $\rho_{xy} = -\rho_{yx}$, the conductivity tensor can be expressed in terms of the resistivities as

$$\hat{\sigma} = \hat{\rho}^{-1} = \frac{1}{\rho_{\text{xx}}^2 + \rho_{\text{xy}}^2} \begin{pmatrix} \rho_{\text{xx}} & -\rho_{\text{xy}} \\ \rho_{\text{xy}} & \rho_{\text{xx}} \end{pmatrix}. \tag{2.10}$$

It should be noted that if $\rho_{xx} \to 0$ then $\sigma_{xx} \to 0$ whenever $\rho_{xy} \neq 0$, which is opposite from a superconductor since both $\rho_{xx} \to 0$ and $\rho_{xy} \to 0$ and hence $\sigma_{xx} \to \infty$.

In the absence of collisions within a crystal electrons obey the following acceleration equation

$$\frac{d\mathbf{v}}{dt} = -e[\mathbf{E} - \mathbf{v}_d \times \mathbf{B}], \tag{2.11}$$

where $\mathbf{v}_d$ is the drift velocity, $\mathbf{E}$ is the electric field and $\mathbf{B}$ the magnetic field. In the absence of an applied magnetic field Eq. 2.11 predicts that a DC electric field will lead to a constant acceleration of the electrons and therefore lead to a steady increase of the electron current! In practice this is not the case since an electron will only be accelerated for a finite time, τ before colliding with phonons, impurity atoms, vacancies and other structural defects. At finite temperatures the scattering time is given to good approximation by

$$\frac{1}{\tau} = \frac{1}{\tau_{ph}(T)} + \frac{1}{\tau_0}, \tag{2.12}$$

where $\tau_{ph}(T)$ is the temperature dependent electron-phonon scattering time that tends to infinity as $T \to 0$, and τ_0 is the imperfection scattering time based on Matthiessen's rule which states that these crystal imperfections are temperature independent. Taking in account Eq. 2.12 the Drude model [36] gives the steady state condition where the electric field force is balanced with this "frictional" scattering force,

$$\left[\frac{d\mathbf{p}}{dt}\right]_{scattering} = \left[\frac{d\mathbf{p}}{dt}\right]_{field} \quad \rightarrow \quad \frac{m^*\mathbf{v}_d}{\tau} = -e[\mathbf{E} - \mathbf{v}_d \times \mathbf{B}], \tag{2.13}$$

here m^* is the electron effective mass. Together with the definition of the current density $\mathbf{j} = en_s\mathbf{v}_d$ and Ohm's law $\mathbf{E} = \rho\mathbf{j}$, this yields

$$\rho_{xx} = \frac{m^*}{n_s e^2 \tau} = \frac{1}{n_s e \mu} \quad \text{and} \quad \rho_{xy} = \frac{B}{en}, \tag{2.14}$$

where n_s is the electron density. The constant of proportionality between the drift velocity and the electric field is known as the mobility,

$$\mu = \frac{|\mathbf{v}_d|}{|\mathbf{E}|} = \frac{e\tau}{m^*}. \tag{2.15}$$

Since the mobility is directly proportional to the scattering time it is a general measure of the overall sample quality. The distance an electron located on the Fermi surface can travel between successive scattering events is given by the transport electron mean free path

$$l = v_F \tau \quad \text{and} \quad v_F = \sqrt{\frac{2E_F}{m^*}}, \tag{2.16}$$

where v_F is the Fermi velocity calculated from the Fermi energy E_F.

2.2.2 High B-Field Magneto-Transport

When an electron can complete a full cyclotron orbit without scattering it can quantum mechanically interfere with itself and the classical Drude picture presented in Sec. 2.2.1 is no longer valid. A quantum mechanical treatment is thus necessary [37].

The Lagrangian for a charged particle in an electric and magnetic field can be written as

$$L(q, \dot{q}, t) = T(q, \dot{q}, t) - V(q, t) = \frac{1}{2}m^*\dot{\mathbf{q}}^2 - e\dot{\mathbf{q}} \cdot \mathbf{A} - eV, \tag{2.17}$$

where $\dot{\mathbf{q}}$ is the time derivative of the generalized spatial coordinate $\mathbf{q}$ and $\mathbf{A}$ is the magnetic vector potential $\mathbf{B} = \nabla \times \mathbf{A}$. It can be readily seen that the canonical momentum

$$p_i = \frac{\partial L(q, \dot{q}, t)}{\partial \dot{q}} = m\dot{q}_i + eA_i, \tag{2.18}$$

is no longer a strictly mass velocity relation $m\dot{q}$ for a free particle, but is also dependent on the magnetic field. In a fully quantum mechanical treatment that neglects scattering processes, electron spin, and electron-electron interactions, an electron located in a 2DES with a perpendicular external magnetic field $\mathbf{B} = \nabla \times \mathbf{A}$ can be described by the time independent Schrödinger equation. Performing a Legendre transformation on Eq. 2.17 to obtain the Hamiltonian and replacing the canonical momentum by $\mathbf{p} = -i\hbar\nabla$ the Schrödinger equation is

$$H\psi(x, y) = \frac{1}{2m^*}\left[\mathbf{p} + e\mathbf{A}\right]^2 \psi_n(x, y) = E_n\psi_n(x, y). \tag{2.19}$$

In this case it can be seen that the Hamiltonian operator is just the kinetic energy obtained from the canonical momentum (see Eq. 2.18). It is convenient to use the Landau gauge $\mathbf{A} = (-Bx, 0, 0)$, where the magnetic field is $\mathbf{B} = \nabla \times \mathbf{A} = B\hat{z}$. In this case the vector potential points in the y-direction but only varies with the x position. Hence the system has translational invariance in the y-direction leading to the following Schrödinger equation

$$\frac{1}{2m^*}\left(p_y^2 + (p_x + eBx)^2\right)\psi_n(x,y) = E_n\psi_n(x,y). \tag{2.20}$$

Taking advantage of the translational symmetry in the y direction, the wavefunction $\psi_n(x,y)$ can be written as a product of free plane waves extending in the y direction and eigenfunctions of a quantum harmonic oscillator in the x direction,

$$\psi_n(x,y) = e^{ik_y y}H_n(x-x_0)e^{-\frac{1}{2\ell_B{}^2}(x-x_0)^2}. \tag{2.21}$$

$H_n(x-x_0)$ is the nth Hermite polynomial displaced to the new central position x_0 and $\ell_B = \sqrt{\frac{\hbar}{eB}}$ is the magnetic length. From this solution the wave function is extended in the y direction as seen by the plane wave solution $e^{ik_y y}$ in Eq. 2.21 but localized in x, centered around the coordinate $x_0 = -k_y\ell_B{}^2 = -\hbar k_y/eB$. The cyclotron radius, which indicates the spread of the wavefunction in the x direction, is given by the magnetic length,

$$R_n = \ell_B\sqrt{2n+1}. \tag{2.22}$$

The energy eigenvalues take the form

$$E_n = \left(n + \frac{1}{2}\right)\hbar\omega_c \tag{2.23}$$

where $\omega_c = \frac{eB}{m^*}$ is the cyclotron frequency. Surprisingly the energy eigenvalues are only dependent on the quantum number $n = 0, 1, 2, ...$ and no longer on the y momentum $\hbar k$, therefore the degeneracy of each quantum number is huge! These harmonic oscillator levels are known as Landau levels (LLs). For the lowest energy the wavefunction is a Gaussian centered about, $x_0 = \frac{-\hbar k_y}{eB}$, therefore a system with dimensions $L_x \times L_y$, periodic boundary conditions on the plane wave in the y-direction require that $k_y = (2\pi/L_y)j$, where $j = 0, \pm1, \pm2, \pm3...$ The spacing between adjacent k-states in the x-direction will be $x_j - x_{j-1} = h/(eBL_y)$. The total number of states of each Landau level or that can fit along $0 < x < L_x$ will then be

$$N_L = \frac{L_x}{x_j - x_{j-1}} = \frac{L_x L_y eB}{h} = \frac{\Phi}{\Phi_0}, \tag{2.24}$$

demonstrating that the number of states per LL increases linearly as a function of magnetic field. The last term of Eq. 2.24 is the total magnetic flux $\Phi = BA$ over a single flux quantum $\Phi_0 = h/e$, stating that there is one state per Landau level per flux quantum. It is also equivalent,

and for certain problems more convenient, to use the symmetric gauge over the Landau gauge. In this case the wave function is circular with a radius given by Eq. 2.22. In the symmetric gauge the LL degeneracy is again equal to the Landau gauge degeneracy

$$N_L = \frac{L_x L_y}{2\pi \ell_B{}^2} = \frac{AeB}{h} = \frac{\Phi}{\Phi_0}. \tag{2.25}$$

As shown in Fig. 2.4 a magnetic field leads to the destruction of the continous DOS as given by Eq. 2.3 leading to the formation of LLs where each LL is separated by the cyclotron gap energy $\hbar\omega_c$ and has a degeneracy as given by Eq. 2.24 and Eq. 2.25. Electrons fill up a discrete set of LL's based on the condition that a given LL can only host N_L states. This allows for the definition of the "filling factor" or the ratio of the total amount of electrons N_s over the number of states N_L in each LL

$$\nu \equiv \frac{N_s}{N_L} = \frac{n_s h}{eB} = \frac{n_s \Phi_0}{B}, \tag{2.26}$$

where n_s is the electron density. When the filling factor ν is at an integer value it corresponds to an exact number of Landau levels being completely filled with the Fermi energy lying in the middle of the cyclotron energy gap as shown in Fig. 2.4. In this case the system is in an incompressible phase due to the large energy required to excite an electron over the gap, giving the system semi-conductor or insulator properties. Adding electrons or decreasing the the number of flux quanta will cause the Fermi level to jump, becoming pinned at the next unfilled LL leading to a compressible state that will show quasi-metallic properties.

All known particles have an additional intrinsic quantum number known as spin that has no classic counterpart. Electrons subjected to a magnetic field will acquire an additional energetic shift known as the Zeeman energy as calculated using the magnetization operator $\hat{M}_S = g^* \frac{e}{2m^*} B \hat{S}_z$,

$$\langle \Psi_S | \hat{M}_S | \Psi_S \rangle = \langle \Psi_S | g^* \frac{e}{2m^*} B \hat{S}_z (|\chi_\uparrow\rangle + |\chi_\downarrow\rangle) = \pm \frac{1}{2} g^* \mu_B B, \tag{2.27}$$

where $\mu_B = \frac{e\hbar}{2m^*}$ is the Bohr magnetron and the electron g^*-factor differs from the vacuum value $g = 2$ due to spin-orbit coupling and other effects from the interactions of electrons within the crystal lattice. Including the Zeeman shift in Eq. 2.23 leads to the following eigen-energies, shown in Fig. 2.4,

$$E_n = (n + \frac{1}{2})\hbar\omega_c \pm \frac{1}{2} g^* \mu_B B. \tag{2.28}$$

Each Landau level therefore splits into two levels corresponding to the higher energy spin up electrons and the lower energy spin down electrons. There now exist two quantum numbers defining a specific Landau level, the cyclotron index n and the electron spin m_s. For example, the lowest Landau level (LLL) $n = 0$ refers to both the spin split energy levels $n = (0, \uparrow)$ and $n = (0, \downarrow)$.
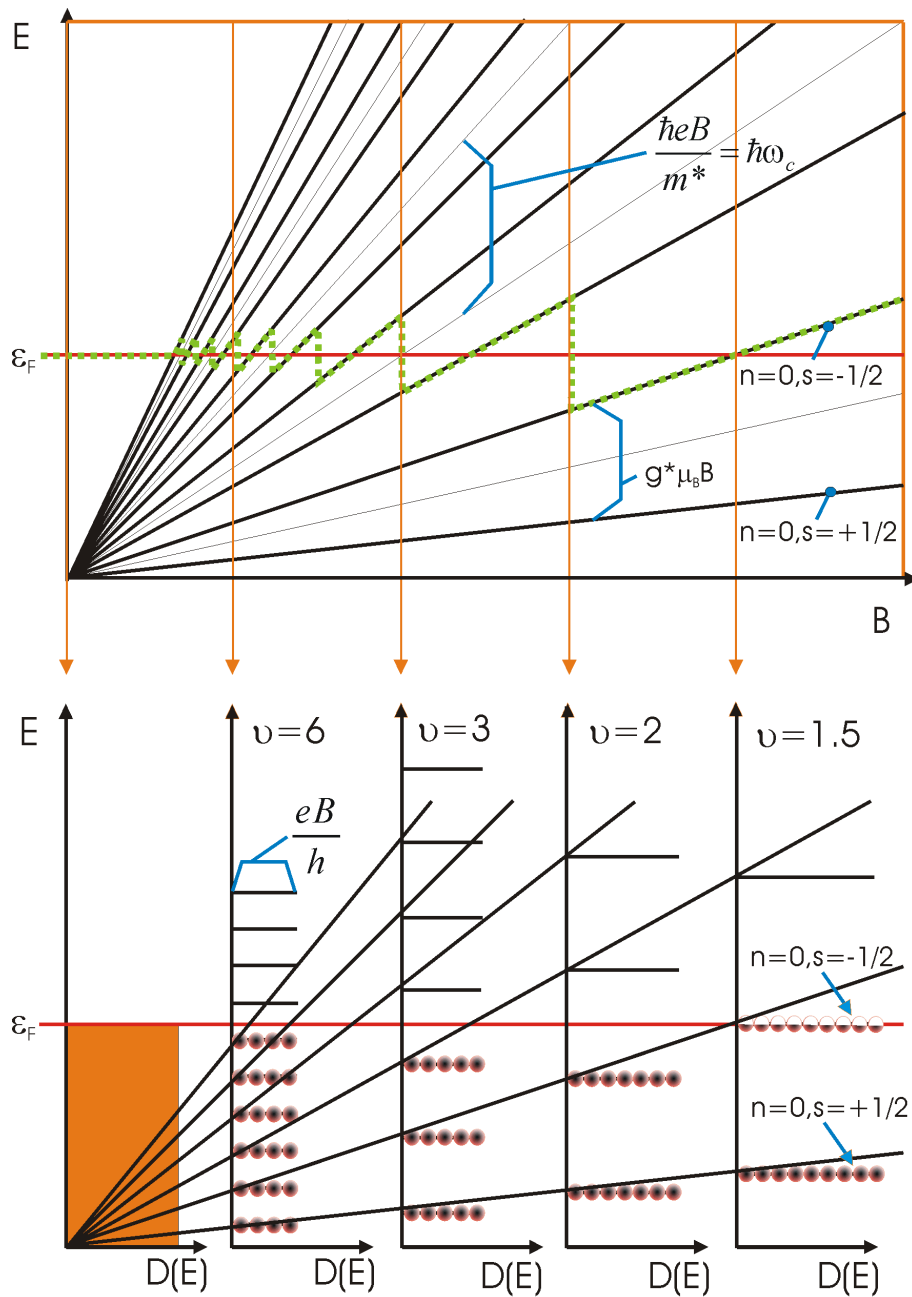
Figure 2.4: Landau level fan diagram including spin degeneracy (top figure) based on Eq. 2.28. The chemical potential oscillates in a saw tooth pattern with increasing magnetic field. The corresponding ideal Dirac-δ like LL energies vs. the states available for different specified magnetic fields are shown in the bottom figure. The individual LL states, pictorially represented by circles, increase with B as according to Eq. 2.24.
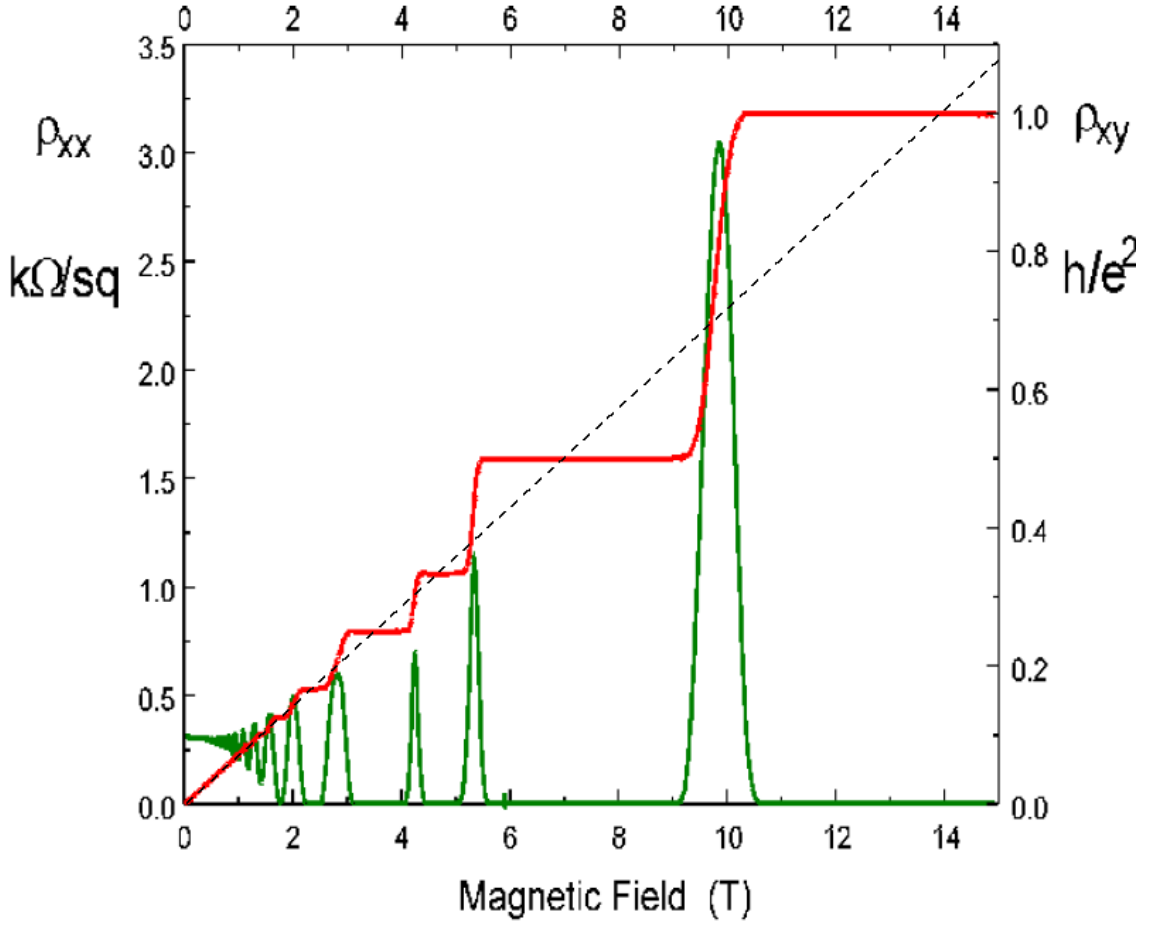
2.2.3 Integer Quantum Hall Effect

Figure 2.5: The resistivity components ρ_{xx} (green) and ρ_{xy} (red) as a function of B$_\perp$ showing the IQHE. At higher magnetic fields the remarkable property of nearly dissipationless longitudinal transport $\rho_{xx} \to 0$ and quantized Hall resistivity $\rho_{xy} = \frac{\hbar}{ie^2}$ is shown. At low B the Hall resistivity ρ_{xy} follows the classical Drude transport (dashed line) until 1 T, after which Shubnikov-deHass oscillations reflect the modification of the DOS by the magnetic field. The intersection of the classical result with plateaus correspond to integer filling factors as defined by 2.26. After ref. [38].

Assuming the Dirac-δ like DOS as given by the following expression

$$D(E) = n_L \Sigma \delta(E - E_n), \tag{2.29}$$

one would expect by solving Eq. 2.26 for B and inserting it into Eq. 2.14 the Hall resistance

would be linear in B with values of

$$\rho_{xy} = \frac{h}{ie^2}, \quad \text{where} \quad i = 1, 2, 3, ... \tag{2.30}$$

precisely at the exact magnetic field values corresponding to integer filling factors. Experimentally the Hall resistance takes on the amazing step like function form as depicted in Fig. 2.5. The resistances at integer filling factors have been broadened out into plateaus of constant resistance as given by Eq. 2.30 where they are not defined at a specific magnetic field but rather span a large range of magnetic field values. This effect discovered 25 years ago by Klaus von Klitzing [16] is known as the integer quantum Hall effect (IQHE) and has been a source of fundamental 2D physics research and practical applications up to the present day. Since the Hall resistance, as defined by the von Klitzing constant $R_K = h/e^2$, is independent of microscopic sample details and only dependent on the natural constants h and e it can be measured to an astonishing accuracy of 10^{-8} [39, 40]. This has lead to the adoption of the fixed value of $R_{K-90} = 25812.807 \, \Omega$ in 1990 as the internationally accepted value for defining the unit Ohm. The QHE is also of great importance in determining high precision values of the fine structure constant,

$$\alpha = \frac{\mu_0 c e^2}{2h}, \tag{2.31}$$

since the permittivity of vacuum μ_0 and the speed of light c are exactly defined.

A complete microscopic explanation accounting for all experimental features of the IQHE is still under intense research, however, it has been realized that a decisive ingredient of the IQHE is sample disorder. In practice the Landau levels are not Dirac-δ like in nature but are broadened into Gaussian shaped distributions by impurity disorder due to donor atoms, quantum well thickness variation, and crystalline defects. This random impurity potential can be visualized as of consisting of local valleys and hills over the area of the 2DES as depicted in Fig. 2.6.

When a lower Landau level is completely filled and extra electrons are added to the system, they will cross the cyclotron gap and become localized in the lowest energetic valleys of the next Landau level. Since these electrons are confined to small localized puddles of space on the sample they do not participate in conduction. As more electrons are added these valleys fill and increase in spatial area until different localized regions finally percolate into an extended state that connects the sample from one edge to the other allowing conduction. Therefore, in reference to Fig. 2.6, the tails of these Gaussian broadened Landau levels can be considered to consist of localized non-conducting regions and the center area as extended conducting states.

Another useful theory in explaining the features of the IQHE is an approach originally put forward by Landauer and Büttiker [41]. This method takes into account that experimentally a 2DES sample is bounded by edges. These edges lead to depletion of the local electron density and thus forms a confinement potential that bends up the Landau levels near the sample edges as displayed in Fig. 2.6. Considering the case where the Fermi energy is pinned in a localized
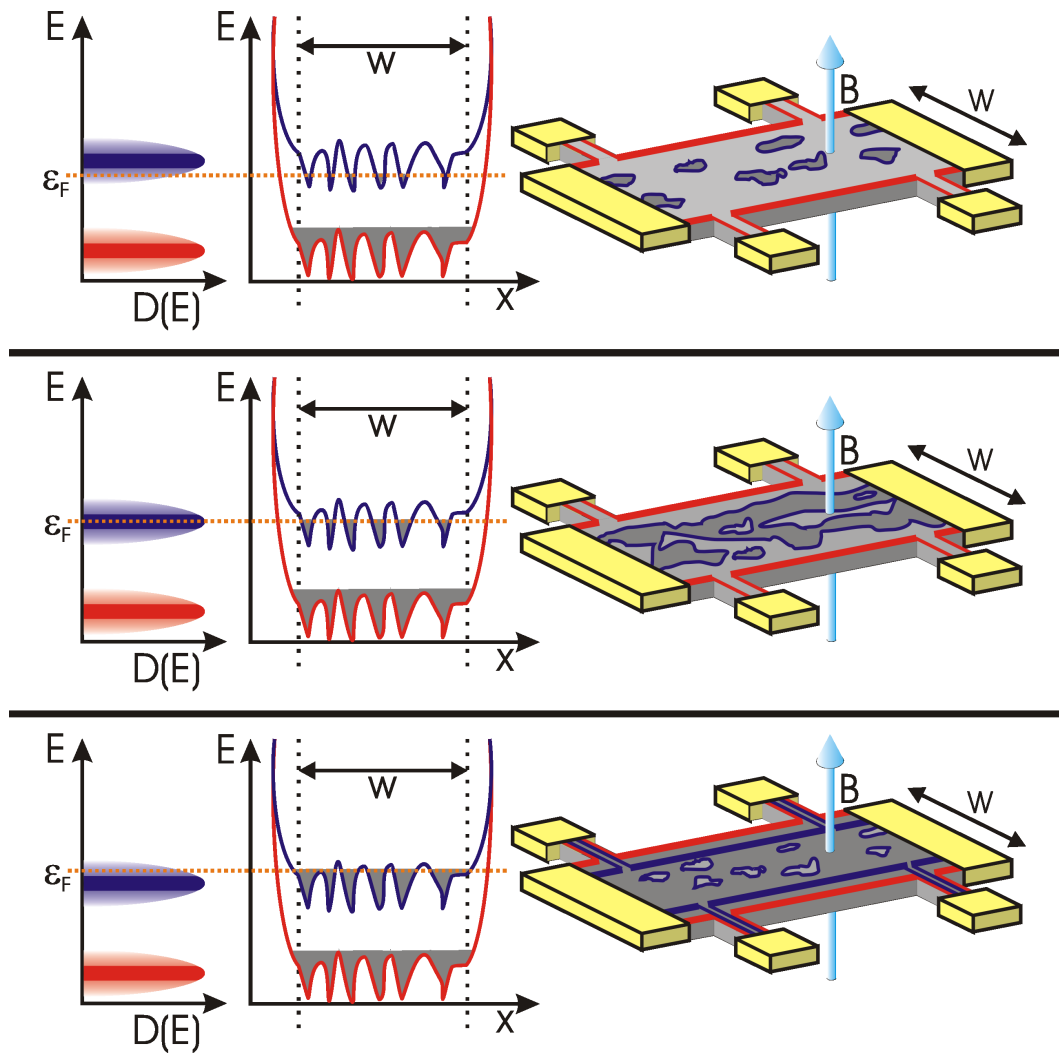
Figure 2.6: Landau level diagrams of a sample of width w for different Fermi energy ε_F positions. Disorder (shaded color) leads to gaussian broadening of the ideal Dirac-δ like LLs as shown on the left. Localized states exist in the tails of the LLs with extended states (solid color) in the middle. LLs are affected in the bulk by the disorder (middle diagrams), and curve up sharply near the edges due to sample boundaries. Top: ε_F in lower tail of second LL leads to formation of small filled localized regions within the bulk. Intersection of ε_F with the first LL near the edges leads to edge channels as indicated on the Hall bar (red). Middle: ε_F in the center of the LL leads to percolation of localized states into extended states allowing bulk transport. Bottom: ε_F in high energy tail leads again to localized states but with the formation of another edge channel (blue) on each side of the Hall bar.

region as shown in Fig. 2.6, the Landau levels which lie below the Fermi energy in the bulk will cross the Fermi energy near the sample border forming edge states. These edge states can be considered as 1D conducting channels that run parallel to the sample boundary and support dissipationless transport due to suppression of electron backscattering. The direction of electron velocity in an edge state is determined by the gradient of the confinement potential. Therefore electrons in edge channels on the opposite sides of the sample will move in opposite directions leading to a chiral symmetry. The density of states of a 1D conductor is given by Eq. 2.3 and can be equated to

$$\frac{dN}{dE} = D(E) = \frac{1}{hv_e},$$ (2.32)

where v_e is the electron velocity. From this relation it is found that each edge state contributes exactly $\frac{2e^2}{h}$ to the total conduction. Landauer and Büttiker used the edge channel concept to form a method of explaining the features describing a multi-terminal 2DES sample. Treating all sample terminals equally (voltage or current) the electrical transport in a QHS can be described in terms of transmission probabilities between the different terminals. A current I_p flowing through terminal p is expressed as a function of the voltage difference $V_p - V_q$ with respect to all other terminals q of the sample

$$I_p = \frac{2e^2}{h} \sum_q T_{qp}[V_p - V_q].$$ (2.33)

The transmission coefficients T_{qp} is the probability of scattering an electron from terminal p to terminal q and will take on the values of 0 to 1. Each fully transmitting ideal $1D$ channel will have a $T = 1$ and thus contribute a quantum $\frac{2e^2}{h}$ to the conduction.

By using the impurity potential model together with the edge state picture a qualitative explanation can be presented to describe the experimental features of the IQHE. At very low magnetic fields the DOS can still be considered independent of energy as given by Eq. 2.3 for the $B = 0$ case. This regime can be accounted for by the Drude model where the longitudinal resistance is a constant and the transverse resistance depends linearly on the magnetic field as described in Eq. 2.14 and shown in Fig. 2.5. At intermediate magnetic fields the DOS splits into Gaussian broadened Landau levels, and when the cyclotron energy gap becomes greater than the Landau level broadening, the longitudinal resistance undergoes Shubnikov-deHaas oscillations [42] where minima occur at integer filling factors. The SdH oscillations are periodic in $1/B$ and inversely proportional to the density

$$\Delta(\frac{1}{B}) = \frac{g_s e}{h n_e}.$$ (2.34)

As the magnetic field is increased to high values, the cyclotron energy and the LL degeneracy both increase as a function of B. In this case the R_{xx} minima begin to deepen and go to zero at integer filling factors, indicating that scattering processes have disappeared and that the

transport is dissipationless. This corresponds to the Fermi energy being pinned in the localized region of the Landau level, where the sample bulk is insulating and transport is confined only to occur along the $1D$ edge channels. The large localized bulk separating oppositely directed edge channels prevents backscattering resulting in zero longitudinal resistance. Since each of the two edge channel contributes exactly one $\frac{2e^2}{h}$ conduction quantum, the Hall resistance plateaus are precisely quantized at $\rho_{xy} = h/e^2$ since this is a measure of the electrochemical potential difference between the edge channels. The large magnetic field range of the Hall plateaus is due to the extent over which the Fermi energy resides in the localized regions of the Landau levels as the magnetic field increases. Therefore the plateau width is a direct signature of sample quality, where cleaner samples would have less LL broadening and thus smaller quantum Hall plateaus. As the Fermi energy enters the extended state region, bulk conduction occurs leading to a finite longitudinal resistance and a magnetic field dependent Hall resistance.

2.2.4 Fractional Quantum Hall Effect

The fractional quantum Hall effect (FQHE) was discovered in 1982 by Strömer and Tsui in a AlGaAs/GaAs heterostructure system [20, 21, 22]. This discovery was a direct consequence of advancement in epitaxial crystal growth technology and techniques leading to the production of more ideal 2DES with lower impurity concentrations. As displayed in Fig. 2.7 the QHE now exists at filling factors that are no longer integer but rather fractional, where $\nu = p/q$ with p, q being integer and where q is odd. This is surprising since in the non-interacting single electron picture no energy gap should exist below ν=1. It was soon realized that the FQHE was a direct manifestation of electron-electron correlations mediated by the Coulomb interaction leading to creation of energy gaps at the Fermi level. It is therefore necessary to include electron-electron interactions in the Hamiltonian operator defined in Eq. 2.19. Also including electron spin the full Hamiltonian now becomes

$$\hat{H} = \frac{1}{2m^*} \left[\mathbf{p} + e\mathbf{A} \right]^2 + \frac{e^2}{4\pi\epsilon_0} \sum_{j<k} \frac{1}{\vec{r_j} - \vec{r_k}} + \sum_j U(r_j) + g\mu_B \vec{B} \cdot \hat{S}, \quad (2.35)$$

where the second term accounts for the Coulomb interactions and the third term is the disorder potential. Unfortunately, an exact solution using conventional methods for this Hamilton does not exist, primarily due to the massive number of electrons $n_s > 10^{11}\ cm^{-2}$ typically involved in an experimental 2DES. In 1983 Laughlin proposed a fermionic many-body ground state trial wavefunction that was able to account for the most pronounced $\nu = 1/q$ states [23, 24],

$$\chi_{1/m} = \prod_{i<j} (z_i - z_j)^m exp[-\frac{1}{4\ell_B^2} \sum_i |z_i|^2], \quad (2.36)$$

where m is related to $\nu = 1/m$ and $z_i = x_i + iy_i$ describes the electron position in complex notation. The Gaussian term is the direct solution of the Schrödinger equation without taking
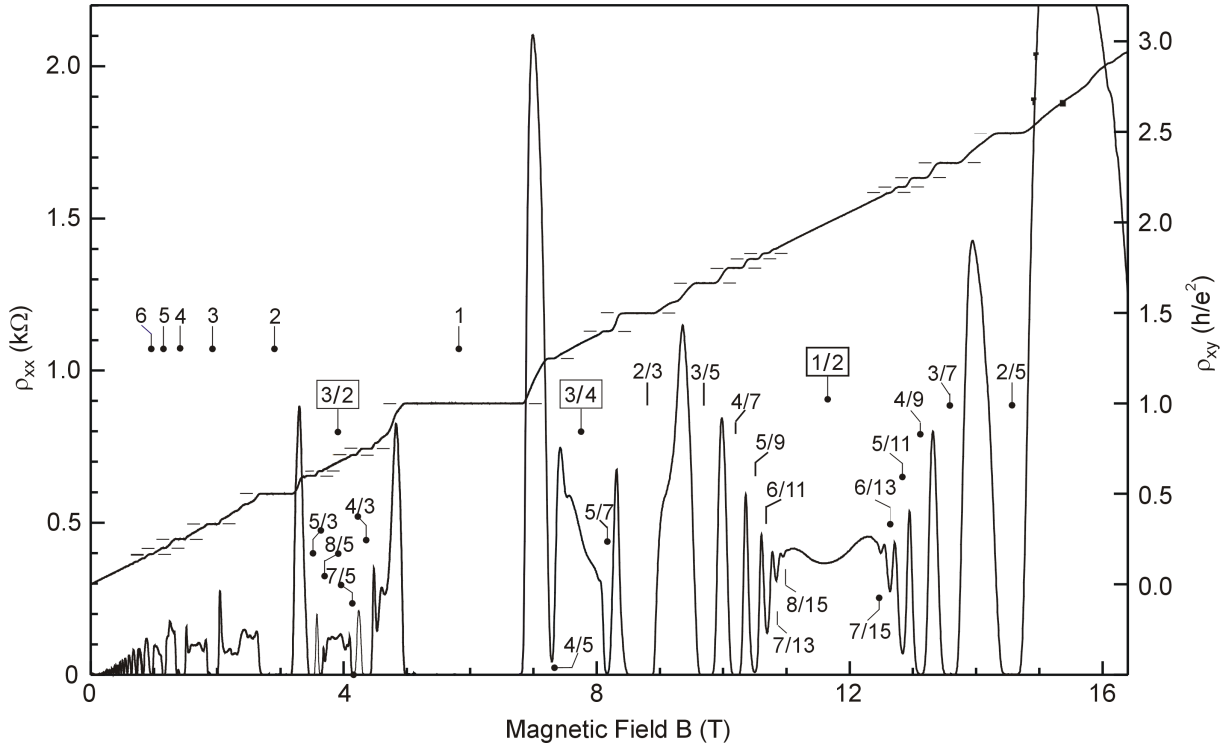
Figure 2.7: Longitudinal ρ_{xx} and Hall ρ_H resistivity components as a function of $B_\perp$ for a high quality 2DES sample. As a result of Coulomb interactions between the electrons, numerous plateaus at fractional values of h/e^2 appear in the Hall resistance, accompanied by vanishing longitudinal resistivity. These fractional states have no single electron counterpart and depend solely on strong electron correlations. Measurements performed by J.H. Smet on a sample grown by W. Wegscheider.

into account electron interactions. The functional difference from the IQHE wavefunction given by Eq. 2.21 is a result of not using the Landau gauge but rather the symmetric gauge to solve the Schrödinger equation. In this case the wavefunction has a size given by the cyclotron radius R_C and a width given by ℓ_B. The first part of the Laughlin wavefunction is know as the Jastrow term and takes into account electron-electron interactions. In the case when two electrons near each other, $z_i \to z_j$ the wavefunction probability $\chi_{1/m}$ goes to zero. Therefore it is probabilistically preferable to find the system in a state where the electrons arrange themselves in a manner as to be maximally spaced from each other. This arrangement as defined by the Laughlin equation is found to be the most energetically favorable configuration due to the Coulomb repulsive energy E_C,

$$E_C = \frac{1}{4\pi\epsilon\epsilon_0}\frac{e^2}{\ell_B}. \tag{2.37}$$

The order m of the Jastrow term specifies how quickly the probability will decay as electrons approach each other. At $\nu = 1/3$ there is a 3:1 ratio of the magnetic flux piercing the 2DES to the number of electrons. Here the three complex zeros of the Jastrow term are assigned as follows: one zero due to the Pauli exclusion principle and the other two correspond to magnetic flux quanta. Even though a magnetic flux quantum can be located anywhere it is most energetically favorable for the system when two flux tubes attach themselves at the position of each electron z_j. Therefore the wavefunction of an electron located at z_i will see three complex zeros for every other electron located at z_j. This leads to a homogeneous incompressible state in the LLL where the electrons avoid each other to lower the overall system energy.

Figure 2.8: The left diagram is an uncorrelated Poisson distribution of 1000 charged particles whereas the right displays the same amount of particles as distributed by the Laughlin wave function for $m = 3$. The right is calculated using a Monte Carlo simulation that is allowed to converge to an equilibrium. At equilibrium it is found that the configuration generated are distributed according to $|\Psi|^2$. Adapted from Laughlin [43].

To further illustrate how the Laughlin state leads to overall system correlations it is useful to consider Fig. 2.8 which compares how N=1000 electrons subjected to either an uncorrelated random Poisson distribution or to the Laughlin wave function for $m = 3$ will be distributed after many iterations. The Laughlin distribution is obtained by a Monte Carlo sampling of $|\chi_{1/3}|^2$ for random trail moves of the particles to new positions where a move that increases the value of $|\chi_{1/3}|^2$ is accepted. After equilibrium it is seen that the particles are distributed as according to the Laughlin state $|\chi_{1/3}|^2$. Comparison of the simulation to the random Poisson distribution shows that the Laughlin state suppresses particle density fluctuations at long wavelengths leading to greater individual particle neutrality that reduces overall system energy.

Laughlin considered the FQHE as evidence supporting the existence of fractionally charged quasiparticles with charge $e^* = e/q$ where q is an integer [23, 24]. These quasiparticles do not obey Fermi-Dirac or Bose-Einstein statistics but rather anyonic statistics. Indeed the exact

quantization of the finite Hall plateaus and longitudinal resistance minima is analogous to the IQHE if Laughlin quasiparticles are substituted for electrons. To account for filling factors $\nu = 1 - 1/q$ electron-hole symmetry arguments are used to describe these states in terms of quasi-holes [44]. The quasi-hole wavefunction is

$$\chi_{qh} = \prod_i (z_i - z_0)\chi_{1/m},\tag{2.38}$$

where a flux quantum is introduced at z_0 [45]. Experimental evidence supporting the existence of fractionally charged quasiparticles has been seen in shot noise [46] and tunnel [47] experiments.

Unfortunately there are many shortcomings of the Laughlin picture in describing the fractional features of Fig. 2.7. To explain the existence of $\nu = 1 - 1/q$ states a complex hierarchical scheme involving Laughlin states recursively built from Laughlin quasiparticles instead of electrons is necessary. In addition accounting for fractional states in the next higher Landau level (N=1) using Laughlin states results in very complicated wavefunctions that are unable to account for the relative strength of the FQHE states as shown by experiment. Also there exists unusual even fractions which conflict with the Laughlin quasiparticle theory.

Composite Fermions

Failure of the Laughlin quasi-particle theory to account for the state ν=1/2 and the relative intensities of FQHE states based on the hierarchical model led Jain in 1989 to reformulate the FQHE in terms of a new quasi-particle termed the "composite fermion" [48, 49]. Based on the symmetry and the appearance of Shubnikov-deHaas like oscillations at ν=1/2, Jain proposed that composite fermions existed at a zero effective magnetic field B_{eff} at ν=1/2 and formed into discreet CF LLs as the effective magnetic field is increased

$$B_{eff} = B \left(1 - 2\nu\right),\tag{2.39}$$

where B is the real magnetic field and ν is the IQHE filling factor. This approach has greatly simplified the interpretation of the FQHE by allowing it to be explained in terms of IQHE concepts.

The basic building blocks of a CF is the replacement of Coulomb interactions by the attachment of statistical flux tubes to each electron. The attachment of flux tubes relates to the fact that magnetic flux quanta are preferably located at the positions of the electrons as seen in the Laughlin wavefunction. It is found that the flux quanta attachment occurs in even pairs, allowing CF electrons to be dressed with $n = 2, 4, 6, etc...$ flux tubes. Since the CF is composed of an electron with an even number of attached flux quanta it has a charge of e^- and obeys Fermi-Dirac statistics unlike the fractionally charged Laughlin quasi-particles.

The concept of $B_{eff} = 0$ at $\nu=1/2$ defines a CF groundstate that is metallic and filled up to the Fermi wave-vector in a similar way as a 2DES at zero magnetic field. The CF wavevector is therefore

$$k_F^{CF} = \sqrt{\frac{4\pi n_s}{g_s}},\qquad(2.40)$$

where unlike the single electron case Eq. 2.6 the spin degeneracy $g_s = 2$ is removed since electron spin is subjected to the total magnetic field and therefore the CF LLs are spin split. As stated previously, movement of the magnetic field away from $\nu= 1/2$ causes a non-zero B_{eff} leading to the formation of CF LLs where each CF LL is energetically separated by

$$\hbar\omega_C^* = \hbar\frac{eB_{eff}}{m_{CF}^*} = C_C E_C,\qquad(2.41)$$

where m_{CF}^* is the CF effective mass, C_C is a constant scaling prefactor, and E_C is the Coulomb correlation energy as defined in Eq. 2.37. Similar to the non-interacting IQHE electron LLs, the FQHE LLs also undergo Gaussian broadening due to disorder. Since the CF energy gaps are much smaller than the IQHE, higher sample quality and lower temperatures are therefore needed to observe the FQHE. Due to the Coulomb correlation energy, E_C the CF cyclotron gap scales as $\sqrt{B}$ as opposed to that of electrons which scales linearly with B. Analogous to the single electron cyclotron radius (Eq. 2.22), a CF cyclotron radius can be defined using B_{eff} as

$$R_n^{CF} = \ell_B\sqrt{2n+1} = \frac{\hbar k_F^{CF}}{|e|B_{eff}}.\qquad(2.42)$$

Cyclotron resonance experiments at $\nu=1/2$ have confirmed the existence of a CF fermi surface, allowing for a determination of an effective mass value that is generally 10 times larger than the normal effective mass in GaAs [50].

The CF-LLs are defined at

$$E_n = (n + \frac{1}{2})\hbar\omega_{C^*} \pm \frac{1}{2}g^*\mu_B B.\qquad(2.43)$$

Therefore, as in the IQHE case

$$\nu_{eff} = \frac{n_s h}{eB_{eff}} = \frac{n_s \Phi_0}{B_{eff}} \quad\text{where}\quad \nu = \frac{\nu_{eff}}{2\nu_{eff}\pm 1},\qquad(2.44)$$

where the IQHE of composite fermions occurs exactly at the same magnetic field position as the FQHE.

As seen in Fig. 2.7 the Hall resistance at $\nu=1/2$ is $\rho_{xy} = 2h/e^2$ and not zero as would be expected for B_{eff}. This can be treated using a simple argument if one considers that each composite fermion carries two flux tubes, then by Faraday's law

$$R_{xy} = \frac{EMF}{I} = \frac{d\Phi/dt}{I} = \frac{d\Phi}{dQ} = \frac{2\Phi_0}{e} = \frac{2h}{e^2}.\qquad(2.45)$$

Electron correlations in Landau levels (N=0,1) give rise to the FQHE, however, for Landau levels greater than $N \geq 2$ the FQHE has never been observed. The existence of completely filled lower LLs is thought to modify the Coulomb potential leading to a competition between long range repulsive and short range attractive Coulomb interactions [51]. This results in ground states with fragile long range order known as the stripe and bubble phases [52].

Chapter 3

Two-Dimensional Electron Bilayer Systems

This chapter discusses the basic concepts and theoretical background of a 2DES bilayer. The first section Sec. 3.1 introduces the concept of a bilayer 2DES and discusses some of the basic parameters used to describe such systems. In the next two sections the theory and experiments as related to high (Sec. 3.2) and low (Sec. 3.3) interlayer tunneling systems are discussed. For the case of low interlayer tunneling it is found that bilayers are able to support a unique excitonic superfluidic state at a total filling factor ν_T=1.

3.1 The Bilayer System

A bilayer system is formed when two charge carrier layers are brought in close proximity to each other. The charge carrier layers can consist of two dimensional electron systems (2DES), two dimensional hole systems (2DHS) or a combination of one 2DES with one 2DHS. Typically formed using two closely spaced quantum wells, the average interlayer separation between the two charge carrier layers is parameterized by the center-to-center quantum well distance d. At sufficiently small values of d, layer to layer carrier interactions begin to manifest through tunneling and Coulomb interactions.

Considering a single electron within the bilayer system, the electron's Hilbert space can be defined as

$$u|upper\rangle + v|lower\rangle = (uc^\dagger_{upper} + vc^\dagger_{lower})|0\rangle \quad \text{where} \quad |u|^2 + |v|^2 = 1, \quad (3.1)$$

where $|upper\rangle$ and $|lower\rangle$ correspond to the two basis eigenstates of the upper and lower layer respectively, and where $c^\dagger_{upper}$ and $c^\dagger_{lower}$ are fermion creation operators for the different layers acting on the vacuum state $|0\rangle$. The probability of finding the electron in one of the basis states is given by $|u|^2$ and $|v|^2$ for the upper and lower layers, respectively.
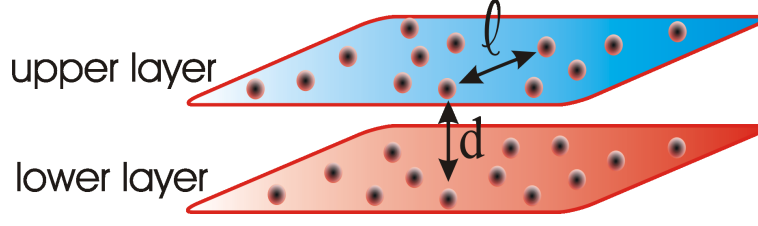
Figure 3.1: Pictorial representation of a 2DES bilayer system showing the upper layer (blue) and lower layer (red). The average mean intralayer electron separation is parameterized by the magnetic length ℓ_B whereas the interlayer electron separation is given by the center-to-center quantum well distance d.

Upon application of a perpendicular magnetic field $B_\perp$ with respect to the 2D planes the two QW electron Fermi seas will become quantized into Landau levels with energy eigenvalues as defined by Eq. 2.28. For the condition where the magnetic field and electron densities have been tuned to give balanced layer densities with all electrons existing in the lowest spin split Landau level, one has the situation where the electron kinetic energy in the two layers is quenched and all electrons are completely degenerate in energy. This changes the system from a non-interacting 2DES at $B = 0$ to a system where each electron experiences a Coulomb interaction between other electrons at different positions $z = x + iy$. The Coulomb interactions can be between electrons within the same layer (intralayer) or between electrons from the two different layers (interlayer). These intralayer and interlayer Coulomb interactions can be expressed as

$$E_C = \frac{e^2}{4\pi\epsilon\ell_B} \quad \text{and} \quad E_d = \frac{e^2}{4\pi\epsilon d}, \tag{3.2}$$

where the mean intralayer electron layer spacing is given by the magnetic length $\ell_B = \sqrt{\frac{\hbar}{eB}}$ and d is the previously mentioned center-to-center QW distance. The ratio $E_d/E_C = d/\ell_B$ can be used as a parameter to characterize the relative importance of the intralayer and interlayer Coulomb energies. It should be noted that only E_C is a function of applied B, whereas E_d is fixed by the boundary conditions of the sample. At large d/ℓ_B the system will behave as two independent single layers that have infinite separation between them. In this case each electron has a unitary probability of only existing in the $|upper\rangle$ or the $|lower\rangle$ eigenstate. However, as the d/ℓ_B ratio is lowered the two layers can interact with each other producing a new state where an electron at position $z = x + iy$ can exist in both layers simultaneously!

3.2 High Interlayer Tunneling Systems

At $B_\perp = 0$ the tunneling coupling is a function of the potential barrier height and thickness. As the potential barrier between the two quantum wells is lowered the probability of an electron
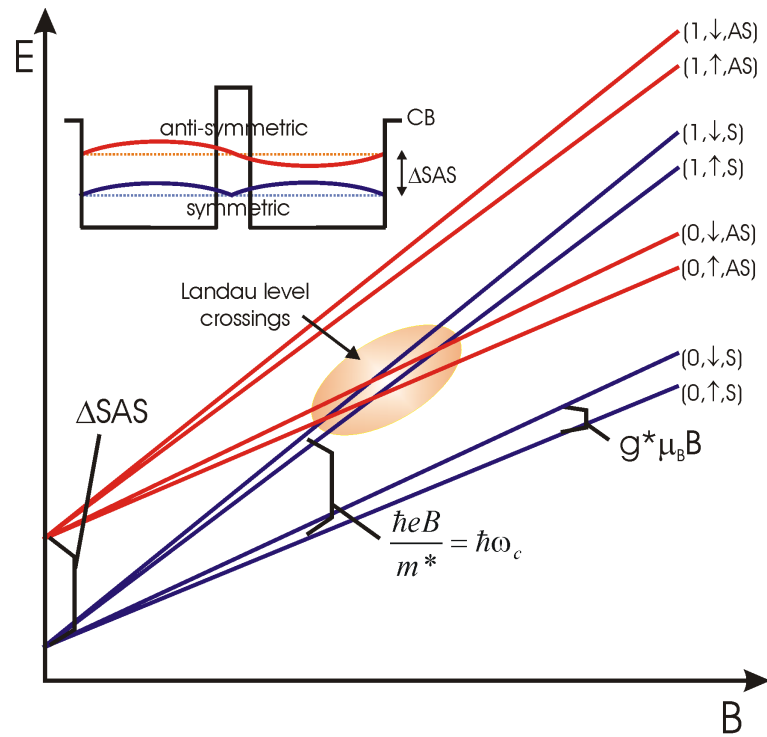
Figure 3.2: Graph showing the symmetric (S) and anti-symmetric (AS) subband states separated by an energy $\triangle_{SAS}$ for a strongly tunneling bilayer system. The inset shows that the anti-symmetric state is higher in energy than the symmetric state. The graph shows the formation of two LL fan diagrams separated by $\triangle_{SAS}$ at $B = 0$ for both S and AS subbands. Each Landau level has three quantum numbers corresponding to LL index, spin, and subband.

to tunnel from one layer to the other is enhanced. This leads to an electron eigenstate $\Psi_z = u|upper\rangle + v|lower\rangle$ with both u and v nonzero, defining a probability of an electron existing in both of the quantum wells. In the balanced electron layer case this eigenstate can be symmetric with respect to the potential barrier $u = v$ or anti-symmetric $u = -v$ as depicted in Fig. 3.2. The symmetric (S) eigenstate assumes a lower eigenenergy than the antisymmetric (AS) eigenstate leading to the formation of an energy gap that is denoted $\triangle_{SAS}$. As the strength of the tunneling is increased the energy gap between the symmetric and antisymmetric eigenstates widens leading to a greater $\triangle_{SAS}$. For large $\triangle_{SAS}$ the electrons tunnel back and forth so rapidly between the two layers that the bilayer system acts as a single wide QW. The tunnel splitting $\triangle_{SAS}$ is then analogous to the electric subband splitting in a single well. Therefore, since the symmetric state is lower in energy than the antisymmetric state, all the electrons will occupy this lower lying state.

Applying a $B_\perp$ will quantize both the symmetric and the antisymmetric DOS into discreet

Landau levels as shown in Fig. 3.2. The LL energy as a function of B can be represented using two Landau level fan diagrams separated by the sub-band splitting $\triangle_{SAS}$. Now, in addition to the orbital ($n = 0, 1, 2, 3, ...$) and spin ($\uparrow, \downarrow$) quantum numbers, each LL has an additional subband index (S,AS). In experimental magneto-transport measurements the co-existing symmetric and antisymmetric states lead to a beating in the longitudinal resistivity component ρ_{xx}. A Fourier transformation can be used to obtain the separate electron densities n_S and n_{AS} allowing a determination of $\triangle_{SAS}$,

$$\Delta SAS = \frac{\pi \hbar^2}{m^*}(n_S - n_{AS}). \tag{3.3}$$

In addition, when the cyclotron energy $\hbar\omega_C$ is in general much greater than $\triangle_{SAS}$, $\triangle_{SAS}$ can be determined by temperature activated transport studies of ρ_{xx},

$$\rho_{xx} = \rho_0 e^{\frac{-\triangle_{SAS}}{kT}}, \tag{3.4}$$

where k is the Boltzman constant and ρ_0 is a proportionality constant.

Since strong tunneling will lead to all the electrons occupying the lower energy symmetric state, the formation of an incompressible IQHE state will no longer be dependent on the single layer electron density equaling the LL degeneracy eB/h as discussed in Sec. 2.2.2, but rather on the total electron density ($n_T = n_{upper} + n_{lower}$) equaling eB/h. Therefore, the transport measurements will show a minimum in ρ_{xx} and a quantized $\frac{h}{ie^2}$ Hall plateau in ρ_{xy} only at even filling factors due to the contribution of electrons from both layers,

$$\nu_T = \frac{hn_T}{eB} = \frac{2hn}{eB}, \tag{3.5}$$

where both layers have equal electron densities and n is the single layer density. At ν_T=1 precisely one electron occupies each spatial position z in both layers simultaneously due to the strong tunneling, this will therefore correspond to a completely filled Landau level. The multiparticle wavefunction can be written as

$$\Psi = \prod_k (uc_{upper}^\dagger + vc_{lower}^\dagger)|0\rangle. \tag{3.6}$$

Similar to ν=1 for the single layer case the ν_T=1 equation simply corresponds to a completely filled Landau level of electrons but with the exception that electrons now exist in a superposition of the two layer eigenstates. This equation is the exact ground state for bilayer systems with large tunneling [53] and just corresponds to the ordinary ν=1 integer quantum Hall effect where collective electron correlations between the layers are irrelevant. What is not so obvious is that under certain conditions this wavefuction also survives in the limit of zero tunneling!
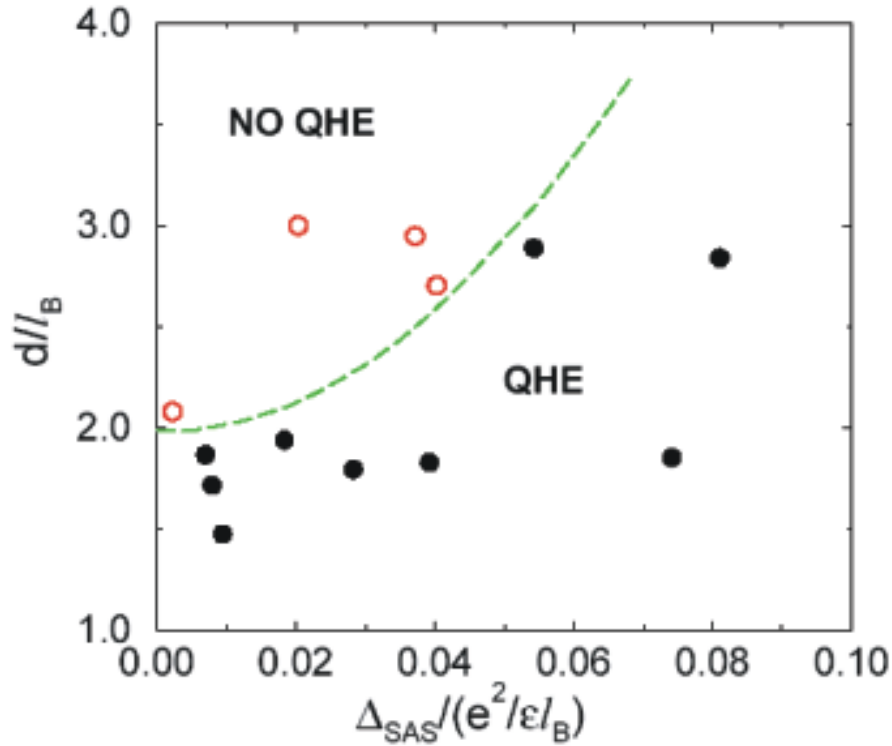
Figure 3.3: Phase diagram where the dashed line separates the coupled phase coherent ν_T=1 state and the uncoupled separate layer ν= 1/2 states as a function of d/ℓ_B versus $\triangle_{SAS}$. Data points correspond to experimental measurements by Murphy et al. [54].

3.3 Low Tunneling Systems

In the limit as the tunneling goes to zero, $\triangle_{SAS} \rightarrow 0$, the symmetric and antisymmetric states converge to the same energy value, and it is not intuitively expected that the layers would show coherence. However, at low d/ℓ_B ratios, it was predicted [27] that electron-electron interactions should lead to a superposition of states and that Eq. 3.6 should remains a valid description. This is shown by the phase diagram in Fig. 3.3, where the dashed line indicates the distinction between the strongly coupled ν_T=1 phase coherent state and the weakly coupled individual case, where both layers are approximately at ν=1/2. To the far right of the phase diagram, the single particle tunneling will dominate over the Coulomb energy, leading to a single particle IQHE as discussed in Sec. 3.2.

This cross-over of the single-particle at high $\triangle_{SAS}$ to a collective gap is visible in experiments done by Murphy et al. [54] where the interlayer tunneling strength was tuned using a

parallel magnetic field, $B_\parallel$ as according to [55],

$$\triangle_{SAS}(\theta) \approx \triangle_{SAS} e^{-(\frac{dB_\parallel}{2\ell_B B_\perp})^2},$$
(3.7)

here $\triangle_{SAS}$ is the $B_\parallel = 0$ single particle tunneling gap energy, $\frac{B_\parallel}{B_\perp} = \tan\theta$ relates to the sample tilt angle, d is the center to center QW spacing, and ell_B is the magnetic length. The $\nu_T = 1$ state measured by thermally activated transport depicted in Fig. 3.4 survives even when $\triangle_{SAS} \to 0$.
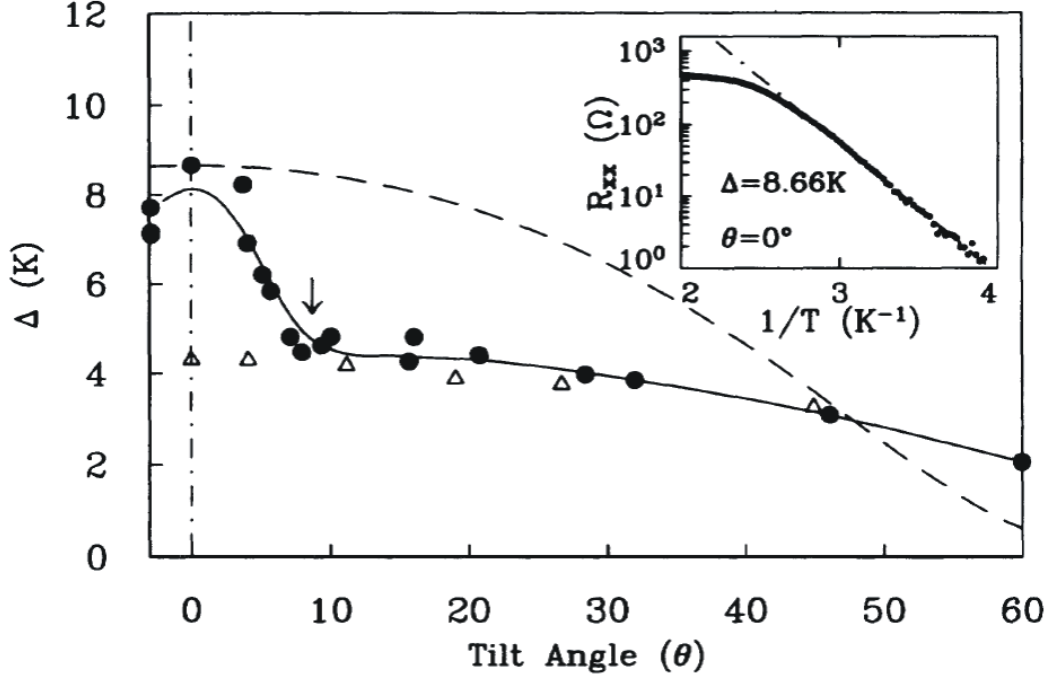
Figure 3.4: Charged activaton energy gap measurements for an electron bilayer sample with $\triangle_{SAS} = 0.8$ K as a function of different sample tilt angles. Activation energies are obtained by temperature dependent measurements of R_{xx} as shown in inset. Solid circles are for $\nu_T = 1$ and open triangles are for $\nu_T = 2/3$. Even for high tilt angles ($\triangle_{SAS} \to 0$) the $\nu_T = 1$ survives. Murphy et al. [54].

3.3.1 Halperin (111) State

The wavefunction Eq. 3.6 can be written down in first quantized form as

$$\Psi = \prod_k (uc^\dagger_{upper} + vc^\dagger_{lower})|0\rangle \otimes \Psi_{Filled\ LLL},$$
(3.8)

where the first term is the isospin or layer degree of freedom (u, v) and can account for an electron being in a superposition of the upper and lower layers. The second term is the positional
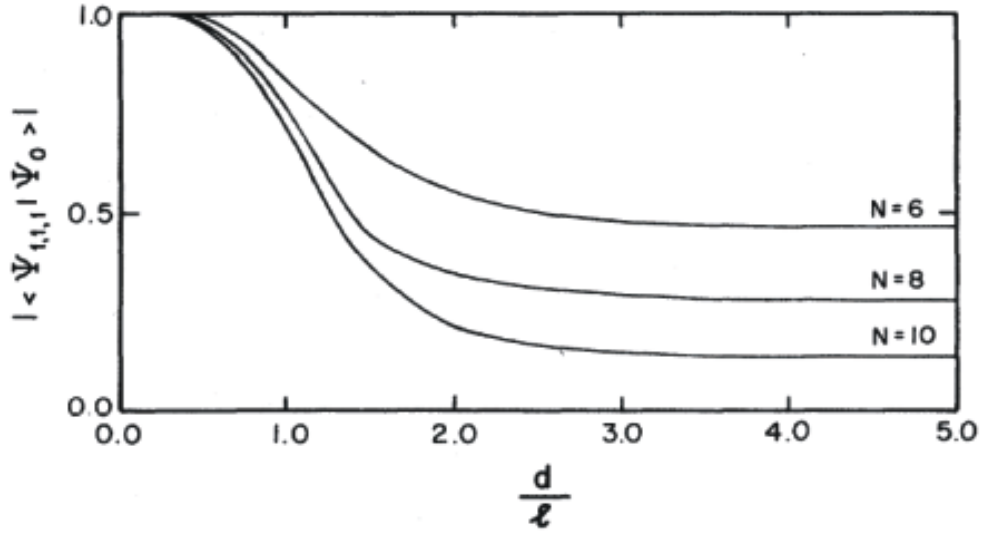
Figure 3.5: Overlap between the exact ground-state wave function Ψ_0 and the (111) state as a function of d/ℓ for $\nu_T = 1$. Three plots corresponding to a total electron number of $N = 6, 8, 10$ are shown. Yoshioka et al. [56]

degree of freedom of the electron within the layer. In the radial gauge the positional degree wave function of a completely filled Landau level can be expressed by the Laughlin wave function where $m = 1$,

$$\Psi_{Filled\ LLL} = \prod_{i<j} (z_i - z_j) e^{-\frac{1}{4\ell_B^2} \sum_i |z_i|^2}. \tag{3.9}$$

The layer degree of freedom in Eq. 3.8 can be reformulated using a generalization of Laughlin's wavefunction by Halperin [25]. This wavefunction was first formulated by Halperin over 20 years ago to account for systems with two different electron spin Landau states existing at the same energy [1]. Replacing the two LL spin states by the two layers allows the first quantized form to be expressed as

$$\Psi_{111} = \prod_{i<j} (z_i - z_j) \prod_{i<j} (w_i - w_j) \prod_{i<j} (z_i - w_j) \, e^{-\frac{1}{4\ell_B^2} \sum_i |z_i|^2} e^{-\frac{1}{4\ell_B^2} \sum_i |w_i|^2}. \tag{3.10}$$

In this case z and w represent the spatial coordinates of the upper and lower layers, respectively. As in the single layer case, the wavefunction goes to zero whenever $z_i \to z_j$ or $w_i \to w_j$. What is surprising is the third Jastrow term, which states that even though electrons z and w exist in different layers, the wave function will still goto zero whenever electrons in different layers approch each other, $\Psi_{111} \to 0$ as $z \to w$! Therefore, electrons avoid each other not only in

---

[1]Such a system is formed when two spin split Landau levels cross, forming a state composed of both spin up and spin down electrons at the same energy [57].

the same layer but also electrons in the other layer, leading to a state where each positional degree of freedom is filled either by an electron in the z-layer or the w-layer. This completely filled Landau level is energetically optimal and will lead to an energy gap even in the absence of interlayer tunneling. This wavefunction was termed the (lmn) state where "lm" denote the number of statistical flux tubes per electron in each layer, and "n" denotes the number of flux tubes per quasi-hole in one layer shared with quasi-electron in the other layer. As shown in Fig. 3.5, Yoshioha et al. [56] have compared exact numerical solutions of the bilayer Hamiltonian for very small electron bilayer systems ($N \approx 10$) to the (111) wavefunction. Here overlap between the two solutions is seen to occur when the d/ℓ ratio goes below a critical value.

3.3.2 Pseudospin Picture

Returning to the Laughlin wavefunction for $m = \frac{1}{\nu} = 1$,

$$\chi_1 = \prod_{i<j}(z_i - z_j)e^{-\frac{1}{4\ell_B^2}\sum_i |z_i|^2} \tag{3.11}$$

the wave function can be rewritten in second quantization form as

$$\chi_1 = \prod_k c_k^\dagger |0\rangle, \tag{3.12}$$

where k labels the single particles states. In this form the state is a simple Slater determinant. It is also possible to rewrite the (111) state as a single layer Laughlin function for $m = 1$ which is analogous to Eq. 3.11 but with the exception that there now exists an uncertainty as to which layer the electrons are in,

$$\Psi = \prod_{i<j}(z_i - z_j)\,e^{-\frac{1}{4\ell_B^2}\sum_i |z_i|^2} \otimes | \rightarrow\rightarrow\rightarrow \dots \rightarrow\rangle \quad \text{where} \quad |\rightarrow\rangle = u|\uparrow\rangle + e^{i\phi(X)}v|\downarrow\rangle, \tag{3.13}$$

where the first part containing the Jastrow and Gaussian terms are antisymmetric and spins are all symmetric. Here the two eigenstates $|upper\rangle$ and $|lower\rangle$ have been rewritten in spin-1/2 language using pseudospin up ($|\uparrow\rangle$) to denote an electron in the upper layer and pseudospin down ($|\downarrow\rangle$) to denote an electron in the lower layer [26]. The two eigenvalues (u, v) relate to the probability of finding an electron in the $|\uparrow\rangle$ or $|\downarrow\rangle$ state, respectively, and have a combined probability of $|u|^2 + |v|^2 = 1$. Exchange interactions will favor the same pseudospin state $|upper\rangle + e^{i\phi}|lower\rangle$ for all electrons, where the phase ϕ is uniform and in the absence of tunneling arbitrary. As depicted in Fig. 3.6 the symbol ϕ relates to the azimuthal angle with the spin components S_x and S_y. The z-component S_z of the pseudospin is given by the polar angle θ, where $\langle S_z \rangle \propto |u|^2 - |v|^2$ and represents the density imbalance between the layers. This quantity is fixed by the interlayer bias, and any variation of $\langle S_z \rangle$ from a fixed value will cost capacitive energy.
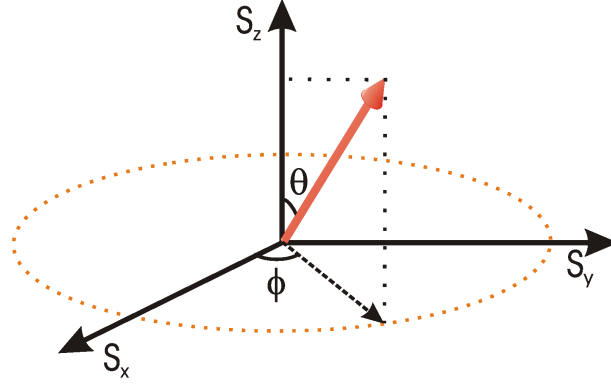
Figure 3.6: Psuedospin representation of the (111) state. The azimuthal angle ϕ is the global phase parameter of the (111) state and has the components S_x and S_y. The polar angle θ represents the density imbalance between the layers where $\langle S_z \rangle \propto |u|^2 - |v|^2$.

In the case of zero tunneling all possible orientations of ϕ are equivalent meaning that the system is completely degenerate for $0 < \phi < 2\pi$, the only requirement is when a particular phase is chosen the same phase will exist at all other spatial points in the bilayer system. This is known as a spontaneous breaking of the system symmetry. In comparison, a superconductor also spontaneously breaks the gauge symmetry associated with total charge carriers through the formation of Cooper pairs. Here the (111) state is an incompressible QHE with a fixed total charge, however, due to the uncertainty of electron charges existing in the upper or lower layer, the breaking of the symmetry in now associated with charge difference.

The order parameter associated with the (111) bilayer state is defined as

$$\psi(z) \equiv \langle \Psi_\uparrow^\dagger \Psi_\downarrow \rangle = uve^{i\phi(z)} = \frac{n_0}{2}e^{i\phi(z)}, \tag{3.14}$$

where z is the in-plane spatial coordinate. The order parameter is the expectation value of an operator that removes an electron from one layer and places it into the other layer. It is therefore possible to transfer an electron from one layer to the other layer and still be in the same quantum state. If the system is still in the same quantum state, the energy change is zero. Therefore, in the case of tunneling experiments, the process conserves energy only if the bias voltage between the upper and lower layer is zero. Similar to a superconducting Josephson junction, it was predicted early on that at zero bias an enormous anomaly in the conductivity should occur [27, 58, 59]. The tunneling operator for the current passing through the layers can be expressed as

$$j_{\uparrow\downarrow z} = -it(\Psi_\uparrow^\dagger \Psi_\downarrow - \Psi_\downarrow^\dagger \Psi_\uparrow) \tag{3.15}$$

and has an expectation value of

$$\langle j_{\uparrow\downarrow z} \rangle = -it(\Psi_z^* - \Psi_z) = 2tuv\sin(\phi(z)), \tag{3.16}$$

which is similar to a DC Josephson current where the tunneling depends only on the phase and not on the potential bias between the layers! Experiments [3] have indeed observed such a zero bias peak as shown in Fig. 3.7, nevertheless, some noticeable differences from an ideal DC Josephson peak exist in that the experimentally peak has a finite height and width. Various theories [60, 61] involving a finite phase coherence time or sample inhomogeneity have been proposed to explain this finite height and width but no conclusive agreement has of yet been obtained.
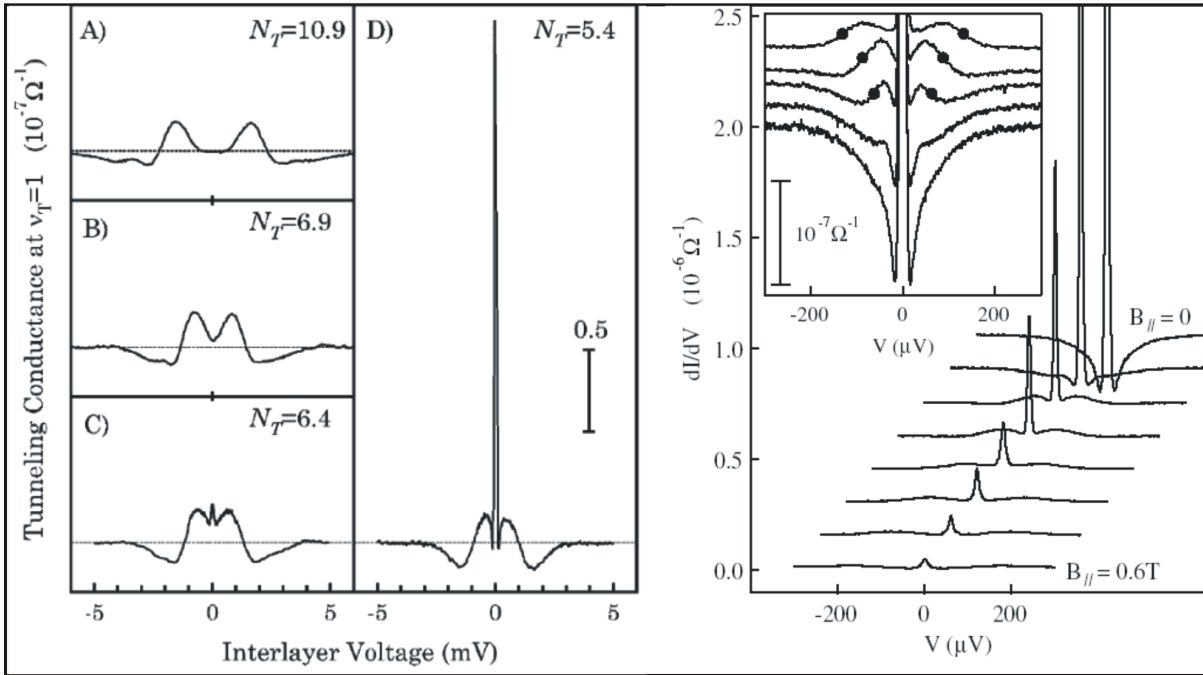
Figure 3.7: On the left is shown the emergence of the ν_T=1 zero bias peak in the differential conductivity dI/dV as the d/ℓ ratio is lowered. The two satellite peaks are due to resonant tunneling. The right graph is a plot of the zero bias peak for different parallel magnetic fields $B_\parallel$ values. The inset is a magnification showing a linearly dispersing Goldstone mode as indicated by the solid circles. Data measured by Spielman et al. [3, 62].

When the global phase ϕ varies as a function of spatial position in a system with a spontaneously broken symmetry, there will exist a Goldstone mode corresponding to long wavelength, low energy variations of the broken variable. At zero tunneling this Goldstone mode is gapless and has a linear dispersion relation with wave vector q [27, 58]. Application of a parallel magnetic field $B_\parallel$ with respect to the layers will induce a spatial variation in the phase ϕ where $q = eB_\parallel d/\hbar$. This can be detected by tunneling spectroscopy experiments [62] as shown in Fig. 3.7 where a $B_\parallel$ splits the zero bias tunneling peak into two resonances symmet-

ric about $V = 0$ [60, 61]. These resonance peaks should occur at the Goldstone mode energy $eV = \pm\hbar\omega(q)$ at the parallel field-induced wave vector q. Plotting $\hbar\omega(q)$ versus $q = eB_{\parallel}d/\hbar$ shows a linear dispersion where from the slope a dispersion velocity of $1.4 \times 10^4 \ m/s$ is obtained [62]. This is believed to offer experimental evidence showing the existence of a linearly dispersing collective mode that is characteristic of the predicted Goldstone mode. Though finite interlayer tunneling will open a gap Δ_0 at $q = 0$ for this mode, it is predicted, if small enough, the tunneling should not destroy the state [63]. Discrepancies with the proposed theoretical models include the persistence of the zero bias tunneling peak to large $B_{\parallel}$ values.
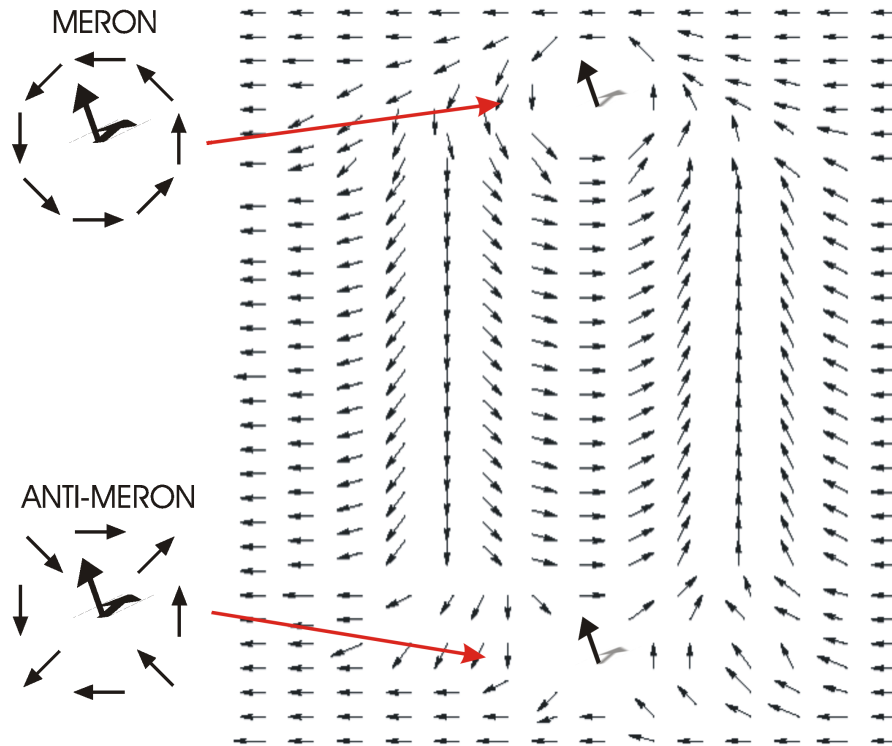
Figure 3.8: A meron and an anti-meron pair connected together by a domain wall. Such topological defects will form into pairs to reduce over all system energy.

The broken-symmetry state can support excitations that can be viewed in the pseudospin ferromagnetic picture as consisting of stable topological defects called merons and anti-merons as sketched in Fig. 3.8. Merons and anti-merons consist of a pseudospin pointing positively or negatively out of the xy-plane, respectively. A positive flavored meron would correspond to an electron entirely localized in the upper layer whereas a negative flavor to an electron in the bottom layer. As depicted in Fig. 3.8 the pseudospins phase can wind in a clockwise direction around the core creating a positive vorticity meron or in an anti-clockwise direction leading to

a negative vorticity anti-meron. As one moves away from the core the pseudospins fall away in a gradual rate relaxing back into the xy-plane. In addition, merons and anti-merons carry a charge of $\pm e/2$, where the sign is determined as a product of the vorticity and flavor. In total, four different types of merons are possible consisting of the attributes related to direction (upper/lower), vorticity (clockwise/anti-clockwise), and charge (negitive/positive).

A single meron will strongly modify the global phase over a long range, and therefore has a high energy cost since $E \sim |\nabla\phi|^2$. It is therefore energetically optimal for oppositely charged merons to form meron/anti-meron pairs as shown in Fig. 3.8. Here the pairs are electrically neutral and have a zero vorticity, and thus only create a local disturbance in the order parameter.

Below a critical temperature, known as the Kosterlitz-Thouless temperature T_{KT}, free energy considerations keep merons and anti-merons bound in neutral, zero vorticity pairs. In this regime a 3D system should show zero resistance and infinite conductivity in linear response up to a critical current. Unlike a 3D system, a 2D system will only display zero resistance and infinite conductivity in the limiting case as $T \to 0$. The $V - I$ below T_{KT} is predicted to be

$$V \propto I^P \quad \text{where} \quad P = 1 + 2\frac{T_{KT}}{T}, \tag{3.17}$$

where $p = 3$ at $T = T_{KT}$. At T_{KT} the pairs become unbound and the phase coherence is lost, destroying the superfluidic state, and a jump is expected to occur as the system reverts back to its normal $V - I$ linear response state. Above T_{KT} the $V - I$ relationship will again be ohmic so there should exist a discontinuity at $T = T_{KT}$ from $p = 1$ to $p = 3$. This is the well known Kosterlitz-Thouless transition [64] and if found experimentally would be the first finite-temperature phase transition in a quantum Hall system [63].
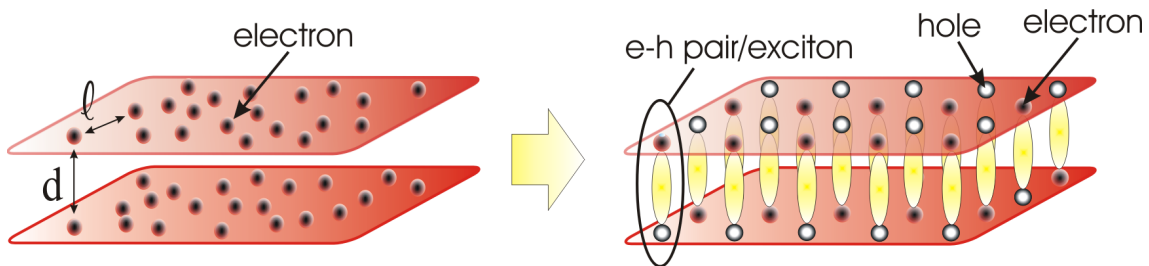
3.3.3 Exciton Picture

Figure 3.9: As the intralayer electron distance ℓ approaches the interlayer distance d, the electrons will optimally avoid each other to reduce overall system Coulomb correlation energy. As shown in the right, each electron is then placed opposite to an empty state or hole leading to e-h pair or exciton formation.

In addition to the Halperin (111) and pseudospin pictures, the ν_T=1 state can be equivalently expressed as a Bose-Einstein condensate of electron-hole pairs [27, 28, 29]. Considering the special case of ν_T=1 with equal electron densities, one has the situation where each of the individual layer LLs is at ν=1/2 or is half filled with electrons. By performing a particle-hole transformation one can equivalently interpret the single layer LL as being half filled with empty states or holes. In the (111) state the optimal system configuration as given by Eq. 3.10 is one where each electron is located directly opposite to that of a empty state or hole in the other layer (Fig. 3.9). At ν_T=1 there will exist an equal number of electrons and holes, allowing electrons in one layer to bind with holes in the other layer forming electron-hole pairs (e-h) or excitons. Since e-h pairs consist of charge opposite particles they have an overall net charge of zero. Also since the electron and hole momentum vectors are equal but opposite in direction all excitons will have the same net $k = 0$ state. This fortunately does not violate the Pauli exclusion principle since both the electron and hole are both spin-1/2 fermionic particles that add to form an even spin composite boson particle. It was therefore predicted that under appropriate conditions of dilute exciton densities and low temperatures a bilayer system can undergo Bose-Einstein condensation. The e-h pairs can still condensate despite a strong magnetic field being present since they are charge neutral. This is in contrast to the condensation of Cooper pair particles where vortices would form. Also because of exciton charge neutrality, they will not feel a Lorentz force when passing through $B_\perp$, leading to zero Hall voltage!

The prediction of a BEC of excitons in semiconductor systems was raised over 40 years ago by theoreticians [1, 2]. It was predicted that excitons due to their light mass should undergo condensation at temperatures of ~ 1 K, which is approximately 10^6 higher than that of the heavier alkali atom BECs which have a typical condensation temperature of $T_c = 10^{-6}$ K. The relation between condensate temperature T_c and mass for the 3D case is given by [65]

$$T_c^{3D} = 0.527 \frac{2\pi\hbar^2}{Mk_B} \frac{n^{2/3}}{g},$$

(3.18)

where n is the density of excitons, M is the effective exciton mass, g is the spin degeneracy of the exciton state, and k_B is the Boltzman constant. Since the ground state of a pure semiconductor has no electrons or holes present, e-h pairs have been traditionally created by thermally or optically exciting electrons from the valence band into the conduction band leading to the creation of free electrons and holes that can bind to form excitons. Unfortunately, these excitons exist in a highly non-equilibrium state where the electrons and holes will quickly recombine in relatively short times of ns or μs. The time required by the excitons to cool down from their optically excitation temperatures to below the critical condensate temperature T_c is typically much longer than the recombination time, thus preventing condensation from occurring. In addition, further complications hampering condensation may arise due to the electrons and holes residing in separate bands having different dispersions relations [30].
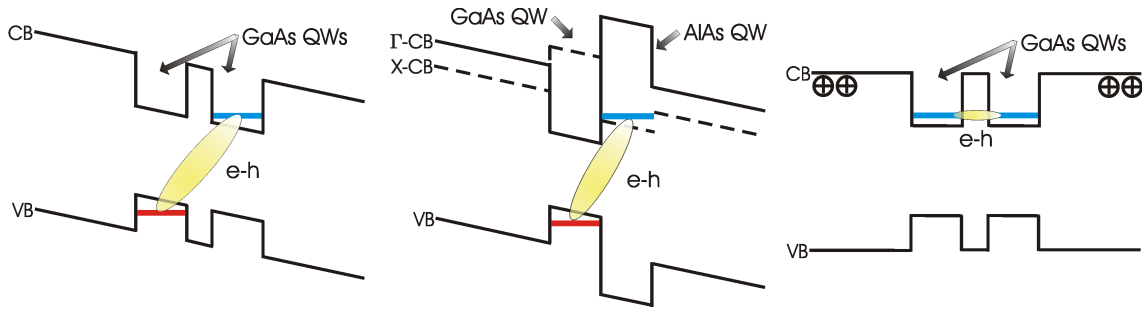
Figure 3.10: On the left is depicted a bilayer GaAs QW system where indirect *e*-*h* pairs are created by optical excitation. The spatial separation of the *e*-*h* pairs greatly reduce their wave function overlap and hence recombination probability. In addition, recombination times can be still further increased by spatial separation combined with k-space separation as shown in the middle by the GaAs/AlAs QW structure. On the right is shown a bilayer quantum Hall system where *e*-*h* pairs exist at an equilibrium in the conduction band.

A recent approach to extend the exciton lifetime by many orders of magnitude has been to use double quantum systems as schematically depicted in Fig. 3.10 to create indirect excitons. The system on the left consists of conduction electrons in one well indirectly bound with valence band holes in the other well, forming excitons. The spatial separation between the *e*-*h* pairs greatly reduces wavefunction overlap, lowering the probability of recombination. Experiments on optically generated systems have uncovered some interesting properties [66, 65, 67, 68, 69], however, conclusive evidence of exciton BEC has not been obtained so far.

Problems with short exciton lifetimes and different band dispersions in optically generated exciton systems are avoided in quantum Hall bilayer systems. At ν_T=1 excitons can exist at equilibrium in the groundstate and thus have infinite lifetimes, thus foregoing any optical excitation requirements. In addition, the *e*-*h* pair is now formed between two dispersionless Landau bands located in the QW conduction bands as depicted in Fig. 3.10, meaning that for different k-vectors the energy is completely degenerate avoiding any problems with Fermi nesting.

In the *e*-*h* picture proposed by Keldysh and Koslov [2] the phase coherence of *e*-*h* pairs in an excitonic condensate is signaled by a finite expectation value for the order parameter,

$$< c^\dagger_{c,\vec{k}}, c_{v,\vec{k}} > \tag{3.19}$$

which corresponds to the creation of an electron in the conduction band with the simultaneous annihilation of an electron in the valence band. This order parameter is closely analogous to the finite expectation value that creates a pair of electrons in a time reversed state in a superconductor. A similar interpretation can be used in the case of the bilayer QH systems. Here an effective vacuum state can be created by defining one of the wells as having a Landau level that

is completely empty and the other Landau well as being completely full. In the case where the upper layer is full and the lower layer is empty the vacuum state is

$$|filled_{upper}\rangle = \prod_k c_{upper}^\dagger |0\rangle. \tag{3.20}$$

Acting on the vacuum state with the e-h operator $c_{lower}^\dagger c_{upper}$, which will annihilate an electron (create a hole) in the filled upper layer while simultaneously creating an electron (annihilate a hole) in the empty lower layer, the ν_T=1 wave function can be expressed as

$$\Psi = \prod_k (u + v c_{lower}^\dagger c_{upper}) \prod_k c_{upper}^\dagger |0\rangle. \tag{3.21}$$

This is essentially identical to an exciton condensate in the standard conduction-valance band form of Eq. 3.19 where excitons $< c_{lower}^\dagger, c_{upper} >$ are now created by taking an electron out of the filled upper layer and placing it in the empty lower layer. The excitons can then be thought of as an electron in the lower layer bound to a hole in the upper layer. On the other hand one could also consider the lower layer as completely full and the upper layer as completely empty. This results in a completely equivalent state where the creation of excitons are $< c_{upper}^\dagger, c_{lower} >$ and the wavefunction is

$$\Psi = \prod_k (u c_{upper}^\dagger c_{lower} + v) \prod_k c_{lower}^\dagger |0\rangle. \tag{3.22}$$

Creating an exciton in Eq. 3.21 is exactly the same as annihilating an exciton in Eq. 3.22. This duality is not surprising considering the particle-hole symmetry of a half full lowest Landau level. Here it is equally valid to think of the available states as being filled with electrons or holes.

For completeness Eq. 3.21 can be multiplied through by c_{upper} reproducing Eq. 3.1. Replacing u and v by $\cos(\theta/2)$ and $\sin(\theta/2)$ respectively produces the following form

$$|\Psi\rangle = \prod_k \{\cos(\theta/2) c_{k,\uparrow}^\dagger + \sin(\theta/2) e^{i\phi} c_{k,\downarrow}^\dagger\}|0\rangle, \tag{3.23}$$

where the polar angle $\theta = 0$ corresponds to an electron completely located in the upper layer and $\theta = \pi$ is an electron in the lower layer. Similar to the pseudospin wavefunction Eq. 6.1 the azimuthal angle ϕ correspondes to the global symmetry.

Chapter 4

Samples and Processing

The fabrication of high quality electron bilayer samples is a technically challenging task. Only quite recently progress in molecular beam epitaxy (MBE) has allowed for the possibility of growing epitaxial crystal structures showing the ν_T=1 excitonic effect with a highly resistive interlayer barrier [3]. In addition to crystal growth, other technical challenges include the development of annealing techniques to electronically contact the 2DESs, the making of separate electrical contacts to the individual layers, and the fabrication of electrostatic gates to control the layer electron densities.

In the first portion of this chapter, Sec. 4.1, details of the crystal structure used to confine electrons in two closely spaced 2DES will be presented. Next in Sec. 4.2 the method used to electrically contact the individual electron layers will be discussed. Finally, the different sample designs used in this work will be explored in Sec. 4.3.

4.1 Bilayer Sample Crystal Structure

A schematic cross section of the basic structure used in this work is displayed in Fig. 4.1. Before actual MBE growth of the crystal structure simulations using a self-consistent Poisson-Schrödinger solver [70] are made to estimate the electron distribution and density profiles in the QWs as a function of various parameters as QW thickness, spacer layers, doping profiles, Al composition, etc. A calculation of the Γ-minimum conduction band energy diagram using the solver is displayed along the crystal structure in Fig. 4.1. From the calculation it is seen that QWs are formed by sandwiching a gallium arsenide (GaAs) layer between two aluminum gallium arsenide (AlGaAs) layers. The $Al_{0.33}Ga_{0.67}As$ forming one wall of the GaAs QW is calculated to have a conduction band $\sim$ 160 meV higher in energy whereas the other wall, formed using a $Al_{0.9}Ga_{0.1}As$ barrier is $\sim$ 250 meV higher. Conduction band electrons supplied from Si-doped regions will therefore become trapped in the QWs at low temperatures. Since the average intra-layer electron spacing at ν_U=1/2, ν_L=1/2 is proportional to the density $\ell_B =$
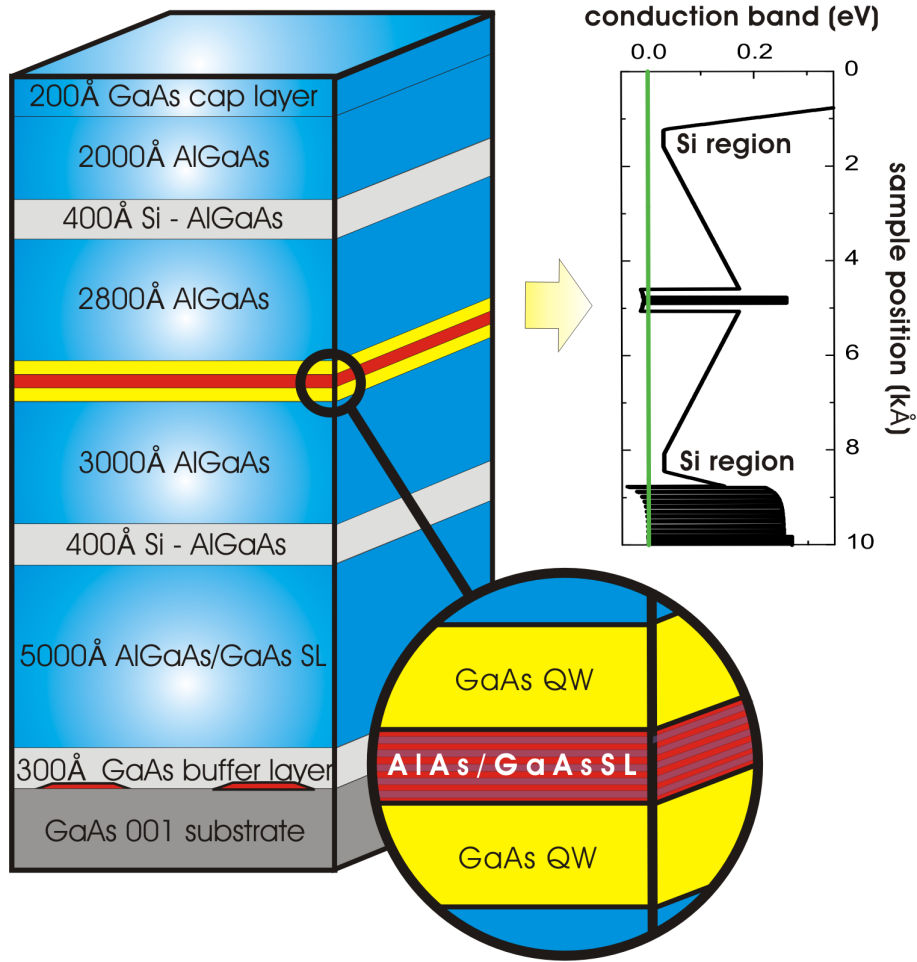
Figure 4.1: A cross sectional representation of a typical GaAs/AlGaAs semiconductor structure used in forming a bilayer QW system. The magnified area displays the active region consisting of the two GaAs QWs separated by an AlAs/GaAs superlattice. The calculated conduction band diagram, corresponding to the various crystal regions, is also shown.

$\sqrt{(4\pi n_s)^{-1}}$ whereas the center-to-center QW spacing d is an experimentally fixed quantity, it is preferable to have bilayers with low intrinsic electron densities to reach the required d/ℓ_B ratios. Therefore, with the QW electron density being inversely proportional to spacer layer thickness [71], a large separation between the QWs and the doped region is incorporated. The intrinsic electron density calculated using a Poisson solver for a spacer layer thickness of 300 nm is $\sim 4 \times 10^{10}$ cm^{-2} and agrees very well with the actual experimentally determined densities of 3.7×10^{10} - 4.5×10^{10} cm^{-2}.

All the crystal structures used in this work are grown using the MBE technique. Due to requirements of high mobility and hence low sample impurity incorporation, MBE offers a

distinct advantage over other crystal growth techniques due to the sample structure being grown in a controlled ultra high vacuum (UHV) environment. Using reflection high energy electron diffraction (RHEED) to monitor the growth surface *in situ*, MBE offers a method of precise atom layer growth control. The epitaxial layers in the bilayer structures consist of the III-V semiconductors GaAs and AlGaAs, grown using ultra pure Al, Ga, and As source material that are thermally evaporated from crucibles onto a (001) orientated SI GaAs substrate surface.

The active region in the bilayer samples consists of the two QWs separated by a high Al content barrier as seen in Fig. 4.1. In this work the samples used to obtain data are denoted in Tab. 4.1. Two different types of active regions are investigated, either two 17 nm GaAs QWs separated by a superlattice of 12.4 nm or two 19 nm GaAs QWs separated by a superlattice of 9.6 nm. It should be noted in both cases that the center-to-center QW spacing d= 29.4 nm of the 17 nm/12.4 nm/17 nm and d= 28.6 nm of the 19 nm/9.6 nm/19 nm are approximately the same. Therefore, according to the ν_T=1 excitonic state phase diagram, Fig. 3.3 these samples should show similar characteristics, however, as shown later in Sec. 6.5 this surprisingly is not the case!
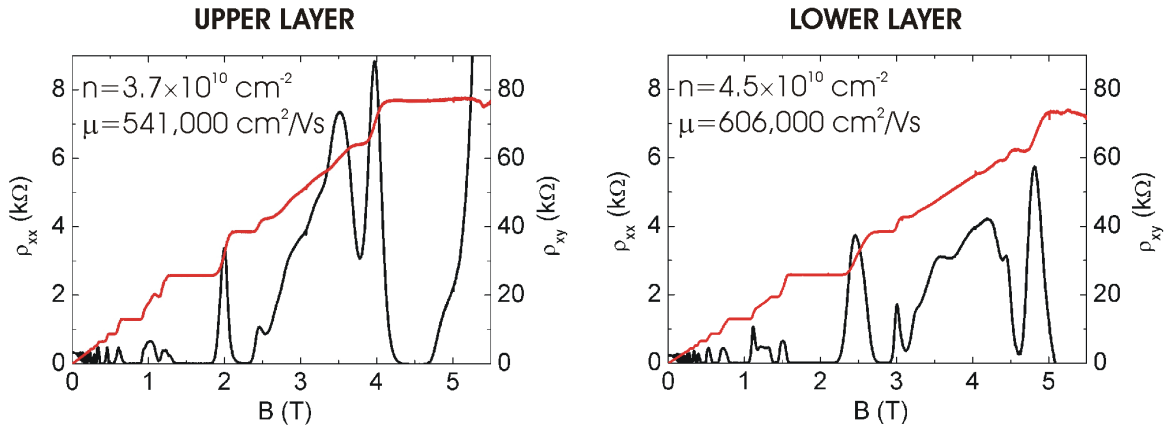

Figure 4.2: Magneto-transport data of the upper and lower layers for the 19nm/9.6nm/19nm (d041007c-143) sample. Sweeps are performed at intrinsic layer electron densities (zero tuning gate voltages) and show many FQHE features indicating high 2DES quality.

As discussed in Sec. 3.3 to observe the ν_T=1 excitonic state the interlayer tunneling between the layers must be small. For electron bilayer systems an AlAs barrier of typically > 9 nm is thus needed. Including the QW thickness ($15 - 20$ nm), the center-to-center QW spacing d is experimentally fixed around 25 - 30 nm, and therefore single layer electron densities of $\sim 3 \times 10^{10}$ cm^{-2} are required to obtain a $d/\ell_B < 2.0$ at total filling factor ν_T=1. To avoid the electrons from becoming localized before reaching the required magnetic field, high mobilities exceeding 400000 cm^2/Vs at these densities are needed. In order to obtain these high mobilities

WAFER QW/BARRIER/QW (nm/nm/nm)	UPPER DENSITY (cm^{-2})	UPPER MOBILITY (cm^2/Vs)	LOWER DENSITY (cm^{-2})	LOWER MOBILITY (cm^2/Vs)	INTERLAYER RESISTANCE ($M\Omega$)
D040114B-100 (17/12.4/17)	3.8×10^{10}	452000	4.4×10^{10}	538000	> 1000 at B $= 0$
DO41007C-143 (19/9.6/19)	3.7×10^{10}	541000	4.5×10^{10}	606000	~ 45 at B $= 0$
DO41007C-55 (19/9.6/19)	3.7×10^{10}	485000	4.5×10^{10}	510000	~ 80 at B $= 0$

Table 4.1: Wafers with their associated characteristics used in obtaining data for this work. All electron density and mobility measurements are made at temperatures below 50 mK. In all cases an upper front gate voltage of ~ -0.35 V and a lower back gate voltage of ~ -0.65 V is used for contact separation.

a large 500 nm superlattice of alternating AlGaAs (7.92 nm) and GaAs (2.26 nm) is grown before the active region to reduce interface roughness (see Fig. 4.1). In addition, the inter-layer barrier is a superlattice composed of alternating 4 monolayers of AlAs (1.13 nm) with 1 monolayer of GaAs (0.28 nm) which may further improve mobility.

The QW electrons originate from bulk doped Si regions placed 280 nm above and 300 nm below the upper and lower QWs, respectively. As seen in the Poisson-Schrödinger calculated band diagram of Fig. 4.1, the Si donors pin the conduction band near the Fermi energy leading to the GaAs QW conduction bands being pulled below the Fermi energy resulting in trapped electron populations. To compensate for surface segregation of the Si dopants during the growth process, the spacer layer below the lower QW is increased slightly. In addition, the upper Si doped region (40 nm width) is enlarged with respect to the lower doping region (35 nm width) to account for electrons taken up by surface states. The volume doping method is preferred over δ-doping since it provides easier control and reproducibility of the final carrier densities with different sample cool downs. In all cases, no illumination at low temperatures is required to obtain workable electron densities in the QWs.

4.2   Separately Contacted Quantum Wells

The 2DESs are electrically contacted by thermally evaporating 321.6 nm Au, 158.4 nm Ge, and 75.0 nm Ni on photolithographically defined regions of the mesa as shown in Fig. 4.3. By annealing the metallic contacts under a 20% H$_2$/80% N$_2$ forming gas at T=440°C the metal diffuses down into the crystal and through the QWs. This diffused metal interacts with the conduction bands profiles in the QWs in such a way as to allow electrical access to the 2DES
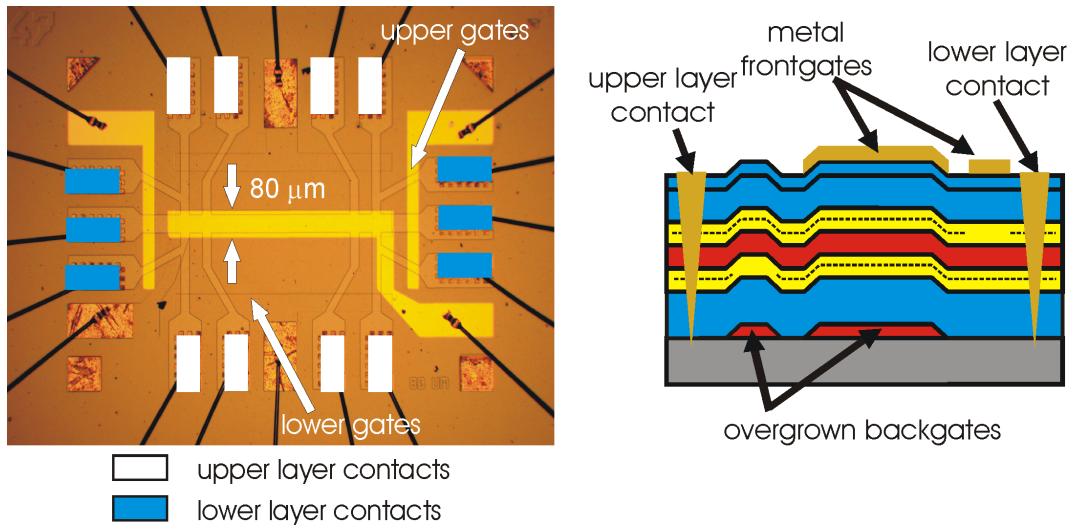
Figure 4.3: On the left is a top view of a 880 μm $\times$ 80 μm Hall bar bilayer structure used in this work. The upper layer electron density tuning gate is covering the entire Hall bar. Not visible is a buried lower layer tuning gate positioned below the Hall bar. The right shows a cross sectional view of how gates are used to selectively deplete the upper and lower layers for contact separation.

[72]. Since the samples used in this work have an active region located 540 nm below the surface, 180 - 200 nm contact holes are etched *a-priori* before metal contact evaporation to assure sufficient diffusion of contact material down to the QWs.

The annealed metal contacts will pass through both QWs and therefore the two layers will be electrically coupled to the same contact. Experimental studies on interlayer tunneling, drag measurements, and other experimental configurations needed to properly investigate the ν_T=1 state require individually contacted layers. Therefore it is necessary to uncouple the two layers. This has been achieved by using a technique first pioneered by Eisenstein et al. [8] using electric field gates located above and below the active region to selectively deplete the QWs. With reference to Fig. 4.3 a negative front gate voltage with respect to the upper 2DES will deplete all electrons in the upper layer such that all contacts behind this front gate will only make contact with the lower layer. Likewise, a negative voltage on the overgrown lower back gate will selectively deplete all electrons in the lower layer, forcing all contacts behind this gate to make contact only to the upper layer. In this way eight and six Ohmic contacts are made to the upper and lower 2DES, respectively.

For samples used in this work front gates are defined using photolithography and created by thermally depositing 150 nm Ti/Au or 150 nm Cr/Au. During the evaporation process the samples are mounted in the evaporator at a slight angle and rotated with respect to the evaporated sources as to allow metal to be also deposited over the mesa edge thus preventing an electrical

conduction break in the gate due to insufficient coverage along the mesa edge. Because of the relative near vicinity of the metallic front gates to the upper QW ($\sim$540 nm) a low front gate voltage of -0.35 V is sufficient to depleting the upper layer for all samples used in this work (see Table 4.1).

Unlike the front gates, back gate fabrication is problematic due to the lower QW being located far from the back of the substrate (> 500000 nm). Therefore, thermally evaporated metallic field gates at these distances will require gate voltages in excess of 1000 V and will consequently lead to poorly defined depletion regions due to inhomogeneity of the electric field. To avoid these large gate voltages it is desirable to locate the back field gates closer to the lower QW. This can be done by thinning the substrate to ~ 50 μm using mechanical (abrasive materials) or chemical (bromine-methonal etch) methods. For a ~ 50 μm distance voltages of $\sim$ 100 V are adequate to fully deplete the lower QW. Unfortunately the application of DC voltages > 100 V are still hazardous and the thinning process leaves the sample in a fragile state, making handling difficult. These problems are avoided in this work by using a method developed by Rubel et al. [9] using highly Si-doped GaAs overgrown back gates. This technique locates the back gates only $\sim$ 900 nm from the lower QW. In this case voltages of only $\sim$ -0.65 V are sufficient to deplete the lower QW for the samples detailed in Table 4.1. The general procedure is to first grow a 100 nm highly Si-doped n > 10^{18} cm^{-3} GaAs layer onto a semi-insulating (SI) epitaxial GaAs substrate using MBE techniques. The wafer is removed from the MBE and photolithography is used to define back gates with a positive-photoresist. A wet chemical etch is used to remove the uncovered Si-doped layer leaving the photoresist covered back gates behind. The wafer is then epi-cleaned using a procedure developed by Fronius et al. [73] to remove hydrocarbons and other contaminates from the substrate surface. Finally, the back gate patterned wafer is reinserted into the MBE for overgrowth of the remaining bilayer structure. At low temperatures the highly Si-doped GaAs material is dominated by degenerate conduction, making it metallic in nature and thus suitable as a back gate.

In addition to the front and back depletion gates, a single large metallic full front gate and a single full back gate are fabricated to cover the 80 μm $\times$ 880 μm Hall bar as shown in Fig. 4.3. By application of suitable voltages to these gates with respect to the 2DESs the electron densities in the individual layers can be independently tuned to desired values. It should be noted that the other layer is generally unaffected by the gate electric field due to the screening properties of the 2DES closest to the gate.

4.3   Sample Design and Processing

All structures used in this work are initially created using the computer assisted drawing program DW2000 from Design Workshop Technologies and all final mask designs are contracted

out to a third party company for fabrication using chromium on quartz masks. The two designs used in this work consist of a standard Hall bar (see Sec. 4.3.1) and a modified standard Hall bar to produce a DC transformer (see Sec. 4.3.2).
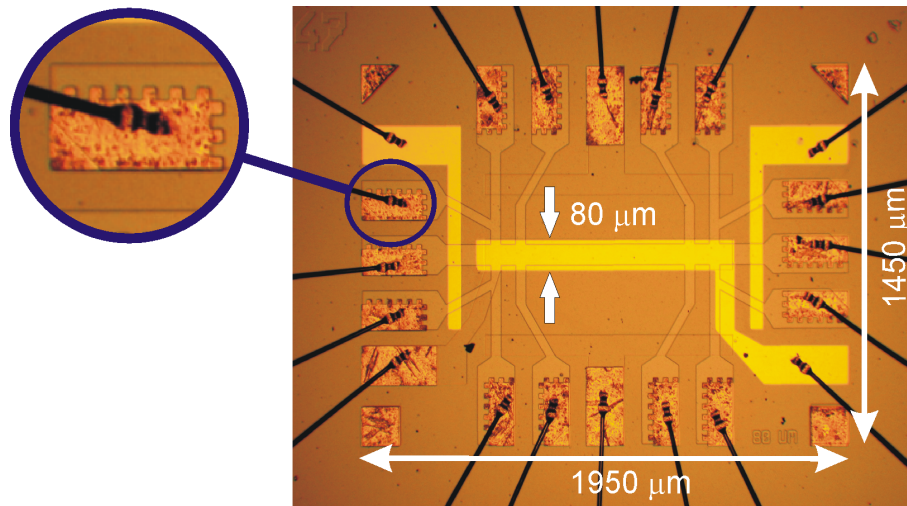
4.3.1 Standard Hall Bar

Figure 4.4: A top view of the 880 μm $\times$ 80 μm Hall bar bilayer structure used in this work. The total mesa dimensions including contact arms are 1.95 mm by 1.45 mm. Left is a magnification of a contact pad displaying the annealed interfaces along both the $[110]$ and $[1\bar{1}0]$ crystal directions.

The total foot print of the Hall bar including contact pads is 1.95 mm by 1.45 mm as shown in Fig. 4.4. The actual Hall bar is 80 μm wide and 880 μm in length. The full back gate and full front gate are slightly larger than the actual Hall bar to insure both 2DES are exposed to a homogeneous electric field.

A magnification of one of the contact arms displayed in Fig. 4.4 shows a square saw tooth pattern outlining the contact. It is found that certain orientations of the annealed metallic contact pad with respect to the semiconductor crystal direction will lead to a better conduction with the 2DES. Using a saw tooth pattern thus allows interfaces with both the $[110]$ and $[1\bar{1}0]$ crystal directions to occur.

4.3.2 DC Transformer

Two different types of DC step-up voltage transformer designs used in this work include a $2\times$ transformer and a $4\times$ transformer. Both of these transformers are modifications of the standard
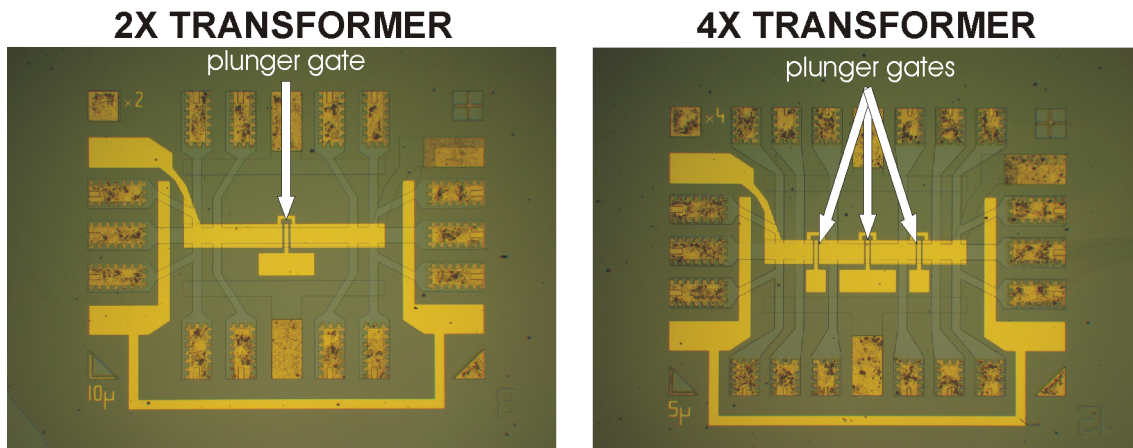
Figure 4.5: Top view of step-up voltage DC transformer structures. Two designs are made consisting of either two (right figure) of four (left figure) ν_T=1 regions as defined by indicated finger gates.

bilayer Hall bar design presented in section 4.3.1. The back gate structures used are identical to the standard Hall bar design and required no new mask fabrication. A new mask is designed for the Hall bar mesa and front gate structures. These designs are unique since the upper 2DES can be separated into two ($2\times$ trans.) or four ($4\times$ trans.) ν_T=1 regions through the use of small finger gates patterned across the Hall bar. The width of the plunger gate is 10 μm and the spacing between the plunger gate and the full front gate can be either 5 μm or 10 μm depending on the mask selected. The Hall bar dimensions are again 80 μm and 880 μm, however, as seen in Fig. 4.5 the $4\times$ transformer includes four additional contact arms to contact the four separate upper layer 2DESs.

Chapter 5

Experimental Setup

In addition to high quality bilayer samples, an investigation of the $\nu_T=1$ excitonic state requires the use of highly specialized experimental equipment. The first half of this chapter, Sec. 5.1 discusses how the experimental conditions of low temperatures (T < 200 mK) and large perpendicular magnetic fields (~ 2 T) necessary to observe the $\nu_T=1$ state are achieved. The second half, Sec. 5.2 discusses the techniques used to make low noise magneto-transport and tunneling measurements.

5.1   Cryostat + Magnet

An Oxford System 2000 low loss dewar with a 89 L ^{4}He capacity and a built-in superconducting Nb$_3$Sn magnet is used for cooling sample inserts to 4.2 K. The ^{4}He reservoir is shielded from the outside thermal environment using an outer vacuum chamber (OVC) containing many layers of aluminized mylar foil and a 68 L liquid nitrogen (LN$_2$) shield. This allows typical 4.2 K operation times of one week before liquid ^{4}He or LN$_2$ refills. The Nb$_3$Sn magnet has a guaranteed maximum central field strength of 12 T at 4.2 K. To properly explore the $\nu_T=1$ excitonic state in bilayer systems it is necessary to cool the samples to dilution refrigerator temperatures. An Oxford Kelvinox AST (Advanced Sorption Technology) ^{3}He/^{4}He dilution refrigerator is used to obtain all experimental data presented in this work. The base mixing chamber (MC) temperature as measured by the angular distribution of $\gamma-$decay of a Co^{60} source is 15 - 17 mK and the system demonstrates a cooling power of > 40 μW at 100 mK. The Kelvinox AST is unique from conventional dilution systems in respect that the external still pump is replaced by two internal graphite sorb pumps. As detailed in Fig. 5.1, one sorb will pump on the still while the other sorb is resistively heated to approximately 50 K releasing the absorbed mixture which is then condensed in the 1.6 K collector. Over time the pumping efficiency of the sorb pumping on the still will degrade due to absorbed mixture, therefore approximately every 30 min. a pneumatically actuated value will close this sorb and open the other regenerated sorb. By cycling
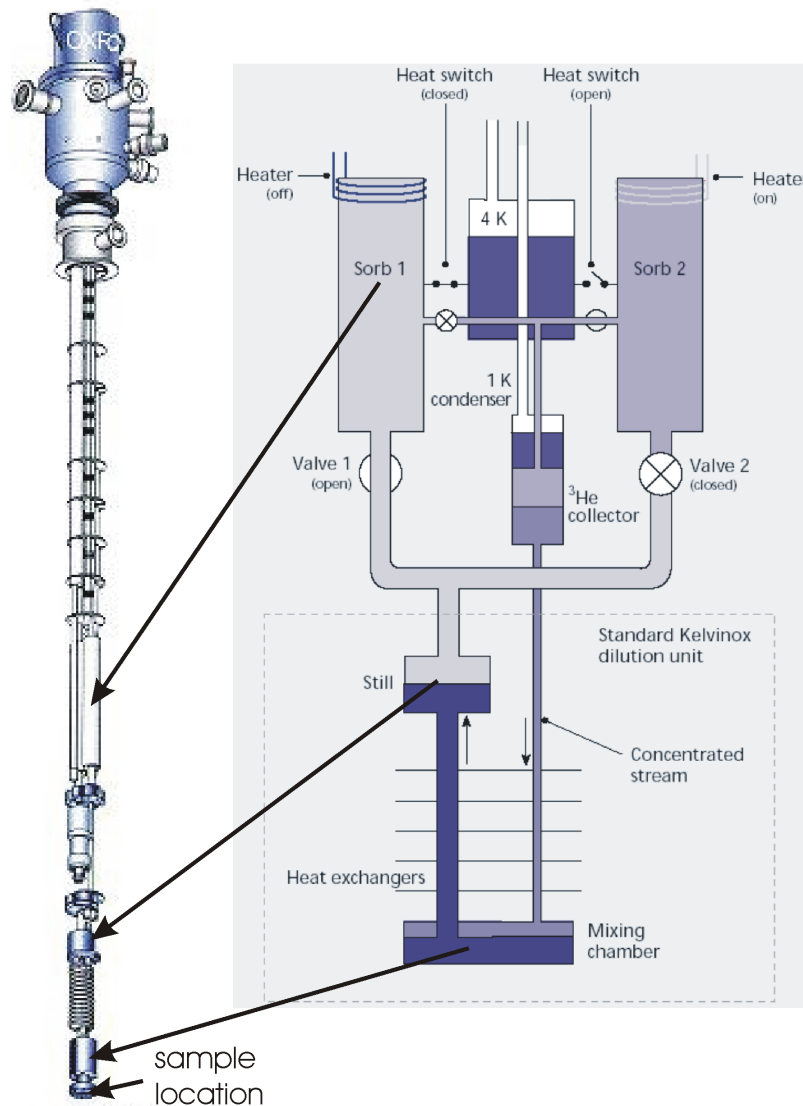
Figure 5.1: Left is displayed an outside view of a Kelvinox AST dilution system. The sample holder (not shown) is attached to the bottom of the mixing chamber. A schematic diagram showing the basic AST operation principle is displayed on the right. The typical external still pump is replaced by two internal graphite sorb pumps as indicated. Figures courtesy of Oxford Instruments.

between pumps a continuous pumping on the still can be maintained. The all internal configuration of the AST is advantageous due to the lack of mechanical vibration and contamination of the ^{3}He/^{4}He mixture inherent with external pumped systems. Disadvantages, however, include a non-constant pumping power on the still due to the decaying pumping efficiency of the sorb with time. This leads to a slight 2 - 3 mK periodic warming and cooling of the mixing chamber with each pumping cycle.

A custom built sample holder is mounted at the end of the copper mixing chamber. The temperature of the sample is measured directly with a RuO_2 resister mounted on the sample holder near the chip carrier. The RuO_2 resister is calibrated as a function of MC temperature as shown in Fig. 5.2. On a log plot the RuO_2 resistance scales linearly with MC temperature for temperatures above 30 mK, demonstrating that the MC and the sample holder are approximately at the same temperature. Therefore, for T_{MC} > 30 mK a measurement of the MC temperature can be considered to be the same as the sample holder temperature. Below 30 mK the RuO_2 resistance deviates from the linear and eventually saturates to a constant resistance of 180 kΩ. This saturated value corresponds to the sample holder base temperature of $\sim$ 25 mK. Hence, between T_{MC}= 15 - 30 mK the temperature difference between the warmer sample holder and cooler MC must be considered. This thermal difference is most likely a result of blackbody radiation from the top of the insert cavity and non-ideal thermal anchoring of the sample holder to the MC.
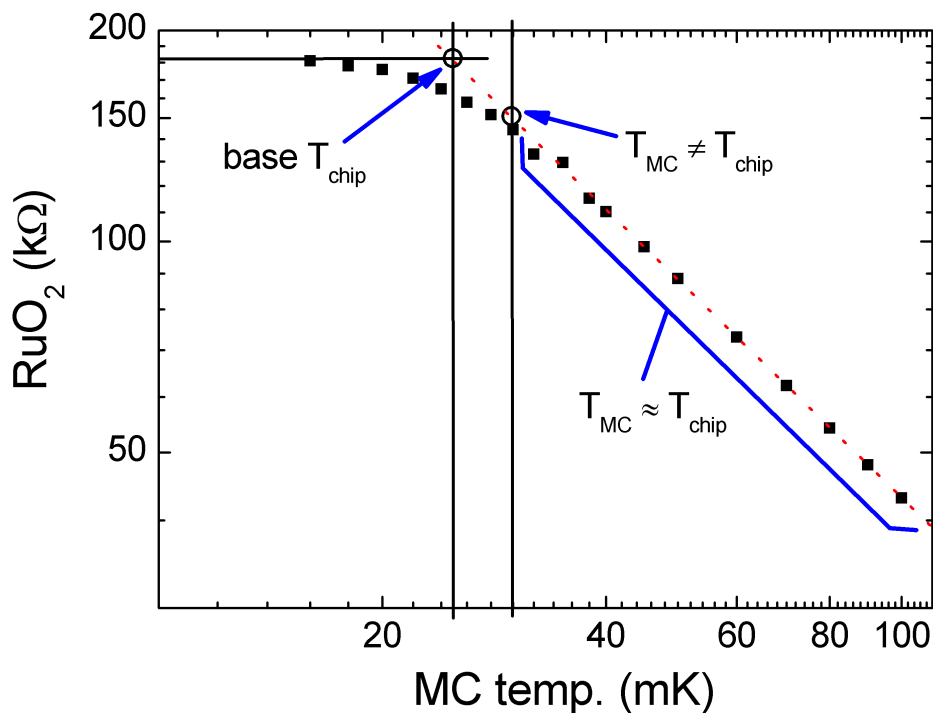

Figure 5.2: Log scale plot of resistance vs. MC temperature as measured by a RuO_2 resistor attached to the sample holder. Resistance scales linearly with MC temperature for temperatures above $\sim$ 30 mK, below which the resistance quickly saturates to $\sim$ 25 mK.

The actual GaAs/AlGaAs sample is mounted in a ceramic package and electrically bonded

using 20 Au wires of 25 μm diameter to the package contact pads. This is mounted in a socket holder with spring loaded copper blades that make a pressure contact to the package pads. The actual semiconductor sample is therefore primarily cooled through the 20 Au wires which are thermally anchored to the MC. Although the GaAs/AlGaAs crystal temperature is most likely near the sample holder measured RuO_2 temperature, the actual electronic temperature of the 2DES, T_{2DES}, usually saturates at a much higher value of ~ 60 mK if special precautions are not taken. High frequency electromagnetic (EM) radiation in the form of radio, microwave or thermal radiation can be transported from the outside via electrical cables that run down to the sample [74]. To reduce this EM noise Pi-filters are used on all AST system control cables and a custom 24-line Pi-filter box is used at the sample entrance port of the insert.
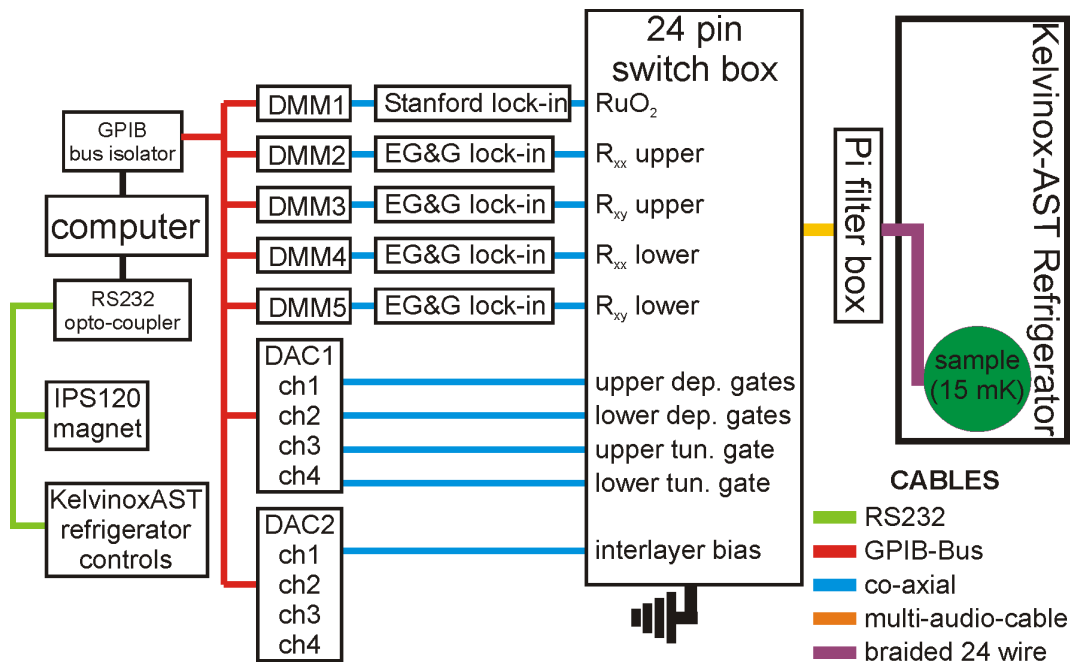
5.2   Measurement Techniques

Figure 5.3:   Schematic block diagram of experimental setup used for obtaining magneto-transport data. Colors denote different cables used (see legend). A singely defined system ground connected to the switch box is used. Not shown is the Oxford System 2000 ^{4}He with a built-in 14 T superconducting Nb_3Sn magnet.

Since all gate potentials used for selective depletion and tuning of the 2DES densities are with respect to a system ground, small fluctuations of this system ground will lead to density instabilities in the sample. Therefore, great precaution is taken to make sure that there exists

only one singly defined system ground. As shown in the schematic setup diagram of Fig. 5.3 a 24-BNC connector breakout box acts as the singly defined ground source for the system through a single cable connected to earth. Great care is taken to avoid any additional inadvertent ground connections through cables, pumping lines, or other instruments which could lead to the formation of grounding loops. The sample, dilution insert (Kelvinox AST), and cryostat (Oxford System 2000) are all grounded to the breakout box through the shielding of the cable housing the sample wires. This cable consists of a large copper wire braided outside shield housing 24 shielded twisted pairs of wires that are connected to the sample. Isolation transformers are used on all electrical equipment connected to the breakout box to prevent grounding loops.

All instrument control and data gathering is accomplished over serial RS232 or GPIB bus using a single computer (see Fig. 5.3). The computer is isolated from the experimental system by the use of opto-couplers on all data lines to prevent any high frequency electrical noise from reaching the experiment.

Gate voltages and experimental DC voltages are provided by custom built digital-to-analog converters (DAC) with a voltage output range of ± 10 V and with GPIB bus control. All longitudinal (V_{xx}) and Hall (V_{xy}) voltage measurements are made using a standard four point configuration with EG&G Princeton 5210 or Stanford SR830 lock-in amplifiers. An AC current typically between 0.2 - 1 nA is used for magneto-transport measurements of the ν_T=1 excitonic state. Sample currents are defined by a sinusoidal low frequency AC voltage provided by a lock-in or a Stanford DS345 function generator that is current regulated by insertion of a large resistance (10 MΩ or 100 MΩ). To avoid computer generated noise the lock-in outputs are not connected directly to the GPIB bus, but rather have all outputs going into Keithley 2000 digital multimeters (DMM) which are then subsequently connected to the GPIB bus (Fig. 5.3). The lock-in reference signals are passed through opto-couplers to avoid any ground loops.

5.2.1 Magneto-Transport Setup

The numerous upper and lower layer contacts of the Hall bar design allow for many different current configurations to be explored as shown in Fig. 5.4 and Fig. 5.5. Three different current configurations are investigated in this work and are denoted as parallel, drag, and counter-flow. In the parallel current configuration two currents, not necessary being equal in magnitude, are passed simultaneously through both of the layers in the same direction. This differs from the drag configuration, where only a single current is passed through one of the layers ("drive layer") and the induced voltage drop in the other ("drag layer") layer is measured. Here the longitudinal and Hall resistivity components of the drag layer are defined as $\rho_{drag,xx} = V_{drag,xx}/I_{drive}$ and $\rho_{drag,xy} = V_{drag,xy}/I_{drive}$, respectively. Finally, the counter-flow current configuration consists of two oppositely directed currents through the two layers. In all cases, the magneto-transport currents $I_{applied}$ have been defined by a low frequency AC sinu-
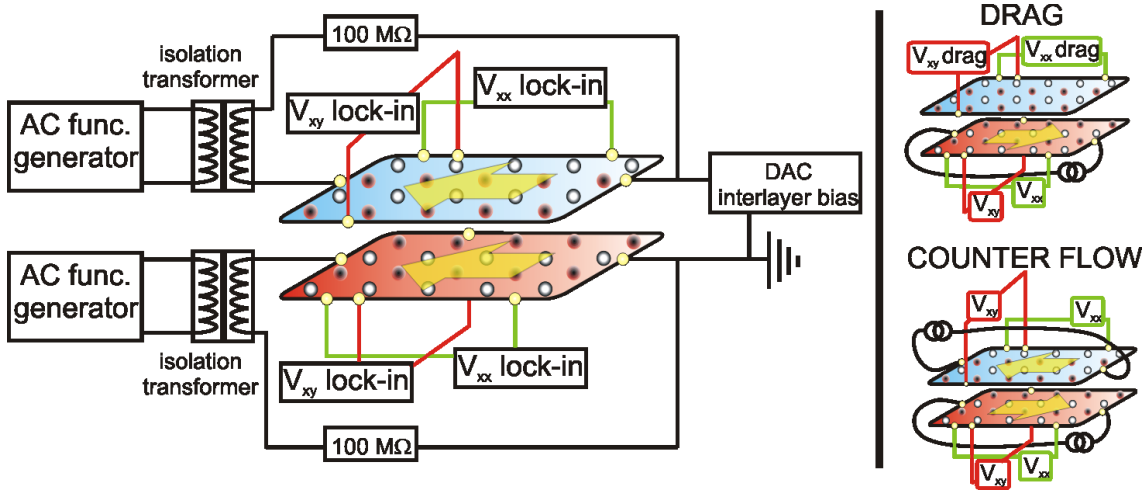
Figure 5.4: Magneto-transport setup for the parallel (main diagram), drag, and counter-flow configurations. Two phase locked current sources connected to isolation transformers are used. An interlayer bias applied using a DAC is used to imbalance the layer electron densities.

soidal voltage provided by a lock-in or function generator with the insertion of a large resistance R where $I_{applied} = V_{ac}/R$.

Normally, a single layer current flows directly from the current source through the layer to a ground contact, however, through the use of an 1:1 isolation transformer the defined ground can be removed as shown in Fig. 5.4. This allows for the possibility of still applying a current, due to the potential difference provided by the transformer, while changing the potential with respect to system ground using an external voltage source connected to one of the layer contacts. Hence, an interlayer bias voltage can be applied even in the counter-flow case. This is highly desirable since an interlayer bias between the two layers will symmetrically imbalance the electron densities $\Delta n = (n_{upper} - n_{lower})/n_T$ between the two layers, where the total system electron density (n_T) is fixed. It is thus possible to tune both individual layer densities using only one full gate and an applied interlayer bias.

5.2.2   Tunneling Setup

In Fig. 5.5 a schematic sketch of the experimental configuration used to measure interlayer resistance is shown. Here a DAC DC voltage and a small AC excitation voltage from a Stanford DS345 function generator are added using a custom built voltage adder. The output voltage is then passed through a voltage divider and connected via the switch box to one of the layers. The other layer is connected through an Ithaco I/V current preamplifier to ground. A DMM connected directly to the preamplifier output measures the DC tunneling current, however, at
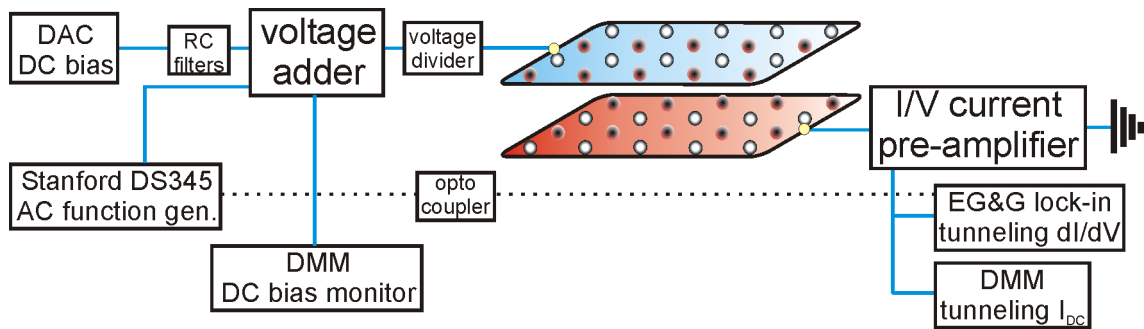
Figure 5.5: Schematic diagram of setup used to obtain differential conductivity (dI/dV) vs. interlayer bias data. A small excitation voltage supplied by a function generator is amplified and detected using lock-in techniques allowing determination of dI/dV. A DMM connected to the output of the I/V current preamplifier provides DC current data.

high interlayer impedances this is very noisy. A more sensitive measurement can be obtained from the differential conductivity (dI/dV) of the excitation voltage as monitored with a lock-in. In this way very accurate measurements of the conductivity as a function of DC voltage bias can be obtained.

Chapter 6

The ν_T=1 State at Balanced Electron Layer Densities

In the most simplistic case the ν_T=1 state is considered for balanced layer electron densities, where both layers are at filling factor ν=1/2. In the case when the intralayer Coulomb correlation energy $E_C = \frac{e^2}{4\pi\epsilon\ell_B}$ is much larger than the interlayer Coulomb correlation $E_d = \frac{e^2}{4\pi\epsilon d}$ one has the situation of two independent layers in the compressible state of ν=1/2. Dependent on sample quality the ν=1/2 state could consist of a single particle IQHE with the lowest Landau level half filled with electrons, or in the case of higher sample quality, as a composite fermions FQHE state with an effective magnetic field of zero (see Sec. 2.2.4). As the intra- and inter-layer correlation energies become similar in strength the two layers couple forming the ν_T=1 excitonic state. This chapter investigates the properties of the ν_T=1 state for balanced layers densities. Initially in Sec. 6.1 the interlayer tunneling is investigated, and then later in Sec. 6.2 and Sec. 6.3 the magneto-transport is examined. In Sec. 6.4 the Hall voltage of the ν_T=1 state is investigated as a function of different layer current imbalances. Finally, from measurements of the temperature dependence of the magneto-transport data of the ν_T=1 state, activation energies $\Delta_{\nu=1}$ are obtained as presented in Sec. 6.5.

6.1   Interlayer Tunneling

Using selective area field gate depletion techniques as detailed in Sec. 4.2 independent contact to the individual layers can be realized. It is therefore possible to make interlayer tunneling conductance experiments between the two closely spaced layers. As explained in Sec. 5.2 the tunneling setup used in this work consists of adding a small AC excitation voltage of 2 - 10 μV to a DC interlayer voltage and applying it to a contact of one of the separated layers. The other layer is connected through a I/V current preamplifier to ground, allowing measurements of the direct DC conductivity and AC differential conductivity (dI/dV) where lock-in techniques are
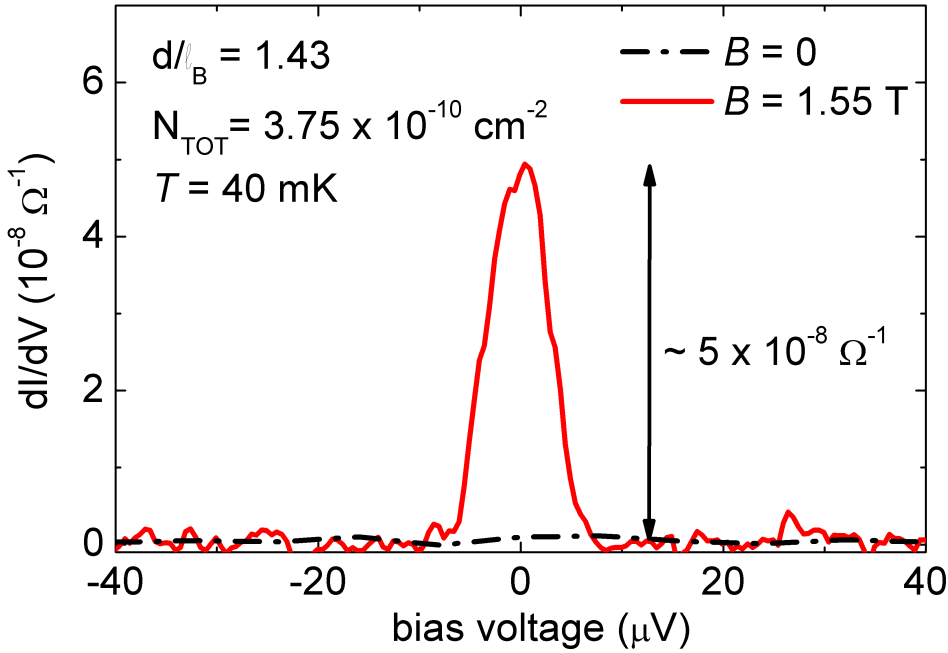
used to detect the small AC modulation.

Figure 6.1: Tunneling conductance dI/dV vs. interlayer voltage between the layers of a independently contacted bilayer electron system with a total electron density of 3.75×10^{10} cm^{-2} equally distributed between the layers. The slash-dot curve plots the $B = 0$ conductance and the solid curve denotes the ν_T=1 exciton condensate conductance at $d/\ell_B \sim 1.43$.

In the case of large d/ℓ_B, the system behaves as two independent single layers where each electron has a unitary probability of existing only in the $|upper\rangle$ or the $|lower\rangle$ eigenstate. Tunneling experiments done at B= 0 for equal layer electron densities will show a very small differential conductivity, dI/dV or very large interlayer resistance for samples having well separated layers. As shown in Fig. 6.1 the black dash-dot curve displays the B= 0 dI/dV data as a function of different DC interlayer voltages for the 17/12.4/17 (d040114B-100) sample (see Tab. 4.1). Here the calculated interlayer sample resistance is found to be several GΩ at B= 0 T.

With samples having lower interlayer resistance it is possible to detect a peak in the dI/dV vs. interlayer bias voltage at B= 0 as reported by Spielman et al. [3] for a sample with ~ 60 MΩ interlayer resistance. This increase in dI/dV corresponds to resonant tunneling effects and can be understood in terms of single particle phenomena where electrons tunnel from one layer to the other layer when the conditions of momentum and energy are satisfied [75]. With balanced layer electron densities this peak will be centered at V= 0 due to conservation of energy and momentum. With slight electron density imbalances the resonance will shift away from center

and reappear at the interlayer voltage required to create equal electron densities. It has been found that the width of the resonance tunneling peak is a reflection of the static disorder in the system [75].

Upon application of a perpendicular magnetic field, $B_\perp$ the electron kinetic energy is quenched and the single layer electrons exist in a highly correlated state. The tunneling of electrons into this correlated state is heavily suppressed since there exists no low energy states on the rapid scale of the tunneling event, placing the quickly tunneled particle into an initial highly excited state. Even at filling factors where the system is thermodynamically compressible, the time required for this excited state to relax is so large in comparison to the time scale of the actual tunneling process that the system seems incompressible. This leads to a high energetic penalty and suppression of the V= 0 resonance tunneling peak formally seen at B= 0 for equal layer densities [76, 77, 78, 79]. To tunnel an electron it is therefore necessary to overcome the intralayer Coulomb correlation energy $E_C = \frac{e^2}{4\pi\epsilon\ell_B}$. The resonance tunneling peaks therefore shift away from V= 0 to a finite interlayer voltage as shown in Fig. 3.7 by Spielman et al. [3] for a square 250 μm $\times$ 250 μm sample with 18 nm QWs separated by a 9.9 nm barrier. Here the finite interlayer voltage relates to the energy $E = eV$ necessary to tunnel an electron into the other layer. Also shown in Fig. 3.7 is the shifting of the resonance tunneling peaks towards V= 0 with lower layer electron densities indicating less energy is required to tunnel electrons since the intralayer correlation energy E_C decreases with density [3].

The $17/12.4/17$ (d040114B-100) sample used to investigate interlayer conductivity in this work however shows no detectable resonant tunneling peak features at zero or finite magnetic field values in the dI/dV vs. interlayer voltage measurements within the noise level (0.5×10^{-9} Ω^{-1}). This most likely relates to the thicker 12.4 nm AlAs/GaAs superlattice barrier, which displays an interlayer resistance of several GΩ. Nevertheless, as one moves to lower balanced layer densities and at a magnetic field such that the lowest Landau level in each QW is half filled, the ν_T=1 state is induced and a large zero interlayer voltage tunneling peak appears as shown in Fig. 6.1. This peak appears below a certain critical d/ℓ_B and increases in magnitude with lower d/ℓ_B ratios corroborating similar results as reported by Spielman et al. [3]. As discussed in Sec. 3.3, the emergence of this zero bias tunneling peak at ν_T=1 was predicted early on by theoreticians [27, 58, 59] and has been claimed as a signature of the ground state of a Bose condensate of phase coherent interlayer excitons. In this ν_T=1 state the individual layers become coupled where each electron is aware of the position of the other electrons not only within its own layer but also within the other layer. Here the strong interlayer correlation leads to the condition where a tunneled electron is opposite to an empty state in the other layer and is thus fully correlated in advance. Therefore, zero energy is required to tunnel an electron between the layers leading to the formation of a large zero bias conductance peak.

From the tunneling peak at the lowest d/ℓ_B= 1.43 obtainable before the layers becoming
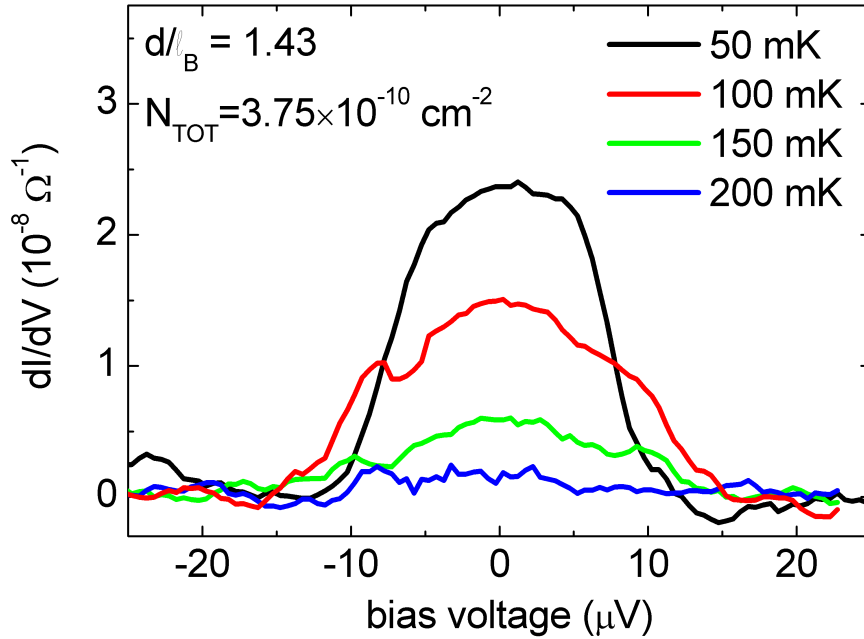
Figure 6.2: Tunneling conductance dI/dV vs. interlayer voltage between the layers of a bilayer system at d/ℓ_B= 1.43 for several different temperatures. The total electron density is 3.75×10^{10} cm^{-2} and is equally distributed between the layers.

insulating due to low electron densities we observe a conductance dI/dV of $\sim 5 \times 10^{-8}$ Ω^{-1} with a width of ~ 6.5 μV. Compared to previous experiments by Spielman et al. on samples with a similar area (250 μm $\times$ 250 μm), temperature (T= 40 mK) and d/ℓ_B ratio, we notice that our tunneling is at least one order of magnitude lower [3]. This goes against intuition, where it is expected if the ν_T=1 state is dependent only on the d/ℓ_B ratio, both experiments should display similar tunneling peak magnitudes when the tunneling surface area is approximately the same. This difference may be due the larger interlayer barrier or the narrower QWs which displayed lower electron mobilities for our sample. It has been proposed by MacDonald [80] that the interlayer tunneling is proportional to the length of the sample edges in the ν_T=1 excitonic state. This theory offers even less support to the observed differences in the conductance peak magnitudes since our sample edge length is $\sim 48\%$ larger than Spielman et al. due to our Hall bar geometry, whereas our sample area is only $\sim 11\%$ greater.

As previously reported [3], the tunneling peak height is strongly temperature dependent and falls rapidly with increasing temperature as displayed in Fig. 6.2. Compared to the previous tunneling peak of Fig. 6.1, the low temperature (50 mK) FWHM is now larger due to a greater AC excitation voltage of 10 μV being used over the previous 4 μV. This leads to a smearing out

of the zero bias peak since the V=0 point is crossed in the 10 μV AC modulation case for all DC interlayer voltage in the range $V_{DC} < | \pm 5|$. Nevertheless, the main qualitative features of the decreasing peak magnitude with increasing temperature can be seen, where for T > 200 mK the tunneling peak is completely destroyed and the sample reverts back to the typical interlayer conductivity between two independent 2DES.

Although suggestive of a Josephson effect, present experimental data do not exhibit the infinitely large and narrow zero bias conductance characteristic of a true DC Josephson effect as seen between two superconductors. While vastly enhanced, the zero bias peak remains finite and the FWHM attains a minimum but nonzero value as T$\rightarrow$ 0. It is not known if the finite height and width are intrinsic to the ν_T=1 state or rather an artifact of imperfect sample conditions. The height and width of the zero bias conductance peak are adversely affected by extrinsic electromagnetic interference, leading to a lowering and broadening of the peak. Also the limitation of cooling power due to electron heating may be another limiting source. Finally, since the tunneling method is two terminal, finite series resistances of the cables and contacts will ultimately limit the height of the tunnel peak. Recent experimental improvements have allowed the zero bias peak at d/ℓ_B= 1.50 to be measured with a dI/dV peak conductance of 20$\times$10^{-6} Ω^{-1} with a FWHM value of 2 μeV at T= 25 mK [81].

These non-ideal characteristics of the zero bias tunneling feature have lead to the formation of two groups of thought. One view supports the enhanced conductance being a type of DC Josephson effect, but with a height and width limited by complicated disorder-induced fluctuations [82, 60, 61]. The other group states there exists no exact analogue to the Josephson effect since the bilayer system is a single superfluid, not a set of two superfluid systems [83], and that within a single superfluid it is impossible to induce a chemical potential gradient between the two layers without destroying the interlayer phase coherence.

6.2 Drag Measurements

As discussed in Sec. 5.2 and shown in Fig. 6.3, drag experiments consists of passing a current through one of the layers ("drive layer") and measuring the induced voltage drop in the other electrically isolated layer ("drag layer"). This configuration is found to be a sensitive probe of interlayer electron-electron Coulomb interactions since the longitudinal drag voltage is a direct measurement of the interlayer momentum relaxation rate [84, 85] [1]. Since the drag layer is electrically isolated from the current carrying drive layer, any current flow within the drag layer will quickly lead to charge build up. This will have the effect of countering the current leading quickly to a static equilibrium. With no or zero flow of charged particles in the drag layer, a

---

[1]Though B= 0 and other non-ν_T=1 drag experiments contain rich and interesting physics it is beyond the scope of this work and the reader is referred to other works [84, 86, 87, 85, 88].
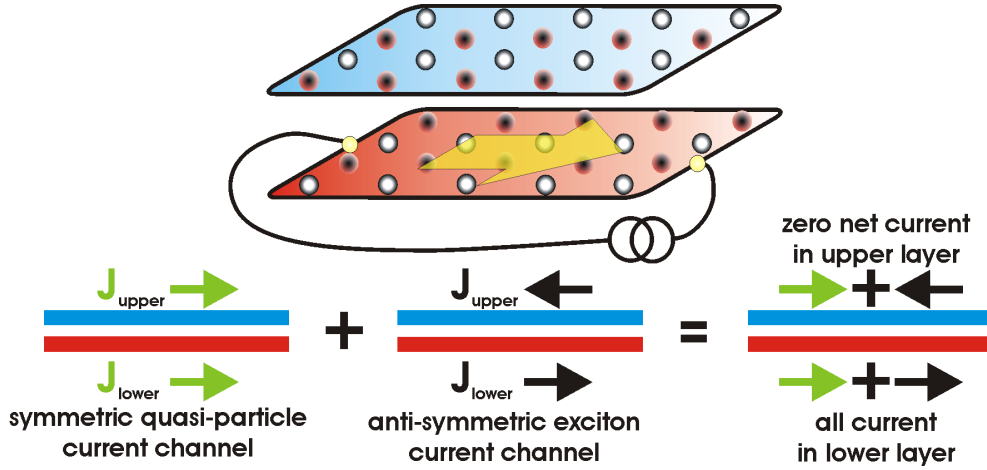
Figure 6.3: Upper is displayed the drag current configuration where current is sent only through one layer. Lower: how the ν_T=1 drag effect is a linear combination of both the symmetric charged quasi-particle and the anti-symmetric charge neutral exciton channels.

$B_\perp$ will not lead to a Lorentz force and the measured Hall drag voltage will be zero. Most surprisingly this is not the case for the ν_T=1 excitonic state!

An enlightening way of viewing the drag configuration for the ν_T=1 excitonic state has been presented by Girvin [14]. In the ν_T=1 state each electron sees a vortex, or node, in the many body wavefunction at the position of every other electron irrespective of the layer degree of freedom as discussed in Sec. 3.3. The many body wavefunction is

$$\Psi = \prod_{i<j} (z_i - z_j)\, e^{-\frac{1}{4\ell_B^2}\sum_i |z_i|^2} \otimes | \rightarrow\rightarrow\rightarrow \ldots \rightarrow\rangle \quad \text{where} \quad | \rightarrow\rangle = u| \uparrow\rangle + e^{i\phi}v| \downarrow\rangle, \quad (6.1)$$

where the first part containing the Jastrow and Gaussian terms is antisymmetric and the part contaning the spins is all symmetric. Here the two eigenstates $|upper\rangle$ and $|lower\rangle$ have been rewritten in spin-1/2 language using pseudospin up ($| \uparrow\rangle$) to denote an electron in the upper layer and pseudospin down ($| \downarrow\rangle$) to denote an electron in the lower layer [26]. The two eigenvalues (u, v) relate to the probability of finding an electron in the $| \uparrow\rangle$ or $| \downarrow\rangle$ state respectively, and have a combined probability of $|u|^2 + |v|^2 = 1$. Therefore, according to Eq. 6.1, one vortex will pass through the layers for each electron that passes through the device. Since the current is related to the number of electrons passing through the system, the total vortex flux can be written as

$$\dot{n}_{vortex} = \frac{I}{e}. \quad (6.2)$$

Using the Josephson relation $\hbar\dot{\phi} = eV$ where the Cooper pair charge of $2e$ is replaced by a single electron charge of e, and assuming each vortex drifting across the sample will cause a

slip of the global phase ϕ by 2π one obtains the rate of phase change as

$$\dot{\phi} = 2\pi \dot{n}_{vortex}. \tag{6.3}$$

Substituting this into the Josephson relation leads to a Hall voltage of,

$$V = \frac{\hbar}{e}\dot{\phi} = \frac{\hbar}{e}2\pi\dot{n}_{vortex} = \frac{\hbar}{e^2}I. \tag{6.4}$$

This quantized drag resistance was predicted earlier by theoreticians [89, 11, 12, 90] and later beautifully verified by experiments from M. Kellogg et al. [4]. Indeed as shown in Fig. 6.4 for the 17/12.4/17 (d040114b-100) sample, the drive and drag Hall resistivities are both quantized at $\rho_{xy} = h/e^2$ irrespective of the layer measured!
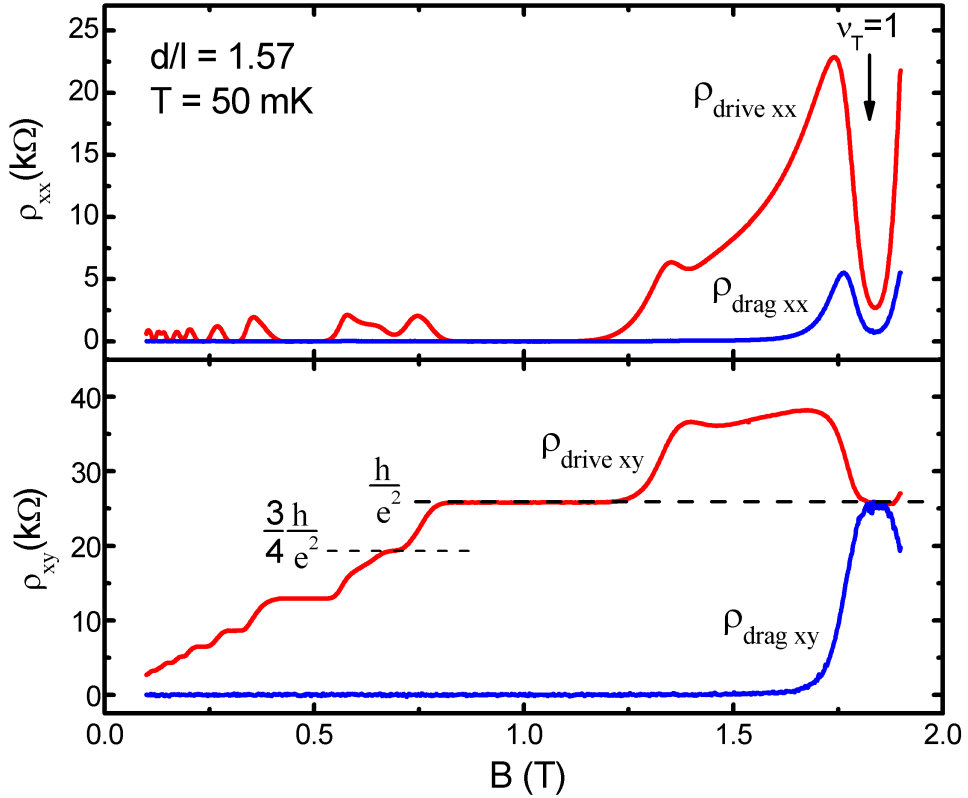

Figure 6.4: Magneto-transport measurements of the drag configuration plotting both longitudinal ($\rho_{drive,xx}$ and $\rho_{drag,xx}$) and transverse ($\rho_{drive,xy}$ and $\rho_{drag,xy}$) resistivity components vs. magnetic field at 50 mK and matched densities ($n_U = n_L = 2.22 \times 10^{14}$ m^{-2} corresponding to $d/\ell_B = 1.57$). At $\nu_T = 1$ both longitudinal components tend to zero while both Hall components tend to h/e^2.

In this experiment, transport measurements were conducted using AC currents of 0.1 - 0.5 nA at 1.2 - 6 Hz to measure the longitudinal and Hall resistances as well as longitudinal

and Hall drag voltages. Currents are defined by a sinusoidal low frequency AC voltage provided by a lock-in or a Stanford DS345 function generator that is regulated by insertion of 100 MΩ resistor. The linearity of the measurements was tested under all measurement conditions and no significant deviations were found up to ~ 1.0 nA.

Data taken with a density of 2.22×10^{10} cm^{-2} in each layer are shown in Fig. 6.4 where the longitudinal ($\rho_{drive,xx}$, $\rho_{drag,xx}$) and transverse ($\rho_{drive,xy}$, $\rho_{drag,xy}$) components of the drive and drag layers are plotted as a function of magnetic field. The upper part of the figure consists of longitudinal data away from ν_T=1, where $\rho_{drive,xx}$ shows the typical Shubnikov-de Haas oscillations of a single layer and $\rho_{drag,xx}$ is seen to be essentially zero within the sensitivity of the experimental measurement. Although small resistance fluctuation in $\rho_{drag,xx}$ due to interlayer Coulomb interactions are noticed, they are dwarfed by the features in the vicinity of the ν_T=1 state. Here $\rho_{drive,xx}$ shows a pronounced minimum while the drag increases by orders of magnitude, showing that interlayer correlations have become very large. As the d/ℓ_B is lowered it is found that both the $\rho_{drive,xx}$ and $\rho_{drag,xx}$ minima deepen, tending toward zero. In this case the formation of the ν_T=1 quantum Hall state has created an energy gap leading to the suppression of inelastic interlayer Coulomb scattering events in the drag layer leading to the small observed longitudinal drag voltage at low temperatures. The sign of the drag voltage $V_{drag,xx}$ is opposite in direction to $V_{drive,xx}$ in the current carrying layer. This sign difference has been removed from Fig. 6.4 and Fig. 6.5 for clarity purposes and is a reflection of the force balancing resulting from the constraint that no current is allowed to flow in the drag layer [4] and is commonly seen in drag studies of weakly correlated bilayer electron systems [84, 87].

The lower part of Fig. 6.4 plots Hall resistivities of the drive $\rho_{drive,xy}$ and drag $\rho_{drag,xy}$ layers. Away from ν_T=1 the $\rho_{drive,xy}$ shows the expected step-like resistance features of single layer QH behavior, and the zero drag Hall signal $\rho_{drag,xy}$ consistent with the current only flowing through the drive layer. Upon entering in the vicinity of the ν_T=1 state the transverse component $\rho_{drive,xy}$ surprisingly drops down from the expected $\sim 2h/e^2$ to a quantization plateau of h/e^2. More surprisingly still is the sudden massive increase of the essentially zero Hall drag $\rho_{drag,xy}$ to a quantized value of h/e^2! Although some energy dependent scattering processes can lead to a Hall drag signal [91, 92], such signals are very small and not detectable at the sensitivities used for the measurements. Rather this phenomena is claimed by theory to be an indirect signature of the exciton condensate [10, 11, 12, 13] and was first observed by Kellogg et al. [4] where $\rho_{drag,xy}$ was found to be precisely quantized to h/e^2= 25,813 Ω to within about five parts in 10^4. Unlike the longitudinal voltage $V_{drag,xx}$, the transverse voltage $V_{drag,xy}$ is not opposite in direction to $V_{drive,xx}$ and is claimed to be a reflection of the symmetric charged quasi-particle current in of the ν_T=1 state as sketched in Fig. 6.3. These observations are also obtained when the roles of the drive and drag layers are reversed. Increasing the temperature to above > 200 mK results in the features of the ν_T=1 state to disappear and the layers to once more show the expected single
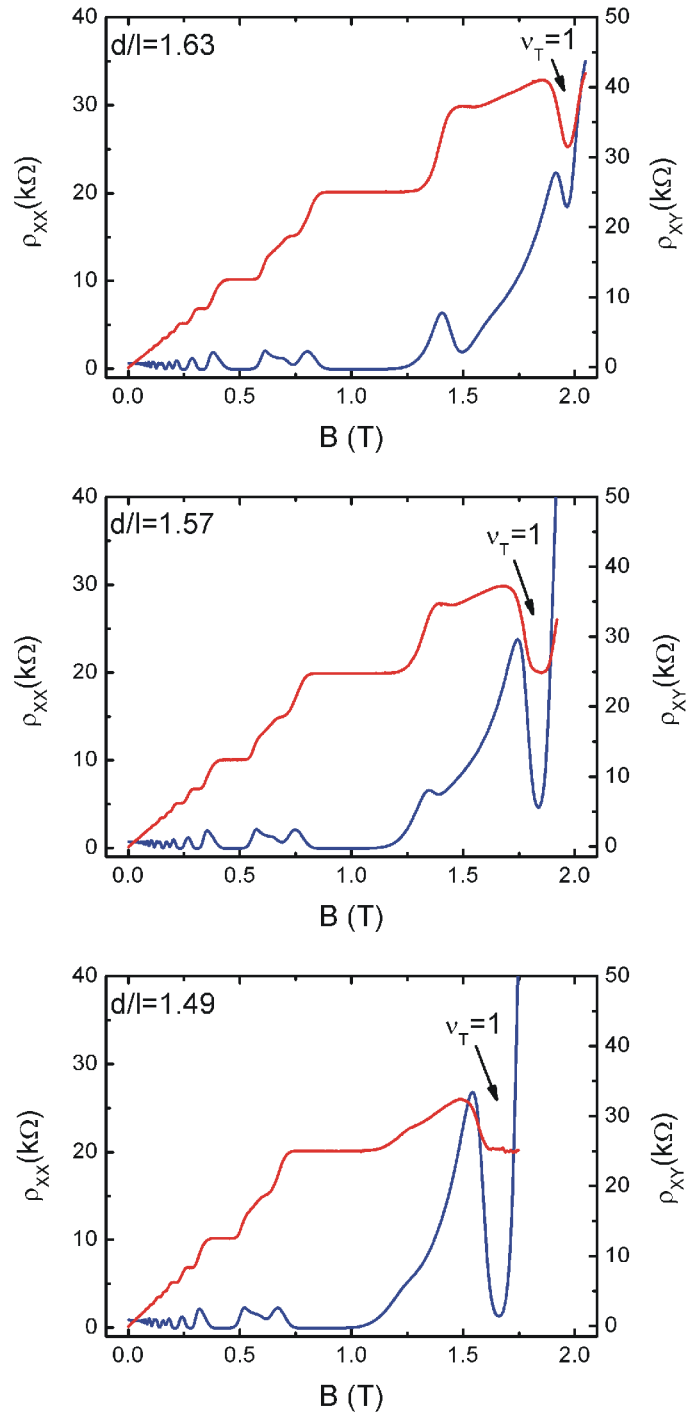
Figure 6.5: Magneto-transport drag measurements at 50 mK with matched electron densities displaying strengthening of the ν_T=1 state as d/ℓ_B is lowered.

layer properties.

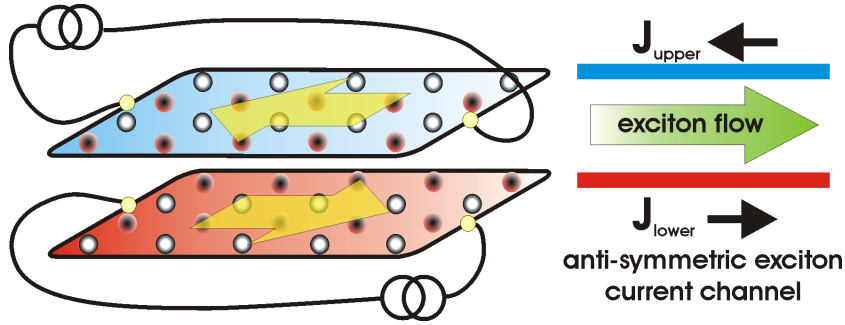## 6.3   Counter-flow Measurements

Figure 6.6: The counter-flow current configuration is produced by sending two equal in magnitude but oppositely directed currents through the two layers. This corresponds directly to the anti-symmetric charge neutral exciton channel, and represents the dissipationless flow of excitons.

The asymmetric current configuration as discussed in Sec. 5.2 can be tested by passing two oppositely directed currents through the two layers as shown in Fig. 6.6. This can be accomplished by either a single voltage source regulated by a large resistor or through the use of two separate phase locked voltage sources. In the single current source case, a current is first passed through one of the layers, extracted, and then redirected via a cable into the other layer but in the opposite direction. This has the advantage of allowing measurements of the extracted current to determine if current has leaked due to interlayer tunneling or other sources before reinsertion into the other layer [5, 6]. In this work two separate phase locked current sources are used or the voltage of a single AC source is split and passed through two isolation transformers which are then current regulated (see Sec. 5.2). The two separate current sources allow investigation of non-equal current magnitudes applied to the separate layers, whereas using isolation transformers allows one to apply an interlayer bias while still being able to send two currents through the sample.

Considering the exciton picture discussed in Sec. 3.3, one can view the ν_T=1 state as consisting of excitons with holes in one layer bound to electrons in the other layer. As sketched in Fig. 6.6, sending two equal but oppositely directed currents through a bilayer system corresponds to sending electrons in opposite directions in the two layers, or in the electron-hole picture, to sending electrons and holes in the same direction. In this situation an uniform flow of excitons in the same direction exists, and according to theoretical models, this exciton current is a dissipationless superfluid of neutral particles unaffected by the presence of a magnetic field!

Counter-flow experimental results are obtained using both the 17/12.4/17 (d040114b-100) and 19/9.6/19 (d041007c-143) samples as listed in Tab. 4.1. The bilayer samples are fabricated using the Hall bar geometry as shown in Sec. 4.3 as to allow independently electrically contacted layers and to allow tuning of the upper and lower layer electron densities through the use of field gates. Transport measurements are done as described in Sec. 5.2 using a Standford SR830 lock-in as a low frequency voltage source where the output was split and sent to two isolation transformers connected to the different layers. AC currents of 0.1 - 0.5 nA at 1.2 - 6 Hz are defined by using large $100\,\text{M}\Omega$ resistors and tuning the output voltage. Magneto-transport measurements of the longitudinal and Hall resistances are made in a cryostat using a dilution refrigerator to reach temperatures down to temperatures of 35 mK.
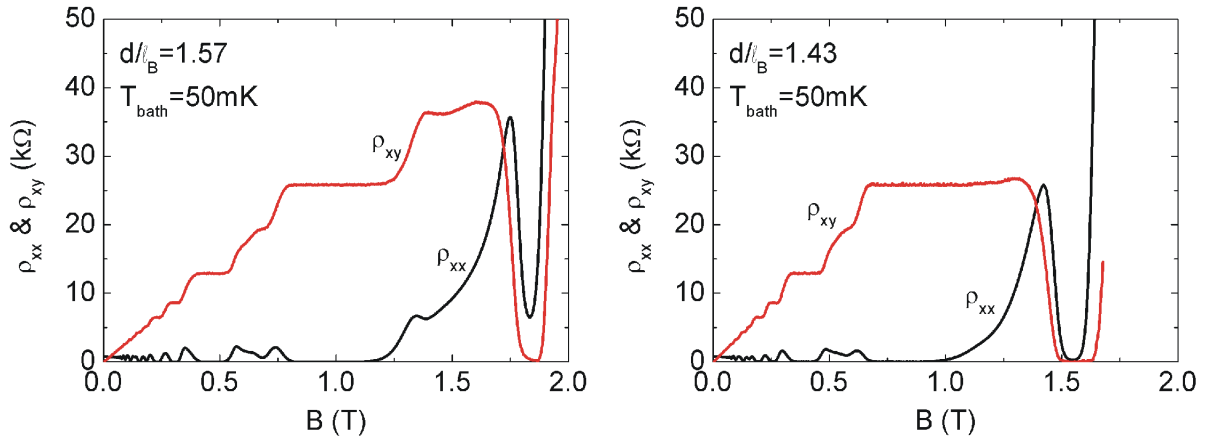

Figure 6.7: Counter-flow measurements at 50 mK with matched electron densities showing ρ_{xx} and ρ_{xy} vs. magnetic field for d/ℓ_B=1.57 (left) and d/ℓ_B=1.43 (right). In both cases at ν_T=1 both longitudinal and Hall resistances tend to zero, but at the lower d/ℓ_B value (i.e. at stronger coupling), the ρ_{xx} and ρ_{xy} minima are deeper.

Fig. 6.7 plots counter-flow data for the 17/12.4/17 (d040114b-100) for two different d/ℓ_B ratios of 1.57 and 1.43 obtained by sending equal but oppositely directed currents though each of the layers simultaneously. In both cases, the layer densities are matched. Irrespective of the layer measured, the d/ℓ_B =1.57 data at ν_T=1 show a pronounced minimum in ρ_{xx} while ρ_{xy} drops approximately to zero. Away from ν_T=1, the traces show Shubnikov-de Haas oscillations of a single layer. At temperatures above 200 mK, the minimum in ρ_{xx} and the zero in ρ_{xy} have disappeared. As seen in Fig. 6.7, decreasing the d/ℓ_B ratio to 1.43 by lowering the electron densities equally in each layer with the upper and lower field gates, leads to a further deepening of the ρ_{xx} minimum and a widening of the zero in ρ_{xy}. Indeed as previously observed [5, 6, 7], both the longitudinal and the Hall voltages in the layers tend to zero at the lowest

experimental temperatures indicating the formation of the neutral superfluid exciton condensate. The amazing disappearance of ρ_{xy} is credited to a current being strictly carried by charge neutral interlayer excitons which are unaffected by the perpendicular magnetic field. Unlike the $\sigma \to 0$ conductivity intrinsic to the IQHE and FQHE states, a superfluid will display an infinite conductivity $\sigma \to \infty$. This is indeed indirectly supported in the counter-flow case since the longitudinal conductivity as given by

$$\sigma_{xx} = \frac{\rho_{xx}}{\rho_{xx}^2 + \rho_{xy}^2},$$
(6.5)

will tend to a large conductivity since as shown by Fig. 6.7 both ρ_{xx} and ρ_{xy} tend toward zero. This behavior is completely new to quantum Hall systems and has never been observed before. The question if this counter-flow is indeed a true excitonic superfluid displaying a macroscopic phase coherence or rather composed of small localized regions of (111) states is currently under investigation both theoretically and experimentally. Theoretically it is claimed different mechanisms exist in the case of parallel, drag, or counter-flow directed current configurations [93]. As sketched in Fig. 6.3 parallel directed currents correspond to a symmetric channel of charged quasi-particles equally distributed between the two layers and flowing in the same direction whereas the asymmetrical counter-flow case is the uniform flow of neutral excitons in one direction. The drag can be considered as a linear superposition of the parallel and counter-flow cases as sketched in Fig. 6.3. Here the quasi-particle and oppositely directed excitonic currents cancel each other out in the drag layer but add in the drive layer.

6.4   Layer Current Imbalances

An interesting experiment involves looking at the ν_T=1 Hall voltage, V_{xy} as the current configuration varies through the parallel, drag, and counter-flow regimes. This is accomplished by fixing the upper layer current to 0.5 nA while varying the lower layer current from -1.0 nA to 1.0 nA. As shown in Fig. 6.8 for the 17/12.4/17 (d040114b-100) sample all three different current configurations (parallel, drag, counter-flow) and their intermediate values are thus investigated. The measured ν_T=1 transverse voltage V_{xy} divided by the upper layer fixed current of 0.5 nA therefore goes from ρ_{xy}= $2h/e^2$ for the parallel case, to ρ_{xy}= h/e^2 for the drag case, and finally to ρ_{xy}= 0 for the counter-flow case, corroborating previous claims [4, 5]. However, taking into consideration the net system current I_{net}= $I_L - I_U$ where I_U and I_L are the upper and lower layer currents respectively, it is found that the Hall resistivity ρ_{xy} is always quantized to h/e^2,

$$\rho_{xy} = \frac{V_{xy}}{I_L - I_U} = \frac{h}{e^2}.$$
(6.6)

Therefore, the slope will always leads to the quantized value of h/e^2, even in the vicinity of the purely antisymmetric counter-flow case. Since the counter-flow case theoretically corresponds
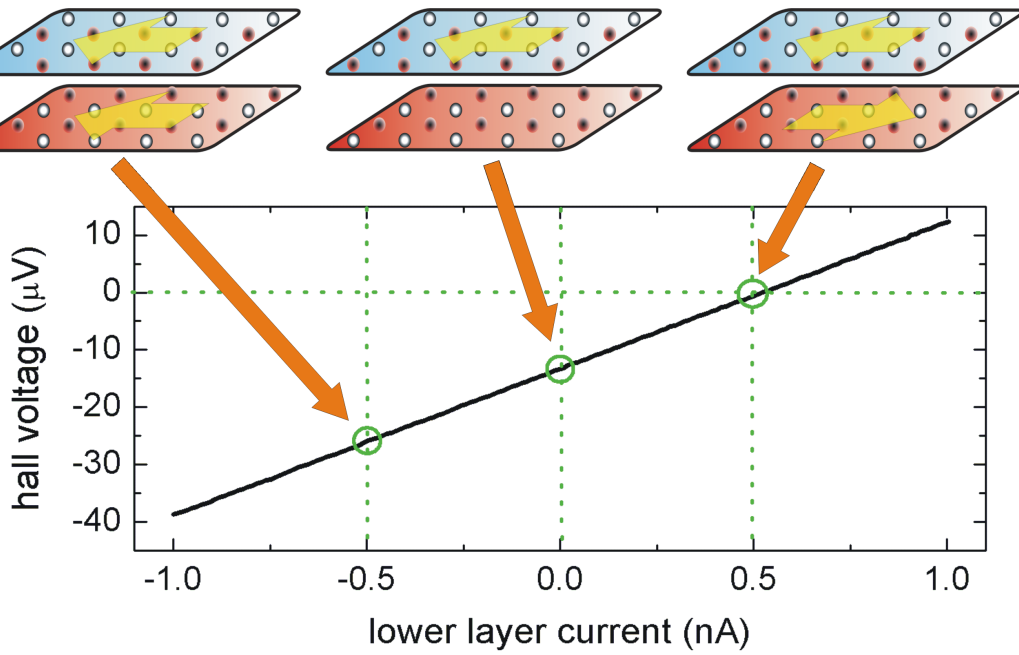
Figure 6.8: Plot of the Hall voltage V_{xy} vs. lower layer current for the $\nu_T=1$ state at 50 mK with matched electron densities. The upper layer current is fixed to 0.5 nA while the lower layer current is varied from -1.0 nA to 1.0 nA allowing V_{xy} to be measured for all current configurations (parallel, drag, counter-flow).

to the formation of a superfluidic exciton state one, may expected to see a discontinuity in the V_{xy} data around the regime where the two currents become approximately equal but opposite. As seen by the linear Hall voltage V_{xy} vs. lower layer current trace this is not the case, and no deviation from the linear is detectable within experimental limits. Here even very near the exact counter-flow case any small net current will lead to a quantized Hall resistivity of h/e^2.

Due to the strongly coupled nature of the $\nu_T=1$ state, one must take into consideration all currents flowing through the system where it is found that any net current leads to a Hall resistance that is quantized at h/e^2 as according to Eq. 6.6. Since there is zero net current in the counter-flow case, a zero Hall voltage will be produced.

6.5 Activated Transport of the Separate Layers

As shown in Fig. 6.5, the longitudinal resistance of the $\nu_T=1$ state deepens with decreasing d/ℓ_B values at a constant low temperature implying a strengthening of the exciton state. We now turn to the temperature dependent investigations of the various resistivities in the drag configuration for the 17/12.4/17 (d040114b-100) sample to further explore the $\nu_T=1$ state. Fig. 6.9 is a plot

of $\rho_{drive,xx}$ for the ν_T=1 state minimum of the lower layer vs. the inverse temperature for a series of different d/ℓ_B values, obtained by adjusting both the front- and back-gates. In all cases one can distinguish between three different temperature regimes: at higher temperatures
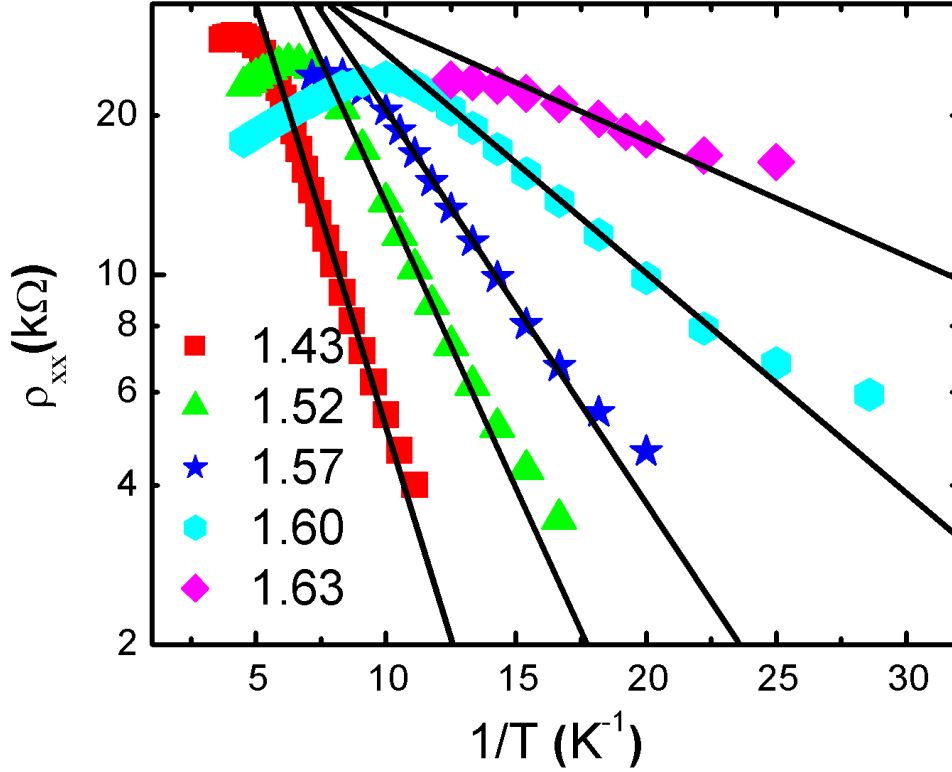

Figure 6.9: Arrhenius plots of $\rho_{drive,xx}$ for 5 different d/ℓ_B values with matched electron densities for the 17/12.4/17 (d040114b-100) sample. Lines are fits to $\rho_{xx} \propto \exp(-\Delta_{\nu=1}/k_BT)$.

the resistance is only weakly temperature dependent as expected for filling factor ν=1/2 for a single layer. With decreasing temperature there is an exponential decrease of the resistance which, in the end, levels off into saturation around $\sim$ 50 mK. At present it is not clear if this is an intrinsic phenomenon or caused by insufficient cooling of the 2D system below 50 mK. From the intermediate exponential range we deduce activation energies by fitting the resistivity vs. $1/T$ data to

$$\rho_{xx} \propto e^{\frac{-\Delta_{\nu=1}}{k_BT}} , \tag{6.7}$$

where $\Delta_{\nu=1}$ is the activation energy. It is not entirely certain whether or not the ν_T=1 state is really a gapped state following Eq. 6.7, however, measurements at $d/\ell_B = 1.48$ have measured the R_{xx} to be thermally activated over three orders of magnitude [5]. The calculated $\Delta_{\nu=1}$ data

with balanced electron densities are plotted in Fig. 6.10 for both the 17/12.4/17 (d040114b-100) and 19/9.6/19 (d041007c-143) various samples. Also included are zeroes corresponding to measurements that did not display a minimum at $\nu_T=1$ at the lowest temperature. Both the temperature dependence of the longitudinal resistivities for the drag and counter-flow current configurations are plotted for the 17 nm sample, whereas only the drag configuration is plotted for the 19 nm QW sample.
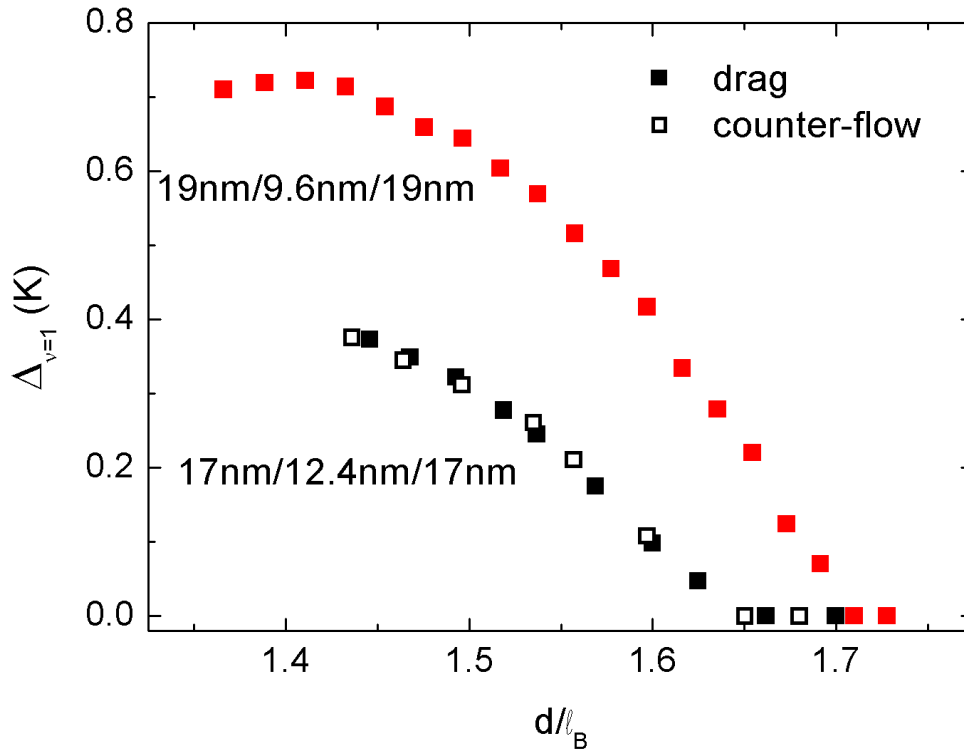

Figure 6.10: Activation energy $\Delta_{\nu=1}$ vs. d/ℓ_B of the $\nu_T = 1$ state for matched electron densities. $\Delta_{\nu=1}$ is plotted for both the drag and counter-flow configurations for the 17/12.4/17 (d040114b-100) sample. For the 19/9.6/19 (d041007c-143) sample only $\Delta_{\nu=1}$ for the drag case is displayed.

In all cases the activation energies in Fig. 6.10 shows a monotonous increase with decreasing d/ℓ_B below a certain $d/\ell_{B,crit}$ which is ~ 1.65 for the 17 nm sample and ~ 1.70 for the 19 nm sample. These $d/\ell_{B,crit}$ values are smaller than the value of ~ 1.83 reported previously [4, 5] and it could possibly be due to our slightly lower mobilities or our smaller interlayer tunneling. The increase of $\Delta_{\nu=1}$ below $d/\ell_{B,crit}$ reminds one of the behaviour seen at a phase transition, for example that of a gap in a superconductor. It is, however, not exactly clear what type of excitations are contributing to the measured $\Delta_{\nu=1}$. In particular, it is not clear if $\Delta_{\nu=1}$ reflects

the thermodynamic condensation energy of the excitonic state.

Focusing on the 17/12.4/17 (d040114b-100) data one can see the drag and counter-flow ρ_{xx} at these d/ℓ_B values display a similar temperature dependence. This is surprising considering different mechanisms have been proposed to cause the resistance in the drag and counter-flow situations [93, 5]. In the counter-flow configuration a uniform flow of neutral excitons across the sample is thought to exist, leading to a zero Hall resistance. Whereas in the drag configuration, in addition to the bulk exciton flow, there also exists a charged quasi-particle current traveling near the edges leading to a quantized Hall resistance [93]. As one goes to the parallel current configuration the charged quasi-particle excitations are the only transport channel [5]. Nevertheless, in both the drag and counter-flow cases the activation energies are the same, both showing a monotonous increase with decreasing d/ℓ_B below a certain $d/\ell_{B,crit}$ which is 1.65 for our sample.

To investigate the universality of the $d/\ell_{B,crit}$ ratio for different samples, temperature dependent measurements in the counter-flow regime are also performed for the 19/9.6/19 (d041007c-143) sample. As denoted by the red square symbols in Fig. 6.10, a critical $d/\ell_{B,crit} \sim 1.70$ is obtained. This is larger than the 1.65 obtained for the 17 nm sample yet smaller than reported ~ 1.83 by other investigations on electron bilayer systems [4,5]. Though the same monotonous increase of $d/\ell_{B,crit}$ with decreasing d/ℓ_B is seen, the activation energies for the 19 nm sample are approximately twice as large as seen in the 17 nm sample. This is quite surprising since the effective center-to-center QW spacing for the 17nm and 19 nm samples are approximately the same (29.4 nm and 28.6 nm, respectively) leading one to expect that as according to the theoretically presented phase diagram of the ν_T=1 state (see Fig. 3.3) one should expect a similar $\Delta_{\nu=1}$ vs. $d/\ell_{B,crit}$ behavior. As shown by M. Kellogg [94], the strength of the ν_T=1 state does not seem to be dependent on the existence of interlayer tunneling as shown by tilted magnetic field and interlayer bias experiments. Therefore, the strength seems to be rather dependent on the quality of the QWs. The 19/9.6/19 sample, though having a lower measured intrinsic B=0 mobility (see Tab. 4.1), displays more FQHE features than the 17/12.4/17 sample at similar electron densities and temperatures. In addition, it has been reported in other works, a 18nm/9.9nm/18nm sample with a similar d of d=28.9 and with a high quality intrinsic low temperature mobility of 1×10^6 cm^2/Vs at 5.4×10^{10} cm^{-2} shows very strong coupled behavior where $d/\ell_{B,crit} \sim 1.8$ [5].

Chapter 7

The ν_T=1 State at Imbalanced Electron Layer Densities

This chapter will explore the role of imbalanced electron densities in the two layers making up the ν_T=1 state. The first section Sec. 7.1, will introduce the concept of imbalanced layers electron densities where the total system density is fixed to a constant value. Sec. 7.2 will present data on the phase boundary existing between the weakly coupled individual layer (ν_U=1/2, ν_L=1/2) case and the strongly coupled ν_T=1 state as obtained from magneto-transport data. Finally, temperature dependent activation measurements of the ν_T=1 state as a function of imbalance will be presented in Sec. 7.3.
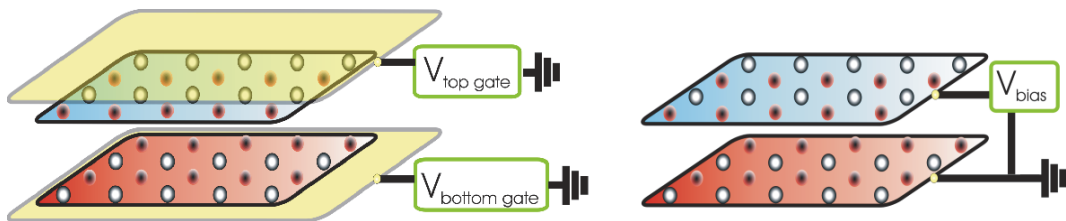
7.1 Density Imbalance

Figure 7.1: Schematic diagrams of configurations used for producing an electron density imbalance in bilayer systems where the total system electron density, n_T=n_U+n_L is held fixed. Imbalance can be either created using the upper and lower field gates (left) or through application of an interlayer voltage bias (right).

In addition to the balanced electron layer density case, the layers can also be symmetrically imbalanced through application of either an interlayer voltage bias, or by using the upper and

lower field gates. These two imbalance methods are depicted in Fig. 7.1, where in both cases the total system electron density, n_T=n_U+n_L is held fixed but the individual layer electron densities (n_U, n_L) are varied. The imbalance is defined as

$$\Delta n = \frac{n_L - n_U}{n_T}, \tag{7.1}$$

where n_U and n_L are the upper and lower electron densities, respectively. Therefore, a positive imbalance will correspond to removing electrons from the upper layer and placing them in the lower layer, whereas a negative imbalance will take electrons from the lower layer and place them in the upper layer. In the pseudospin picture discussed in Sec. 3.3.2 the imbalance is related to the z-component of the pseudospin given by the polar angle θ as shown in Fig. 3.6, and represents the tipping of the pseudospin out of the xy-plane [89]. Here the out of plane pseudospin component $\langle S_z \rangle \propto |u|^2 - |v|^2$ is directly related to the density imbalance between the layers, and any variation of $\langle S_z \rangle$ from a fixed value will cost capacitive energy.

Since the ν_T=1 state is a coupled layer state that is dependent on the total system electron density $(n_T$=n_U+n_L) and not on the individual layer electron densities (n_U, n_L), the ν_T=1 state will remain at a constant magnetic field value with imbalance. This is experimentally shown in Fig. 7.2, where the coupled layer ν_T=1 state remains at a fixed magnetic field while the uncoupled single layer QH states as ν=1 and ν=2/3 shift with layer imbalances.

Although both configurations depicted in Fig. 7.1 can be used to produce an electron density imbalance, there exists some subtle differences between the two methods. In the field gate imbalanced case depicted on the left in Fig. 7.1, each QW 2DES is at the same Fermi energy since one or more contacts in each of the individual 2DESs is connected to the same potential. Application of a negative gate voltage with respect to the 2DES will result in the depopulation of the 2DES as electrons move to the lower potential gate due to the field gate effect. Therefore, to create a density imbalance, one field gate is used to depopulate its nearest 2DES while the other field gate is used to populate the other 2DES in order to maintain a constant total system electron density. The interlayer voltage bias case is subtly different since the Fermi levels of the two QWs are shifted with respect to each other by the applied interlayer bias. Here one of the 2DES is higher in energy by eV over the other 2DES, where V is the applied interlayer bias. Electrons in the higher potential 2DES now have more energy to tunnel into the other QW. A capacitor effect again takes place this time between the two 2DESs, where electrons move from the QW at the higher potential move to the QW at the lower potential resulting in an electron density imbalance.

As discussed in Sec. 6.1 and shown in Fig. 6.1, a slight interlayer voltage bias will quickly lead to suppression of the ν_T=1 coherent tunneling process. It should be noted that this tunneling suppression is not an effect of the density imbalance but rather of the potential difference existing between the QWs. Spielman et al. have done tunneling measurements where the in-
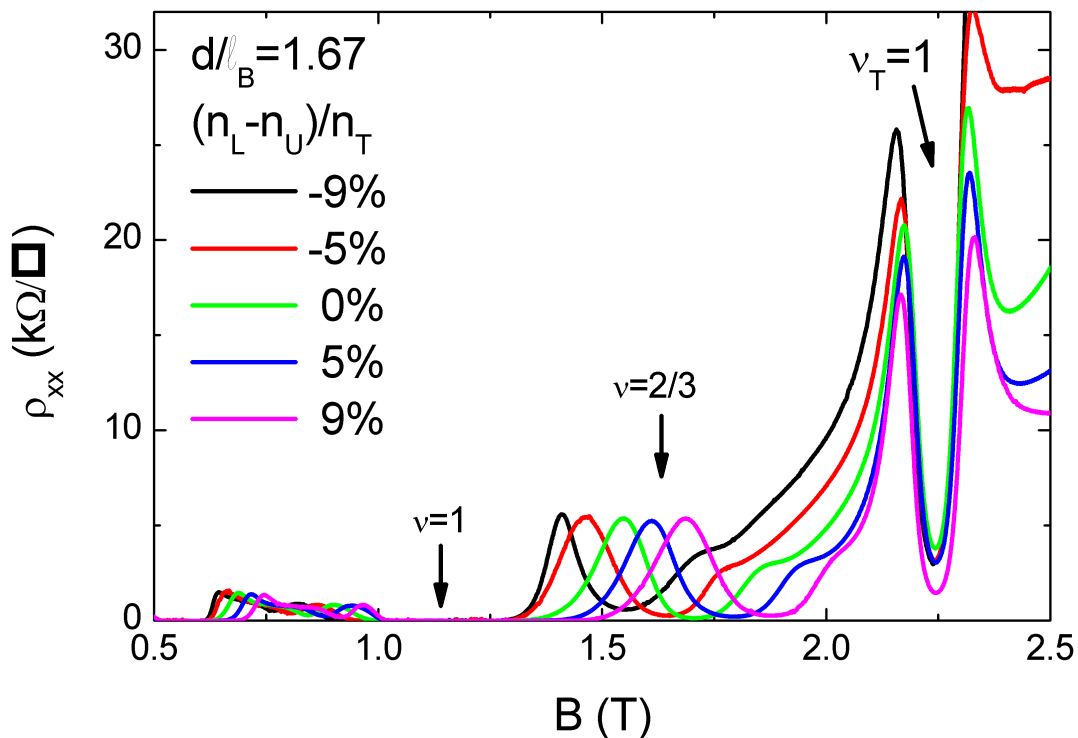
Figure 7.2: Magneto-transport plot of lower layer for the 19/9.6/19 (d041007c-143) sample in the counter-flow configuration for various electron density imbalances. The indicated single layer ν=1 and ν=2/3 QH states shift along the B(T) axis with imbalance whereas the coupled ν_T=1 remains fixed.

duced interlayer imbalance is compensated by continuously adjusting the upper and lower field gates to maintain matched densities while sweeping the interlayer voltage. In both the slightly imbalanced and compensated cases they have found no quantitative differences in the tunneling features for small interlayer biases [3]. In addition, it is found when field gates are used to produce a density imbalance, where both 2DESs are at the same potential, tunneling conductance experiments still show the presence of the ν_T=1 peak at zero interlayer bias [95].

7.2 Phase Diagrams of the ν_T=1 State

The phase transition between the weakly coupled (ν_U=1/2, ν_L=1/2) phase and the strongly coupled ν_T=1 phase is not well understood and has been the subject of various theories [90, 96, 97, 98, 99, 100]. Not known is the order of the phase transition, or even the exact number of phase transitions involved. It has been proposed that in addition to the weakly interacting (ν_U=1/2,

ν_L=1/2) and the strongly coupled ν_T=1 phases there may exist one or more intermediate phases, such as a paired quantum Hall state [96, 97] or a bilayer charge density striped phase [99].
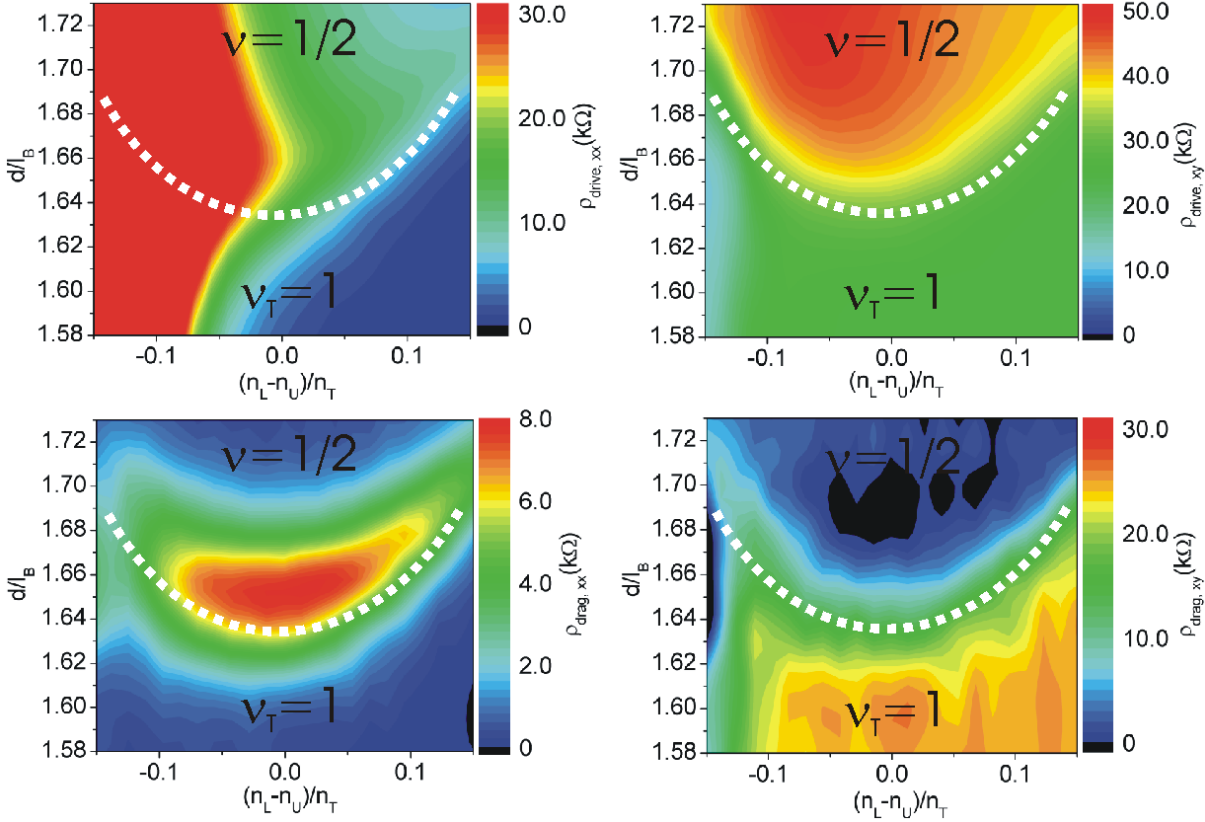

Figure 7.3: Contour plots of d/ℓ_B vs. imbalance of the various resistivities for the 17/12.4/17 (d040114b-100) sample in the drag current configuration. The colors reflect the magnitude of the measured resistivity. The white dashed line is a visual aid displaying the estimated boundary between the weakly coupled (ν_U=1/2, ν_L=1/2) phase and the strongly coupled ν_T=1 phase.

A phase diagram of the ν_T=1 state is experimentally made by sweeping the magnetic field $B_\perp$ to a specific value and then adjusting the front- and back gates to define the center of the ν_T=1 state to exist at this $B_\perp$ with matched densities. At various $B_\perp$ an interlayer bias is added resulting in a symmetric imbalance between the two layers. Therefore, as detailed in Sec. 7.1 one layer has a density of $n + \Delta n$ while the other $n - \Delta n$. Since each $B_\perp$ corresponds to a specific d/ℓ_B, it is therefore possible to construct a phase diagram of the ν_T=1 state as a function of d/ℓ_B vs. imbalance. To facilitate in the quick investigation of ν_T=1 at any desired d/ℓ_B value, the field gate voltages are pre-calibrated such that the individual layer electron density vs. gate voltage are known beforehand. In the drag configuration $\rho_{drive,xx}$, $\rho_{drive,xy}$, $\rho_{drag,xx}$ and $\rho_{drag,xy}$ at ν_T=1 are measured as a function of d/ℓ_B and imbalance for the 17/12.4/17 (d040114b-100)

sample. We have done measurements for several imbalances ($\equiv[n_L\text{-}n_U]/n_T$) between -0.15 and $+0.15$.

All data of the various resistivities in the drag current configuration are plotted in Fig. 7.3 where the color scale is proportional to the measured resistivity. Focusing on the lower right $\rho_{drag,xy}$ contour plot, it can be quickly seen at zero imbalance and $d/\ell_B > 1.66$ that there is essentially no Hall drag signal and that the Hall drive $\rho_{drive,xy}$ is $\approx 2h/e^2$, demonstrating two weakly coupled (ν_U=1/2, ν_L=1/2) layers. Moving to lower d/ℓ_B values with balanced densities, a phase transition from the weakly coupled phase to the strongly coupled ν_T=1 phase is seen to occur at $d/\ell_B \approx 1.65$. This is in full agreement with the temperature dependent studies of the longitudinal resistivity ρ_{xx} as presented in Sec. 6.5, where the same critical $d/\ell_{B,crit}$ ratio is obtained from the activation energy $\Delta_{\nu=1}$ vs. d/ℓ_B data (see Fig. 6.10). Upon crossing this phase boundary, the ν_T=1 phase quickly strengthens with decreasing d/ℓ_B and the transverse resistivities of both $\rho_{drive,xy}$ and drag, $\rho_{drag,xy}$ reach a quantized value of h/e^2. In all cases the transition between the weakly coupled phase and the ν_T=1 state seems to be simple and monotonic as previously shown from the activation energy $\Delta_{\nu=1}$ vs. d/ℓ_B data presented in Sec. 6.5.

Stern and Halperin [98] argue that static fluctuations in the layer densities of real samples lead to a phase separation near the transition boundary. Here, the weakly coupled (ν_U=1/2, ν_L=1/2) phase and the strongly coupled interlayer coherent ν_T=1 phase co-exist. Stern and Halperin represent these two phases as a fraction f, where a $f = 1$ would correspond to the entire sample being occupied by the ν_T=1 coherent phase. Therefore, as d/ℓ_B is lowered from the two completely independent ν =1/2 layer case ($f = 0$) towards the ν_T=1 phase boundary, small puddles of the ν_T=1 phase will initially form throughout the bulk of the sample leading to an increase in $f > 0$. It is predicted that once these ν_T=1 puddles occupy $f \approx 1/2$, percolation will occur, resulting in the longitudinal resistivity components ρ_{xx} and $\rho_{drag,xx}$ going towards zero and the Hall $\rho_{drive,xy}$ and $\rho_{drag,xy}$ becoming quantized at h/e^2. They also account for the large initial increase in the longitudinal drag $\rho_{drag,xx}$ as observed in Fig. 7.3 before percolation. Here they argue that this large longitudinal drag dissipation is a direct cause of the mixture of the two phases, and they predict at $f \approx 0.475$ the longitudinal drag should reach a maximum of $1/2(h/e^2)$.

In addition, other theoreticians have suggested similar models based on competing phases. Simon et al. [100] have used a model of two interpenetrating phases near the transition region to make similar predictions of the observed features. In this model the two phases consist of a composite fermion fluid and the excitonic bosonic fluid. It has also been theorized by Zhou and Kim [90,97] that the transition from the weakly coupled phase to the ν_T=1 state is accompanied by additional intermediate phases. According to their theory the system goes from the ν_T=1 state at low d/ℓ_B, to an interlayer composite fermion paired (33-1) state, and finally to a weakly

coupled compressible phase at high d/ℓ_B. They also predict the possibility of a fourth state consisting of a mixture of the (111) and (33-1) states.

Focusing on the Stern and Halperin model, it is seen in Fig. 7.3 that just before the ν_T=1 phase, $\rho_{drag,xx}$ shows a large increase in resistance to $\rho_{drag,xx} \approx 8000\Omega$ before moving towards zero signaling the ν_T=1 state. The prediction of $\rho_{drag,xx}$ reaching $1/2(h/e^2)$ is not observed anywhere along the phase boundary with imbalance, suggesting a different mechanism involved. Though not quantitatively correct, the model still allows for a qualitative explanation for the large increase in drag resistance near the transition region and also allows for an explaination of the large flanking peaks on either side of the ν_T=1 state shown in Fig. 6.4. As $B_\perp$ moves away from the ν_T=1 filling factor, f decreases leading to the formation of weakly coupled compressible ν =1/2 puddles, these puddles grow until percolation of the ν_T=1 phase is destroyed and the large dissipation due to the mixture of the two phases is seen before the system re-enters the weakly coupled phase.

Additional experimental evidence supporting the Stern and Halperin model is provided by tunneling conductance experiments. Spielman et al. [95] have used interlayer tunneling measurements to construct a d/ℓ_B vs. imbalance phase diagram, where the presence of the ν_T=1 phase is determined by the onset of its zero bias tunneling peak (see Sec. 6.1). They find that the zero bias tunneling peak occurs at higher d/ℓ_B value than the magneto-transport drag measurements of $\rho_{drag,xx}$ and $\rho_{drag,xy}$. Using the Stern and Halperin model, it is argued that before percolation of the ν_T=1 phase, small puddles of coherent interlayer ν_T=1 phase exist randomly located throughout the sample and that these ν_T=1 puddles will still contribute to interlayer tunneling, leading to a detectable tunneling peak before formation of the ν_T=1 magneto-transport signatures.

Moving away from the balanced electron density case towards imbalanced electron layer densities, Coulomb drag measurements reveal that small interlayer biases lead to strengthening of the interlayer coupling. This is particulary apparent in $\rho_{drag,xy}$ of Fig. 7.3 where, even if one is not initially in the strongly correlated phase, it is possible to induce the ν_T=1 phase by imbalancing the system. With imbalance, the phase boundary derived from the drag measurements and the Hall resistance of the drive layer is found to be symmetric around zero imbalance and to fit a quadratic function as shown by the dashed white line in Fig. 7.3. This symmetric behaviour of the phase boundary has also been seen by Spielman et al. [95] to occur in both tunneling and Hall drag experiments.

The strengthening of the ν_T=1 state with imbalance is somewhat surprising since a density imbalance will tip the pseudospins out of the xy-plane, reducing the pseudospin stiffness [89]. Joglekar and MacDonald [101] have been able to account for the stability of the ν_T=1 exciton state against charge imbalance using a Hartree-Fock mean-field theory that assumes that all pseudospins point in the same direction for all electrons in the lowest spin split Landau level.

Here the concept of a magneto-roton minimum in the phase of the collective mode plays an important role in the strength of the interlayer coherent phase. With decreasing d/ℓ_B values, the magneto-roton minimum in the collective mode spectrum of the strongly coupled state deepens. The critical $d/\ell_{B,crit}$ value corresponds to the point when the magneto-roton vanishes and the superfluidic state is destroyed. Imbalancing the system raises this minimum and the phase boundary increases. The shape of the phase boundary is predicted to show a quadric behavior with imbalance, supporting observations in the drag and Hall drive resistivities.

Not predicted or explained by theory is the unusual behavior of the $\rho_{drive,xx}$ resistivity. As shown in the upper left contour plot of Fig. 7.3, the $\rho_{drive,xx}$ behavior is not symmetric around imbalance but rather shows a surprising asymmetric behavior. Here negative imbalances, removing electrons from the drive layer, leads to an enormous increase in the resistivity, whereas positive imbalances, increasing the drive layer density greatly strengthens the ν_T=1 phase! This behavior is completely unexpected and is the main finding of this work. As of yet there has not been any theoretical models accounting for this effect.

7.3 Activated Transport with Imbalance

It is not clear if the excitations contributing to the measured activation energy $\Delta_{\nu=1}$ in Fig. 6.10 really reflect the thermodynamic condensation energy of the excitonic state. To gain insight into this question, temperature dependent resistance measurements are conducted on the separate layers that were symmetrically density-imbalanced for both the drag and counter-flow configuration. If $\Delta_{\nu=1}$ indeed reflects a thermodynamical property of the exciton condensate, then for a fixed imbalance the $\Delta_{\nu=1}$ measured in both upper and lower layer should be the same. Surprisingly, however, it is found that they are very different. Moreover, it is found that at a given imbalance, the properties of one layer strongly resemble those of the other layer at minus that imbalance.

The transport in each of the layers is studied at imbalanced electron densities, yet at a constant total system electron density for the 17/12.4/17 (d040114B-100) sample. The front and back gates are adjusted to have a total density of $2n = 4.44 \times 10^{10}$ cm^{-2} equally distributed between the layers, corresponding to d/ℓ_B=1.57 ($\bigstar$ symbol in Fig 7.4 and Fig 7.5). Then an interlayer bias is added to produce a symmetric imbalance between the two layers, i.e. one layer had $n + \Delta n$, while the other had $n - \Delta n$. In the drag configuration $\rho_{drive,xx}$ and $\rho_{drag,xx}$ are measured as a function of temperature in the respective layers, then the role of the drag and drive layer are interchanged and the procedure is repeated. In the counter-flow configuration, ρ_{xx} in both the upper and lower layer are measured simultaneously as a function of temperature. Measurements are done for several imbalances ($\equiv [n_L\text{-}n_U]/n_T$) between -0.1 and $+0.1$.

In the drag configuration, throughout the range of density imbalances studied, the low tem-
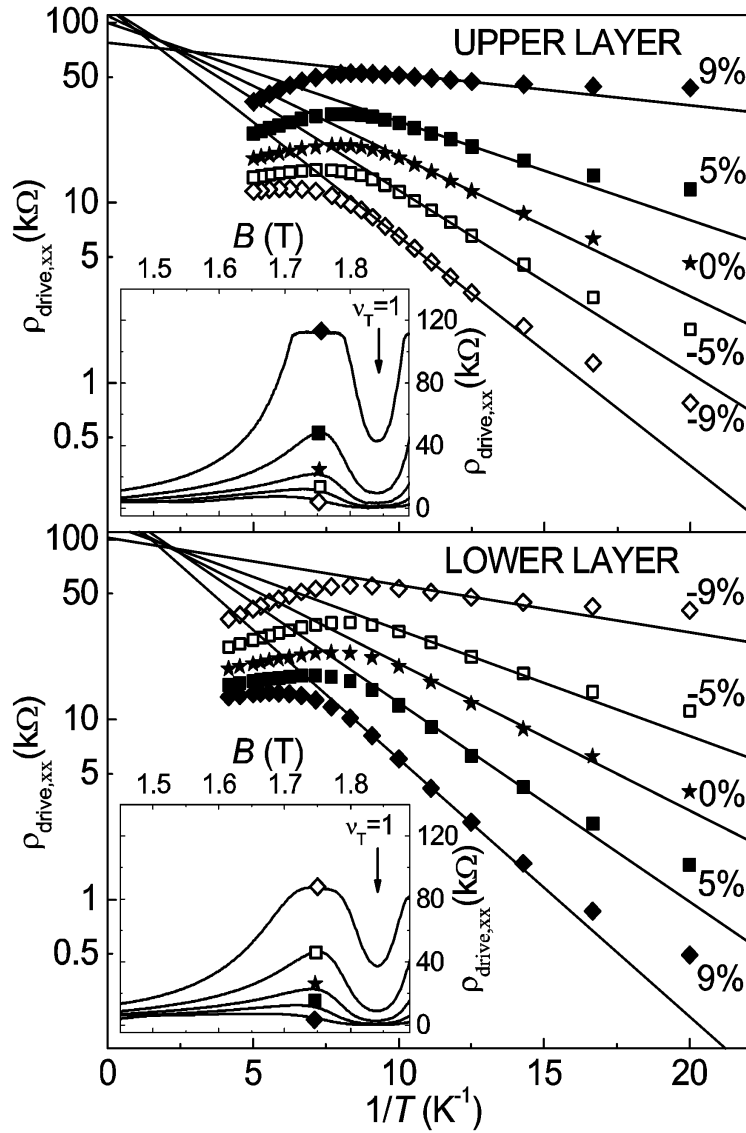
Figure 7.4: Arrhenius plots of $\rho_{drive,xx}$ in the drag configuration for current in the upper layer (top) and for current in the lower layer (bottom). A total of five different imbalances ($\equiv [n_L-n_U]/n_T$) are plotted as indicated in the right of the figure. The insets plot $\rho_{drive,xx}$ at 50 mK vs. magnetic field for these five imbalances. The total electron density is fixed at 4.44×10^{14} m^{-2} corresponding to $d/\ell_B=1.57$.

perature Hall drag remained approximately quantized to h/e^2, indicating that at the lowest temperature nearly all electrons remain paired to holes in the opposite layer. On the other hand, the temperature dependence of the longitudinal resistances for both drag ($\rho_{drive,xx}$, $\rho_{drag,xx}$) and counter-flow (ρ_{xx}) configurations all change significantly with imbalance. Focusing on the drag
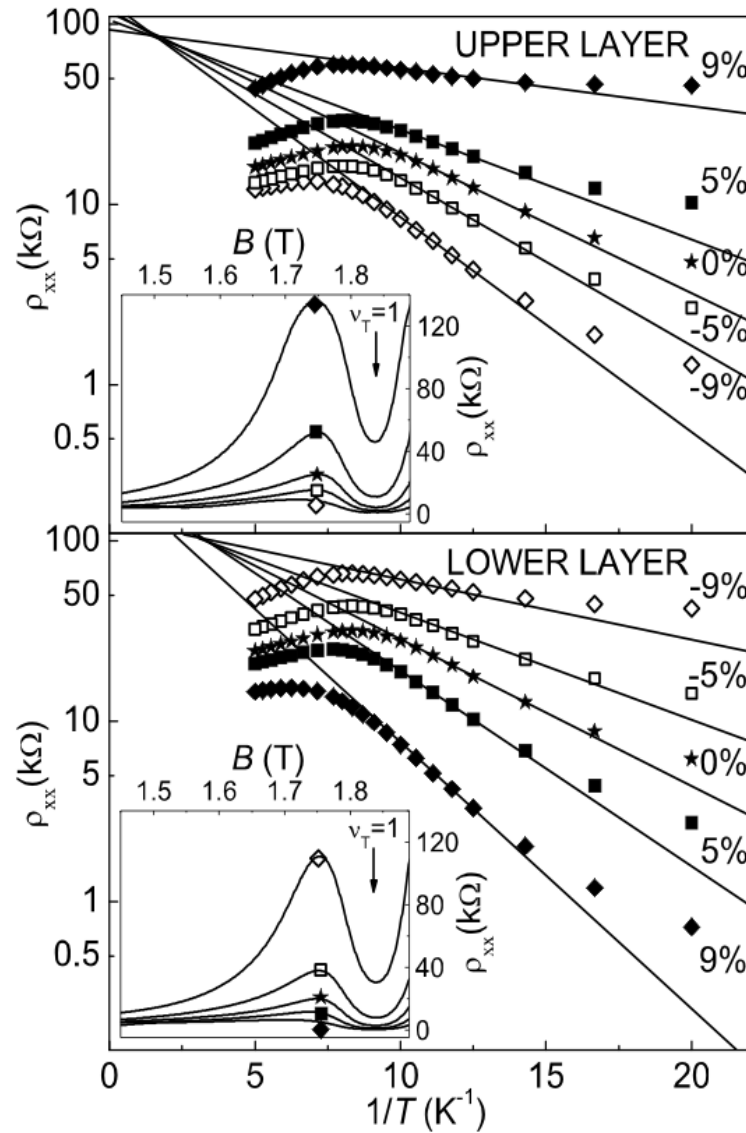
Figure 7.5: Arrhenius plots of ρ_{xx} in the counter-flow configuration for the upper (top) and the lower (bottom) layers using five different imbalances ($\equiv [n_L$-$n_U]/n_T$). The insets plot ρ_{xx} at 50 mK vs. magnetic field for these five imbalances. The total electron density is fixed at 4.44×10^{14} m^{-2} corresponding to d/ℓ_B=1.57.

configuration, the lower part of Fig. 7.4 plots the lower layer $\rho_{drive,xx}$ vs. inverse temperature for various density imbalances. Strikingly, upon increasing the imbalance from negative to positive values (i.e. increasing the lower layer density while simultaneously decreasing the upper layer density), the activation energy measured in the lower layer increases. Upon interchanging the role of the two layers and sending a current in the upper layer (upper part of Fig.

7.4), we find that the upper layer $\rho_{drive,xx}$ at a given imbalance resembles that of the lower layer $\rho_{drive,xx}$ but for minus that imbalance. As a consequence, the activation energy determined from the upper layer $\rho_{drive,xx}$ decreases with increasing imbalance (i.e. it increases with increasing the upper layer density). In the counter-flow configuration (Fig. 7.5), temperature dependent measurements of both the upper and lower layer ρ_{xx} were made simultaneously and the same observation is made, i.e. with imbalance the layer with increasing electron density has an increasing activation energy whereas the the other layer, with the decreasing electron density, has a decreasing activation energy.
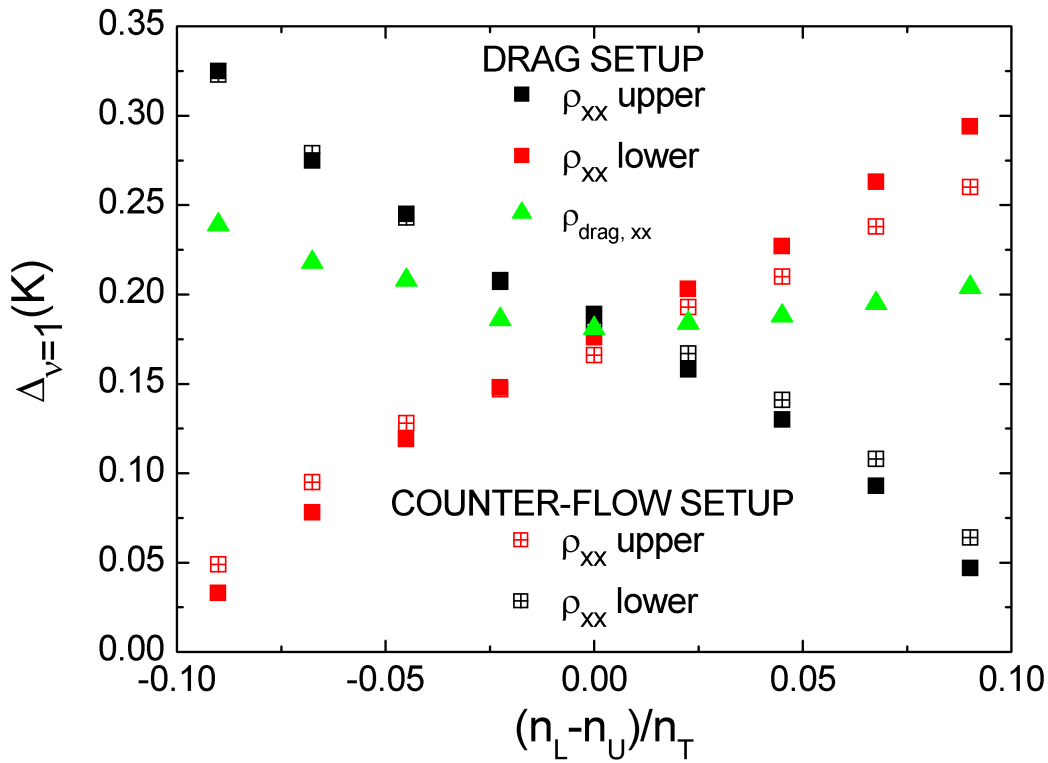

Figure 7.6: Activation energies of the $\nu_T = 1$ state vs. density imbalance for drag and counter-flow configurations. (■) and (♦) correspond to the activation energy determined from ρ_{xx} in the upper and lower layer in the drag configuration. (□) and (◊) correspond to the activation energy determined from ρ_{xx} in the upper and lower layer in the counter-flow configuration. (▲) denotes the activation energy obtained from the longitudinal drag. For all data $d/l_B=1.57$

This asymmetry of the activation energies of the separate layers with imbalance is summarized in Fig. 7.6. It indicates that the measured activation energies do not reflect the condensation energy of the excitonic state nor the binding energy of the excitons, both of which should

be independent on whether it is measured in the upper layer or in the lower layer. Instead, our measurements imply that the activation energy reflects a gap to charge-excitations in the *separate* layers that form the bilayer condensate and that the excitation spectrum of a layer is substantially different for positive and negative imbalance. As with the $\Delta_{\nu=1}$ vs. d/ℓ_B in Fig. 6.10 we find that with imbalance the activation energies obtained in the drag and counter-flow configurations are again approximately equal. The asymmetry further tells us that upon increasing the density in one layer, while keeping the total density constant, it costs more energy to produce excitations in that layer. This is consistent with previous observations that find that for d/ℓ_B slightly higher than the critical value (where no $\nu_T=1$ state can be observed for matched densities), a density imbalance can induce the $\nu_T=1$ state [95]. Under such circumstances, we observe a minimum in ρ_{xx} at $\nu_T=1$ with thermally activated behavior only in the higher-density layer, while ρ_{xx} of the lower-density layer shows no trace of the correlated state at all.

The very different resistances of the layers with imbalance also sheds new light on the alleged disappearance of the insulating (high resistance) phase near $\nu_T=1$ observed in experiments on not separately contacted bilayers [102]. The insets of Fig. 7.4 and Fig. 7.5 plot ρ_{xx} of the upper and lower layer at 50 mK vs. magnetic field for the imbalances indicated in the main figure by the corresponding symbols. Upon decreasing the lower layer density (lower parts of Fig. 7.4 and Fig. 7.5) the insulating phase in the lower layer becomes much stronger. Simultaneously the upper layer gets a higher density and its insulating phase disappears (upper parts of Fig. 7.4 and Fig. 7.5). Our data thus show that the insulating phase survives in the lower-density layer. We further note that this insulating behavior in the lower-density layer is not simply due to its somewhat reduced mobility, since reducing the total density such that both layers have this lower density, results in a much weaker insulating phase than that observed in the lower-density layer in the imbalanced case.

Chapter 8

Excitonic Superfluid DC Transformer

This chapter investigates the potential realization of a DC step-up transformer using the ν_T=1 excitonic state. The data presented in this chapter are based on a theoretical idea initially proposed by Girvin [14] and are its first experimental attempt to the author's knowledge. The first section, Sec. 8.1 discusses some of the basic theoretical aspects of a transformer built using the ν_T=1 state, and the last section, Sec. 8.2 presents some exciting new experimental data obtained from a constructed DC transformer showing step-up voltage behavior in the drag layer.

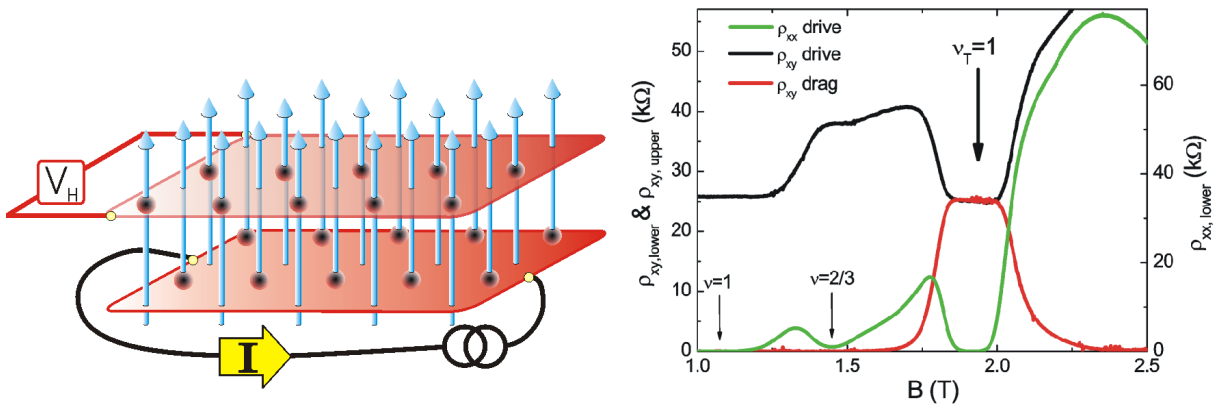## 8.1 Principles of a ν_T=1 Step-Up DC Transformer

Figure 8.1: As explained by Girvin [14] (see Sec. 6.2) the quantized Hall drag of the ν_T=1 state can be viewed as resulting from a current I dragging the fluxes attached to electrons through both layers (left). This induces a voltage drop across both layers that is perpendicular to the current direction and induces a quantized resistance of h/e^2.

Bilayer systems showing the ν_T=1 state will display the peculiar characteristic of an equal

transverse voltage drop across both drive and drag layers when a current I is driven only through one of the layers ("drive layer") and no current is passed through the other layer ("drag layer"). This is dramatically demonstrated in the right plot of Fig. 8.1 where the low temperature magneto-transport measurements of both the transverse drive and drag resistivities are exactly the same, thus corresponding to the voltage drop across both layers being of equal magnitude. In both drive and drag layers this voltage drop is perpendicular to the current I and equal to Ih/e^2. Experiments have determined the transverse drag resistance to be precisely quantized to h/e^2 within an accuracy of order 10^{-3} [4]. Theoreticians have proposed, using this extraordinary feature of a quantized Hall drag, to construct a DC transformer [14, 15]. In this case the primary of the transformer corresponds to the drive layer and the secondary to the drag layer. The actual transforming action can be viewed within the composite boson picture as arising from the flow of Chern-Simons fluxes attached to the particles. Since the Chern-Simons fluxes are attached to the electrons, a current flow I will cause fluxes to be dragged through both layers leading to an induced voltage drop in both layers that is perpendicular to the current.
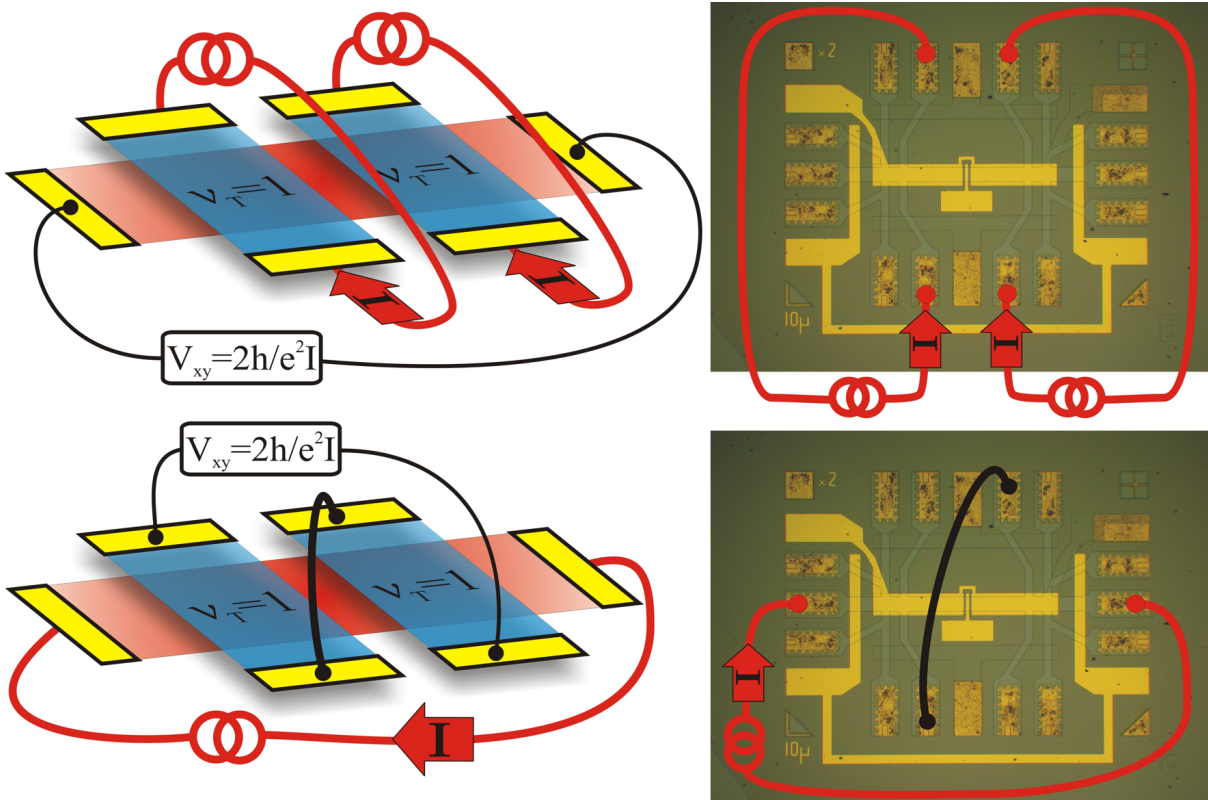

Figure 8.2: The left is a sketch of the two proposed DC transformer designs (parallel, series) by Halperin, Stern, and Girvin [15] using the ν_T=1 state to step-up a voltage in the drag layer. On the right is shown the actual experimental implementation of the parallel and series designs.

Two proposed design configurations for stepping up the secondary voltage [15] are sketched in Fig. 8.2 together with their actual experimental implementation. In both designs the upper layer is separated into N coupled ν_T=1 stages through the use of small plunger gates to locally deplete a small region of width L_d in the upper 2DES. In the first design the primary is the upper layer and a current is driven in parallel through the N stages. With a current I_1 flowing through each stage a voltage $V_2 = N I_1 h/e^2$ is induced in the lower secondary layer. In the second design a current I_1 is driven through the lower layer and the N secondary stages are connected in series leading again to a stepped up voltage of $V_2 = N I_1 h/e^2$. In both cases it is assumed that no secondary current is drawn. In the situation that a nonzero current $I_2 \neq 0$ is drawn from the secondary layer, it is claimed that the ratio of the secondary to the primary voltage (V_2/V_1) will decrease since the output impedance of the transformer is nonzero [15]. For instance, if the primary current I_1 is held fixed and the secondary drawn current I_2 is increased then V_2 will decrease and V_1 will increase. However, for the case where I_2 is sufficiently small V_2 should be higher than V_1 given a suitable number of ν_T=1 stages N.

In the case of equal layer electron densities, each coupled ν_T=1 region will be separated by a small ν=1/2 single layer region due to the finger depletion gate. This makes analysis of the current flows and voltage drops in the primary layer nontrivial. Using macroscopic conductivity laws and Kirchoff's equations Halperin, Stern, and Girvin have given a theoretical prediction of the expected current flows and voltages in each layer. In their analysis it is assumed the $(N-1)$ plunger gate depleted regions have a $\rho_{xy} \approx 2h/e^2$ and ideally, with small depletion widths L_d, a small longitudinal resistivity $\rho_{xx} = \epsilon \ll 1$. For the ν_T=1 regions it is assumed $\rho_{xx} \to 0$ and $\rho_{xy} = h/e^2$. Using these initial assumptions Halperin et al. find a current flowing in the y-direction in the depleted regions. To conserve the total primary current I_1, it is therefore predicted that an "extra" inhomogeneous current must flow diagonally across the ν_T=1 regions. This inhomogeneous current varies depending on the ratio L_d/w where w is the sample width. Taking in consideration these inhomogeneous currents a constant resistance R^* of the depleted region is calculated for three different possible regimes of L_d/w and ϵ. The first regime corresponds to $L_d/w \to 0$ or to when the system is very wide with respect to L_d, here R^* is

$$R^* = \frac{L_d}{w\epsilon}\left(\frac{h}{e^2} + \epsilon^2\right), \tag{8.1}$$

hence, R^* can be made arbitrary small by using a sample with a large width w and a small depletion length L_d. The next regime is when $\epsilon \ll L_d/w \ll \epsilon^{-1}$, in this case R^* becomes

$$R^* = \frac{h}{e^2}. \tag{8.2}$$

Finally, the third regime is when L_d is large or $\epsilon \ll L_d/w$. Now the resistance of each stage is just proportional to the longitudinal resistivity of the depleted region,

$$R^* = \epsilon \frac{L_d}{w}. \tag{8.3}$$

The total resistance of the primary due to the depleted regions is $(N - 1)R^*$. Including the additional resistance of the current input and output arms the total resistance of the primary layer in the first regime ($L_d/w \ll \epsilon$) is predicted to be

$$R_N = \frac{V_1}{I_1} \approx ((N - 1)R^* + 3)\frac{h}{e^2}. \tag{8.4}$$

Therefore, for a $1 : 1$ transformer having an input and output current arm and one ν_T=1 region ($N = 1$) the total primary resistance will be $R_1 \approx 3h/e^2$ (not including contact resistances).

8.2   Experimental DC Transformer Realization

A transformer with a single plunger gate of width of 10 μm is used to divide the upper 2DES into two sections as shown in Sec. 4.3.2. The wafer used is 19/9.6/19 (d041007c) and consists of two 19 nm QWs separated by a superlattice of 9.6 nm total thickness made up of alternating four monolayers (ML) of AlAs (1.13 nm) with one ML GaAs (0.28 nm). The measured low temperature 4.2 K interlayer resistance at zero magnetic field is found to be $\sim$ 80 MΩ (see Tab. 4.1). The 2DES electrons originate from two bulk Si doped regions placed 300 nm below and 280 nm above the wells. Both the upper and lower layers show similar intrinsic densities and mobilities of $\sim 4.0 \times 10^{10}$ cm^{-2} and $\sim$ 500000 cm^{2}V^{-1}s^{-1} without illumination. A selective field gate depletion technique (see Sec. 4.2), using metallic front gates and buried back gates, allow the layers to be individually contacted. In this sample eight Ohmic contacts are made to the upper 2DES and six to the lower 2DES. Upon application of a negative voltage (-0.28 V) to the plunger gate, the upper layer is split into two regions, each having four Ohmic contacts. The density of both layers can be independently fine tuned by a back gate located under the Hall bar and a metallic front gate that only covers the two upper layer ν_T=1 regions regions. The total Hall bar dimensions are 880 μm in length and 80 μm in width. The dimensions of the depleted region will include the plunger gate width plus the two 5 μm gaps existing between the plunger gate and front gate as detailed in Sec. 4.3.2. The depletion region for this sample is therefore L_d= 10μm + 10μm, thus corresponding to a L_d/w= 20/80. All measurements are done in a dilution refrigerator at temperatures down to 35 mK. AC currents of $0.2 - 1.0$ nA at 1.92 Hz are used to measure the longitudinal and Hall resistances, where the linearity of all the measurements was tested under all measurement conditions and no significant deviations were found up to $\sim$ 2.0 nA.

   To eliminate unwanted effects of the plunger gate also effecting the lower layer electron density, the following experiments are performed. The left plot in Fig. 8.3 shows the longitudinal resistivities for the upper, $\rho_{upper,xx}$ and lower, $\rho_{lower,xx}$ layers as a function of plunger gate voltage V_{pl} at zero magnetic field. Both $\rho_{upper,xx}$ and $\rho_{lower,xx}$ are measured across the plunger gate. As shown in Fig. 8.3, the upper layer $\rho_{upper,xx}$ increases dramatically when $V_{pl} < -0.2$
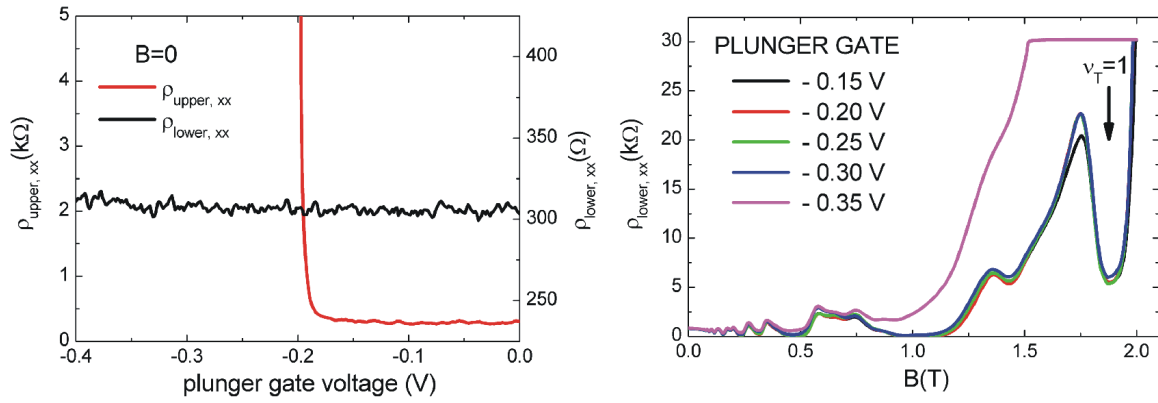
Figure 8.3: On the left is plotted the B =0 longitudinal resistivity data of the upper ($\rho_{upper,xx}$) and lower ($\rho_{lower,xx}$) layers as a function of plunger gate voltage V_{pl}. On the right are shown magneto-resistance curves of $\rho_{upper,xx}$ and $\rho_{lower,xx}$ for various values of V_{pl}.

V corresponding to the upper layer being pinched off into two sections. The upper layer is now no longer continuous but contains a locally depleted region existing in the middle of the Hall bar under the plunger gate. As seen in the plot, the lower 2DES is unaffected in the range of applied plunger gate voltages, remaining essentially constant at $\sim 310 \ \Omega/\square$.

Since the electron behavior of a 2DES changes drastically upon application of a perpendicular magnetic field $B_\perp$, the effect of the plunger gate on the lower 2DES is also tested by performing a series of magneto-transport sweeps. The right plot of Fig. 8.3 is a set of magneto-transport curves of $\rho_{lower,xx}$ for different values of V_{pl}. It is found the traces are practically identical when $V_{pl} < -0.3$ V as shown by their overlap. For $V_{pl} > -0.3$ V the weak magnetic field $\rho_{lower,xx}$ data is essentially the same, however, a large increase in the resistivity is seen at higher fields indicating the plunger gate is affecting the lower layer. To reduce complicating the experiment due to disruption of the lower layer, a plunger gate voltage of V_{pl}= -0.28 V is used for all experimental measurements. At this setting the upper layer is completely depleted below the plunger gate and the lower layer is unaffected.

A curious characteristic of this particular 19/9.6/19 (d041007c-55) sample is an intrinsic inhomogeneity in the lower layer electron density. Surprisingly, there exists an intrinsic density variation only in the lower layer, where one end of the Hall bar displays a higher electron density than the other end. This is not observed in the upper layer where the electron density is found to be homogeneous. Since other bilayer samples processed from the same wafer did not display this effect, this non-ideal intrinsic density variation is most likely attributed to a localized crystal inconsistency formed on the wafer during the MBE growth process. Though interesting, the actual mechanism leading to this lower layer variation is unknown and a full
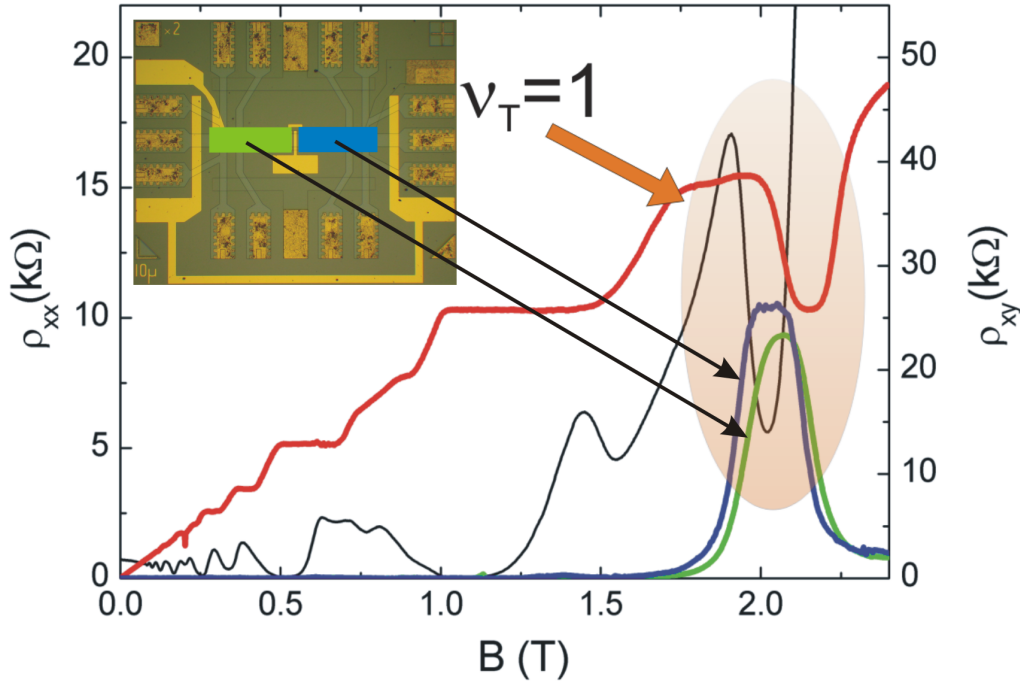
Figure 8.4: Magneto-transport data of the various resistivity for zero plunger gate voltage for the 19/9.6/19 (d041007c-55) sample at $\sim$ 35 mK. The inset shows the two measured ν_T=1 drag regions of the transformer used to obtain the similarly colored curves.

discussion is beyond the scope of this work.

Fig. 8.4 displays low temperature (35 mK) magneto-transport data with zero plunger voltage V_{pl} = 0.0 V. Normally, the ν_T=1 state occurs with the longitudinal ρ_{xx} minimum being located at the center of the Hall ρ_{xy} plateau and with all Hall plateaus being located within the same magnetic field range irrespective of where along the Hall bar they are measured. As shown, this is not the case due to the density inhomogeneity of the lower layer. Therefore, it is not possible to obtain equally matched layer densities but rather there will always exist different degrees of density imbalance as one moves down the Hall bar. The ν_T=1 state measured across the lower layer contacts (green) at one end of the Hall bar (see inset Fig. 8.4) occurs at a slightly higher magnetic field value of B= 2.2 T (d/ℓ_B= 1.73). This occurs since in this region the total electron density (n_T= $n_L + n_U$) is larger due to a higher n_L. The Hall drag peak (blue), as measured by the next set of contacts, shows a ν_T=1 state shifted to lower d/ℓ_B values since the lower layer density has decreased. The lower longitudinal $\rho_{lower,xx}$ trace is a measurement made along the entire length of the Hall bar, and is therefore an average over the entire density inhomogeneity of the ν_T=1 state.

Upon applying a plunger gate voltage of V_{pl}= -0.28 V, the upper layer is effectively divided into two ν_T=1 regions. The lower longitudinal $\rho_{lower,xx}$ is now a nontrivial measurement of the two ν_T=1 regions and a single ν=1/2 region [15]. Focusing only on the secondary layer, it is found that the measured Hall drag resistivies remain unchanged from the V_{pl}= 0.0 V case since they are measured in regions located far away from the plunger gate.
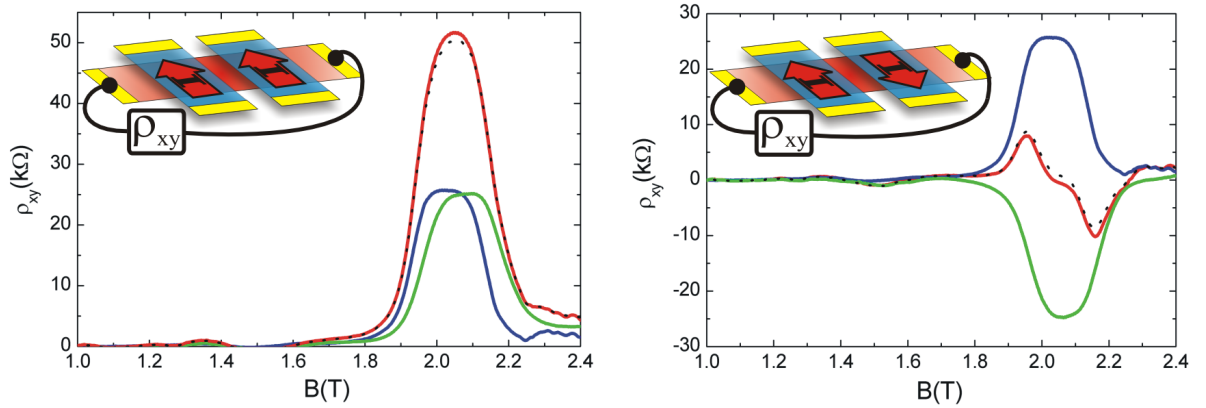

Figure 8.5: Step-up voltage data obtained using parallel (left) and anti-parallel current configurations with V_{pl}= -0.28 V. Schematics of the two configurations are shown in the insets.

Data obtained using the parallel DC voltage step-up configuration is plotted on the left in Fig. 8.2. Low frequency phase locked AC currents are passed across the various sections of the upper primary layer and the voltage on the lower secondary layer is recorded. The parallel configuration is sketched in the inset of Fig. 8.5 and represents the case when two phase locked 0.5 nA AC currents are sent in parallel across the two ν_T=1 sections. The case when only a single 0.5 nA current is sent through either the "blue" section or the "green" section are represented by the blue and green traces of Fig. 8.5, respectively. In these cases, both the traces are approximately quantized to h/e^2 as expected for the ν_T=1 state in the drag configuration. As mentioned previously, the noticeable shift of the quantized drag plateaus between the two sections is related to an intrinsic electron density inhomogeneity in the lower layer. Upon applying two 0.5 nA currents across both sections simultaneously, the Hall drag voltage doubles to approximately $\sim 2h/e^2$ as shown by the red curve. This indeed confirmers the transform action since the addition of the two single current cases (blue and green) result in a curve (dashed black) which essentially overlaps the parallel case. Here as expected the induced Hall drag voltages in the secondary layer are being added up in series.

Reversing the current direction in one of the ν_T=1 regions results in an anti-parallel current configuration where the two equal magnitude currents are sent in opposite directions as shown in the inset of the right plot of Fig. 8.5. As before the blue and green traces represent the single

current source case and show the h/e^2 quantized behavior of the ν_T=1 state. However, upon applying two equal but oppositely directed currents across the two sections, the secondary now does not show the $2\times$ step-up voltage of $\sim 2h/e^2$ as seen in the parallel case, but rather the subtraction of the two induced drag voltages. This is confirmed since subtracting the blue and green curves indeed result in a curve (dashed black) that overlaps the antiparallel case. Here two Hall drag voltages have been induced in series in the lower secondary layer with equal magnitude but with opposite polarity resulting in a net cancelation.
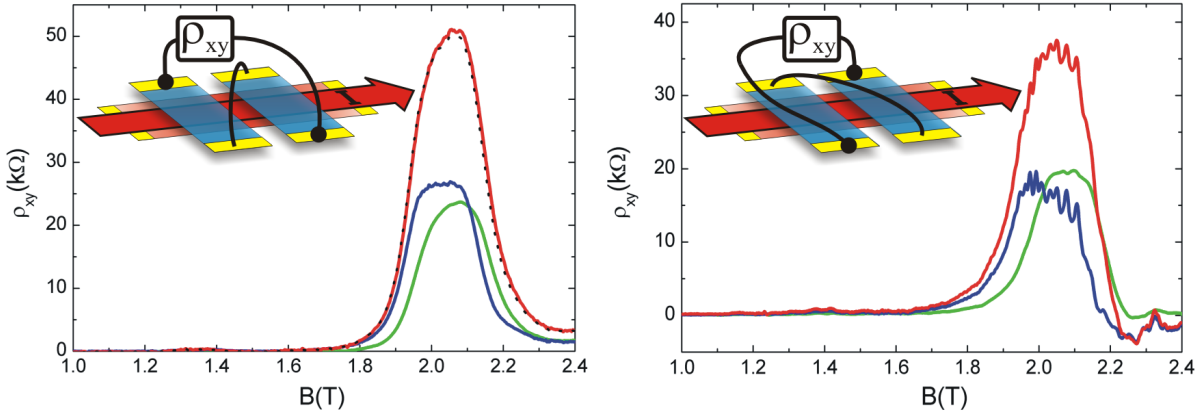

Figure 8.6: Step-up voltage data obtained using two different types of series configurations as schematically shown in the insets. The left shows the expected step-up voltage behavior of $\sim 2h/e^2$ whereas the right plot shows noise that could be potentially due to non-ideal contacts.

The second configuration as suggested by Halperin et al. [15] is to send a single 0.5 nA current through the lower primary layer and to connect the induced Hall drag voltages of the two sections in series through a cable as sketched in the inset of Fig. 8.6. The blue and green curves of the left plot correspond to the Hall drag ρ_{xy} plateaus measured in the two sections of the upper secondary layer when a 0.5 nA current is sent through the lower primary layer. Upon connecting the two ν_T=1 regions in series with a cable, the secondary output voltage as measured across the two sections is approximately $\sim 2h/e^2$. Adding the two separate Hall drag voltages of the blue and green traces results again in a trace (dashed black) that completely overlaps the connected series configuration output. Though the order in which the two sections are looped in series should not play a role, it is nevertheless found that the case denoted in the right plot of Fig. 8.6 is different from the left graph. Here a reduction in the magnitude of the Hall drag voltage is seen in the green trace and noise is measured in the induced Hall drag voltage of the blue region. The combined series voltage measured across the two layers also shows noise. This is most likely due to poor contacts between the two regions that are

connected in series. Since one of the regions depends on the connecting cable to act as the potential reference, a non-ideal contact will result in a poorly defined potential of the blue layer leading to the observed noisy behavior seen in Fig. 8.6. Nevertheless, further investigations are required using different samples before a definite statement can be made.

Chapter 9

Summary and Conclusion

The initial goal of this work was the reproduction of previous experimental claims by other groups. This has has been successfully accomplished in being the first group to successfully reproduce the zero bias resonate interlayer tunneling, the quantized Hall drag, and the counterflow data in two dimensional electron bilayer systems [7]. In all these previous experimental claims we find qualitative agreement of the results and in some cases have been able to clarify some misleading interpretations (see Sec. 7.3). The second goal of this thesis is to provide further characterization on the properties of this relatively unknown bilayer quantum Hall state. This has also been successfully accomplished by the discovery of asymmetric activation energies in the separate layers with imbalance [7]. The following points present the main findings of this work.

- **Interlayer Tunneling** - Using selective area field gate depletion techniques, independent contact to the individual layers are realized. It is therefore possible to make interlayer tunneling conductance experiments between the two closely spaced layers. For the $17/12.4/17$ (d040114B-100) sample, the measured B=0 T interlayer sample resistance is found to be several GΩ. No detectable resonance tunneling peak features at B=0 T or finite magnetic field values away from the ν_T=1 state are seen in the dI/dV vs. interlayer voltage measurements within the noise level (0.5×10^{-9} Ω^{-1}). As one moves to the ν_T=1 state for balanced layer electron densities a large zero interlayer voltage tunneling peak emerges when d/ℓ_B is below a certain critical value, and increases in magnitude with lower d/ℓ_B ratios. This is only the second time the zero interlayer voltage tunneling peak has been reported and is the first time the zero interlayer voltage tunneling peak has been reported in a sample showing no B=0 T resonance tunneling features [3, 103]. Compared to the sample of Spielman et al. [3], which has a similar area (250 μm $\times$ 250 μm), it is found for similar temperatures (T= 40 mK) and d/ℓ_B ratios that our tunneling is at least one order of magnitude lower. This is surprising since both the $17/12.4/17$ (d040114B-100) sample and the $18/9.9/18$ Spielman sample have a similar center-to-

center QW spacing d of 29.4 nm and 27.9 nm, respectively, and should display similar ν_T=1 characteristics. The difference between the Spielman et al. sample and our sample most likely relates to our thicker 12.4 nm AlAs/GaAs superlattice barrier or narrower QWs which displayed lower electron mobilities.

MacDonald [80] has proposed that the interlayer tunneling is proportional to the length of the sample edges in the ν_T=1 excitonic state. This theory offers little support to the observed differences in the conductance peak magnitudes since due to our Hall bar geometry our sample edge length is $\sim 48\%$ larger than that of Spielman et al., even though our sample area is only $\sim 11\%$ greater. Although suggestive of a Josephson effect, present experimental data do not exhibit the infinitely large and narrow zero bias conductance characteristic of a true DC Josephson effect as seen between two superconductors. While vastly enhanced, the zero bias peak remains finite and the FWHM attains a minimum but nonzero value as T$\to 0$. It is not known if the finite height and width are intrinsic to the ν_T=1 state or rather an artifact of imperfect sample conditions. The height and width of the zero bias conductance peak are adversely effected by extrinsic electromagnetic interference, leading to a lowering and broadening of the peak. Also limited cooling power may be another limiting source.

- **Drag Measurements** - Drag experiments consist of passing a current through one of the layers ("drive layer") and measuring the induced voltage drop in the other electrically isolated layer ("drag layer"). Upon entering the vicinity of ν_T=1 state it is found that both the longitudinal $\rho_{drive,xx}$ and $\rho_{drag,xx}$ minima deepen, tending toward zero, and the transverse component $\rho_{drive,xy}$ surprisingly drops down from the expected $\sim 2h/e^2$ to a quantization plateau of h/e^2. More surprisingly still is the sudden massive increase of the essentially zero Hall drag $\rho_{drag,xy}$ to a quantized value of h/e^2! This is claimed by theory to be an indirect signature of the exciton condensate [10, 11, 12, 13] and was first observed by Kellogg et al. [4] where $\rho_{drag,xy}$ was found to be precisely quantized to h/e^2= 25,813 Ω to within about five parts in 10^4.

  The sign of the drag voltage $V_{drag,xx}$ is opposite in direction to $V_{drive,xx}$ in the current carrying layer which is a reflection of the force balancing due to the constraint that no current is allowed to flow in the drag layer [4] and which is commonly seen in drag studies of weakly correlated bilayer electron systems [84, 87]. Unlike the longitudinal drag voltage $V_{drag,xx}$ the transverse voltage $V_{drag,xy}$ is not opposite in direction to $V_{drive,xx}$ and is claimed to be a reflection of the symmetric charged quasi-particle current of the ν_T=1 state.

- **Counter-flow Measurements** - The asymmetric current configuration is tested for both the 17/12.4/17 (d040114b-100) and 19/9.6/19 (d041007c-143) samples by passing two

oppositely directed currents of equal magnitude through the two layers. For matched layer electron densities and for d/ℓ_B below a critical ratio, the ν_T=1 state shows a pronounced minimum in ρ_{xx} while ρ_{xy} drops approximately to zero. Decreasing the d/ℓ_B ratio leads to a further deepening of the ρ_{xx} minimum and a widening of the zero in ρ_{xy}. Indeed, as previously observed [5, 6, 7], both the longitudinal and the Hall voltages in the layers tend to zero at the lowest experimental temperatures. Away from ν_T=1, the traces show Shubnikov-de Haas oscillations of a single layer. At temperatures above 200 mK, the minimum in ρ_{xx} and the zero in ρ_{xy} have disappeared. The amazing disappearance of ρ_{xy} is credited to the formation of neutral excitons. Here the current is strictly carried by charge neutral interlayer excitons which are unaffected by the perpendicular magnetic field.

- **Layer Current Imbalances** - The ν_T=1 Hall voltage, V_{xy} is measured as the layer currents are varied through the parallel, drag, counter-flow and all other intermediate configurations. Due to the strongly coupled nature of the ν_T=1 state, it is found that any net current $I_{net}= I_L - I_U$, where I_U and I_L are the upper and lower layer currents, respectively, will lead to a Hall resistance that is quantized at h/e^2. Even around the vicinity of the claimed counter-flow superfluidic exciton case no deviation from the linear Hall voltage V_{xy} data is detected to within experimental limits. Since there is zero net current in the counter-flow case, a zero Hall voltage will be produced, however V_{xy}/I_{net} remains quantized to h/e^2.

- **Activated Transport at Balanced Electron Layer Densities** - Activation energies ($\Delta_{\nu=1}$) of the ν_T=1 state are obtained from temperature dependent measurements of the various resistivity components for both the 17/12.4/17 (d040114b-100) and 19/9.6/19 (d041007c-143) samples. In all cases the activation energies show a monotonous increase with decreasing d/ℓ_B below a certain $d/\ell_{B,crit}$ which is ~ 1.65 for the 17 nm sample and ~ 1.70 for the 19 nm sample. These $d/\ell_{B,crit}$ values are smaller than the value of ~ 1.83 reported previously [4,5] and it could possibly be due to our slightly lower mobilities or our smaller interlayer tunneling. The activation energies for the 19 sample are approximately twice as large as seen in the 17 nm sample. This is quite surprising since the effective center-to-center QW spacing for the 17 nm and 19 nm samples are approximately the same (29.4 nm and 28.6 nm, respectively) leading one to expect similar $\Delta_{\nu=1}$ vs. $d/\ell_{B,crit}$ behavior. Also for the 19 nm sample, a saturation of $\Delta_{\nu=1}$ for d/ℓ_B below ~ 1.42 can be seen and may indicate a fully developed ν_T=1 state. For the 17/12.4/17 (d040114b-100) we have determined activation energies for transport in the balanced ν_T=1 state over a wide range of the coupling parameter d/ℓ_B for both the drag and counter-flow configurations. The activation energies obtained in the different configurations are approximately equal and increase monotonously with increasing coupling below d/l_B=1.64.

- **Phase Diagrams of the** ν_T**=1 State** - A phase diagram between the weakly coupled
  (ν_U=1/2, ν_L=1/2) phase and the strongly coupled ν_T=1 phase of the ν_T=1 state is exper-
  imentally made as a function of d/ℓ_B vs. imbalance Δn ($\equiv [n_L\text{-}n_U]/n_T$) between -0.15
  and $+0.15$ for the 17/12.4/17 (d040114b-100) sample. In the drag configuration, phase
  diagrams of $\rho_{drive,xx}$, $\rho_{drive,xy}$, $\rho_{drag,xx}$ and $\rho_{drag,xy}$ are obtained. At higher d/ℓ_B values
  the Hall drag signal is essentially zero and the Hall drive $\rho_{drive,xy}$ contour plot goes to
  $\approx 2h/e^2$ signifying two completely independent phases at ν=1/2. Moving to lower d/ℓ_B
  values with balanced densities, a phase transition from the weakly coupled phase to the
  strongly coupled ν_T=1 phase is seen to occur at $d/\ell_B \approx 1.65$. This is in full agreement
  with the $d/\ell_{B,crit}$ ratio obtained from activation energy $\Delta_{\nu=1}$ vs. d/ℓ_B measurements.

  Upon crossing this phase boundary, the ν_T=1 phase quickly strengthens with decreasing
  d/ℓ_B and the transverse resistivities of both $\rho_{drive,xy}$ and $\rho_{drag,xy}$ reach a quantized value
  of h/e^2. Moving away from the balanced electron density case towards imbalanced elec-
  tron layer densities, Coulomb drag measurements reveal that small interlayer imbalances
  lead to strengthening of the excitonic phase. This is particulary apparent in the $\rho_{drag,xy}$
  data where, even if one is not initially in the strongly correlated phase, it is possible to in-
  duce the ν_T=1 phase by imbalancing the system. With imbalance, the phase boundary of
  the drag measurements and the Hall resistance of the drive layer is found to be symmetric
  around zero imbalance and to fit a quadratic function. This symmetric behaviour of the
  phase boundary has also been seen by Spielman et al. [95] to occur in both tunneling and
  Hall drag experiments. Joglekar and MacDonald [101] have been able to account for the
  stability of the ν_T=1 exciton state against charge imbalance using a Hartree-Fock mean-
  field theory approach where the concept of a magneto-roton minimum in the collective
  mode phase plays an important role in the strength of the interlayer coherent phase. Not
  predicted or explained by theory is the unusual asymmetric behavior of the longitudinal
  drive ρ_{xx} resistivity around imbalance. Here negative imbalances (removing electrons
  from the drive layer) leads to an enormous increase in the resistivity, whereas positive
  imbalances (increasing the drive layer density) greatly strengthens the ν_T=1 phase! This
  behavior is completely unexpected and is the main finding of this work. As of yet there
  has not been any theoretical models accounting for this effect.

- **Activated Transport with Imbalance** - In the symmetrically imbalanced ν_T=1 state, an
  asymmetry in the activation energies of the longitudinal resistances of the separate layers
  is observed for both drag and counter-flow configurations for the 17/12.4/17 (d040114b-
  100) sample. In each layer, this activation energy increases approximately linearly with
  increasing the density of the respective layer. It indicates that the measured activation
  energies neither reflect the condensation energy of the excitonic state nor the binding
  energy of the excitons, both of which should be independent on whether it is measured in

the upper layer or in the lower layer. Instead, it implies that the activation energy reflects a gap to charge-excitations in the *separate* layers that form the bilayer condensate and that the excitation spectrum of a layer is substantially different for positive and negative imbalance. As with the $\Delta_{\nu=1}$ vs. d/ℓ_B in Fig. 6.10, we find with imbalance the activation energies obtained in the drag and counter-flow configurations are again approximately equal.

- **The ν_T=1 Step-Up DC Transformer** - The ν_T=1 quantized Hall drag of h/e^2 is used to construct a ν_T=1 step-up DC transformer. Upon separating the upper 2DES into two regions through the use of a finger gate, it is found that in the ν_T=1 state the induced Hall drag voltage in the secondary layer (V_2) can be stepped up to approximately $V_2 = 2I_1h/e^2$ where I_1 is a current sent through the primary layer. Analysis of the current flows and voltage drops in the primary layer is nontrivial due the mixture of coupled ν_T=1 regions separated by small ν=1/2 single layer regions and contact resistances. The question whether the secondary output voltage, V_2 can be made to be larger than the primary input voltage, V_1 requires further investigation.

Bibliography

[1] J. M. Blatt, K. W. Boer and W. Brandt, Phys. Rev. **126**, 1691 (1962).

[2] L. V. Keldysh and Y. V. Kopaev, Fiz. Tverd. Tela. **6**, 2781 (1964).

[3] I. B. Spielman, J. P. Eisenstein, L. N. Pfeiffer and K. W. West, Phys. Rev. Lett. **84**, 5808 (2000).

[4] M. Kellogg, I. B. Spielman, J. P. Eisenstein, L. N. Pfeiffer and K. W. West, Phys. Rev. Lett. **88**, 126804 (2002).

[5] M. Kellogg, J. P. Eisenstein, L. N. Pfeiffer and K. W. West, Phys. Rev. Lett. **93**, 36801 (2004).

[6] E. Tutuc, M. Shayegan and D. Huse, Phys. Rev. Lett. **93**, 36802 (2004).

[7] R. Wiersma, J. Lok, S. Kraus, W. Dietsche, K. von Klitzing, D. Schuh, M. Bichler, H.-P. Tranitz and W. Wegscheider, Phys. Rev. Lett. **93**, 266805 (2004).

[8] J. P. Eisenstein, L. N. Pfeiffer and K. W. West, Appl. Phys. Lett. **57**, 2324 (1990).

[9] H. Rubel, A. Fisher, W. Dietsche, K. von Klitzing and K. Eberl, Mater. Sci. Eng. **51**, 207 (1998).

[10] S. R. Renn, Phys. Rev. Lett. **68**, 658 (1992).

[11] J. M. Duan, Euro. Phys. Lett. **29**, 489 (1995).

[12] K. Yang, Phys. Rev. B **58**, R4246 (1998).

[13] K. Yang and A. H. MacDonald, Phys. Rev. B **63**, 73301 (2001).

[14] S. M. Girvin, Phys. Scr. **T102**, 112 (2002).

[15] B. I. Halperin, A. Stern and S. M. Girvin, Phys. Rev. B **67**, 235313 (2003).

[16] K. v. Klitzing, G. Dorda and M. Pepper, Phys. Rev. Lett. **45**, 494 (1980).

[17] A. P. Balachandran, A. Momen and L. Chandar, Nuclear Physics B **461**, 581 (1996).

[18] M. Greiter, Journal of Modern Physics A **13**, 1293 (1998).

[19] M. Fabinger, Journal High Energy Physics **5**, 37 (2002).

[20] D. C. Tsui, H. L. Störmer and A. C. Gossard, Phys. Rev. Lett. **48**, 1559 (1982).

[21] H. L. Störmer, Rev. Mod. Phys. **71**, 875 (1999).

[22] D. C. Tsui, Rev. Mod. Phys. **71**, 891 (1999).

[23] R. B. Laughlin, Phys. Rev. Lett. **50**, 1395 (1983).

[24] R. B. Laughlin, Rev. Mod. Phys. **71**, 863 (1999).

[25] B.I. Halperin, Helv. Phys. Acta **56**, 75 (1983).

[26] K. Y. et al., Phys. Rev. Lett. **51**, 5138 (1995).

[27] H. Fertig, Phys. Rev. B **40**, 1087 (1989).

[28] A. H. MacDonald, Physica B **298**, 129 (2001).

[29] A. H. MacDonald, A. A. B. Y. N. Joglekar and E. Rossi, Phys. of Semicond. **171**, 29 (2002).

[30] S. Conti, G. Vignale and A. H. MacDonald, Phys. Rev. B **57**, 6846 (1998).

[31] T. Ando, A. B. Fowler and F. Stern, Rev. Mod. Phys. **54**, 437 (1982).

[32] J. P. Eisenstein, K. B. Cooper, L. N. Pfeiffer and K. W. West, Phys. Rev. Lett. **88**, 76801 (2002).

[33] H. L. Störmer, Surf. Science **132**, 519 (1983).

[34] L. L. Chang and K. Ploog, *Molecular Beam Epitaxy and Heterostructures*.

[35] Gerald B. Stringfellow, *Organometallic Vapor Phase Epitaxy*, (Academic Press, 1999).

[36] P. Drude, Ann. Phys. **3**, 369 (1900).

[37] L. Landau, JETP Lett. **30**, 1058 (1956).

[38] J. Mravlje, *Anyons in the Fractional Quantum Hall Effect*, Seminar Course Book, 2005.

[39] B. N. Taylor, IEEE Trans. Instrum. Meas. **38**, 164 (1989).

[40] H. Bachmair, E. Göbel, G. Hein, J. Melcher., B. Schumacher, J. Schurr, L. Schweitzer and P. Warnecke, Physica E **20**, 14 (2003).

[41] M. Büttiker, Phys. Rev. B **38**, 9375 (1988).

[42] L. Shubnikov and W. J. de Haas, Leiden Comm. **207a,c,d,210a**, (1930).

[43] *The Quantum Hall Effect, 2nd Ed.*, edited by Richard E. Prange and Steven M. Girvin, (Springer-Verlay, Berlin, New York, 1995).

[44] S. M. Girvin, Phys. Rev. B **29**, 6012 (1984).

[45] G. Murthy and R. Shankar, Rev. Mod. Phys. **75**, 1101 (2003).

[46] R. de Picciotto, M. Reznikov, M. Heiblum, V. Umansky, G. Bunin and D. Mahalu, Nature **389**, 162 (1997).

[47] V. Goldman and B. Su, Science **267**, 1010 (1995).

[48] J. Jain, Phys. Rev. Lett. **63**, 199 (1989).

[49] J. Jain, Science **266**, 1199 (1990).

[50] J. H. Smet, D. Weiss, R. H. Blick, G. Lütjering, K. von Klitzing, R. Fleischman, T. Geisel and G. Weimann, Phys. Rev. Lett. **77**, 2272 (1996).

[51] N. Read, Physica B **298**, 121 (2001).

[52] J. Göres, Ph.D. thesis, Max-Planck-Institut für Festkörperforschung, Stuttgart, 2004.

[53] S. H. Simon, Solid State Commun. **134**, 81 (2005).

[54] S. Q. Murphy, J. P. Eisenstein, G. S. Boebinger, L. N. Pfeiffer and K. W. West, Phys. Rev. Lett. **72**, 728 (1994).

[55] J. Hu and A. H. MacDonald, Phys. Rev. B **46**, 12554 (1992).

[56] D. Yoshioka, A. H. MacDonald and S. Girvin, Phys. Rev. B **39**, 1932 (1989).

[57] O. I. Stern, Ph.D. Thesis, Max-Planck-Institute, Stuttgart, 2005.

[58] X. G. Wen and A. Zee, Phys. Rev. Lett. **69**, 1811 (1992).

[59] Z. F. Ezawa and A. Iwazaki, Phys. Rev. B **47**, 7295 (1993).

[60] A. Stern, S. M. Girvin, A. H. MacDonald and N. Ma, Phys. Rev. Lett. **86**, 1829 (2001).

[61] L. Balents and L. Radzihovsky, Phys. Rev. Lett. **86**, 1825 (2001).

[62] I. B. Spielman, J. P. Eisenstein, L. N. Pfeiffer and K. W. West, Phys. Rev. Lett. **87**, 36803 (2001).

[63] S. D. Sarma and A. Pinczuk, *Perspective in Quantum Hall Effects* (John Wiley and Sons, Inc., New York, New York, USA, 1997).

[64] J. M. Kosterlitz and D. J. Thouless, J. Phys. C **6**, 1181 (1973).

[65] L. V. Butov, C. W. Lai, A. L. Ivanov, A. C. Gossard and D. S. Chemla, Nature **417**, 47 (2002).

[66] L. V. Butov, Phys. Rev. Lett. **73**, 304 (1994).

[67] L. V. Butov, A. C. Gossard and D. S. Chemla, Nature **418**, 751 (2002).

[68] D. S. S. Denev, Y. Liu, L. N. Pfeiffer and K. W. West, Nature **418**, 754 (2002).

[69] C. W. Lai, J. Zoch, A. C. Gossard and D. S. Chemla, Science **303**, 503 (2004).

[70] Gregory L. Snider, University of Notre Dame, Free Poisson-Schrödinger Solver, www.nd.edu/ gsnider.

[71] L. Pfeiffer, E. F. Schubert, K. W. West and C. W. Magee, Appl. Phys. Lett. **58**, 2258 (1991).

[72] N. Braslau, J. B. Gunn and J. L. Staples, Solid State Electron. **10**, 381 (1967).

[73] H. Fronius, A. Fisher and K. Ploog, United States Patent **4732648**, (1988).

[74] D. Vion, P. F. Orfila, P. Joyez, D. Esteve and M. H. Devoret, J. Appl. Phys. **77**, 2519 (1995).

[75] S. Q. Murphy, J. P. Eisenstein, L. N. Pfeiffer and K. W. West, Phys. Rev. B **52**, 14825 (1995).

[76] R. C. Ashoori, J. A. Lebens, N. P. Bigelow and R. H. Silsbee, Phys. Rev. Lett. **64**, 681 (1990).

[77] J. P. Eisenstein, L. N. Pfeiffer and K. W. West, Phys. Rev. Lett. **69**, 3804 (1992).

[78] K. M. Brown, N. Turner, J. T. Nicholls, E. H. Linfield, M. Pepper, D. A. Ritchie and G. A. C. Jones, Phys. Rev. B **50**, 15465 (1994).

[79] J. G. S. Lok, A. K. Geim, J. C. Maan, L. Eaves, A. Nogaret, P. C. Main and M. Henini, Phys. Rev. B **56**, 1053 (1997).

[80] E. Rossi, A. S. Nunez and A. H. MacDonald, Interlayer Transport in Bilayer Quantum Hall Systems, 2005.

[81] J. P. Eisenstein, Solid State Comm. **127**, 123 (2003).

[82] A. S. S. D. Sarma, M. P. A. Fisher and S. M. Girvin, Phys. Rev. Lett. **84**, 139 (2000).

[83] Y. N. Joglekar and A. H. MacDonald, Phys. Rev. Lett. **87**, 196802 (2001).

[84] T. J. Gramila, J. P. Eisenstein, A. H. MacDonald, L. N. Pfeiffer and K. W. West, Phys. Rev. Lett. **66**, 1216 (1991).

[85] A. P. Jauho and H. Smith, Phys. Rev. B **47**, 4420 (1993).

[86] U. Sivan, P. M. Solomon and H. Shtrikman, Phys. Rev. Lett. **68**, 1196 (1992).

[87] M. P. Lilly, J. P. Eisenstein, L. N. Pfeiffer and K. W. West, Phys. Rev. Lett. **80**, 1714 (1998).

[88] J. G. S. Lok, S. Kraus, M. Pohlt, W. Dietsche, K. von Klitzing, W. Wegscheider and M. Bichler, Phys. Rev. B **63**, 41305 (2001).

[89] K. Moon, H. Mori, K. Yang, S. Girvin, A. MacDonald, L. Zheng, D. Yoshioka and S.-C. Zhang, Phys. Rev. B **51**, 5138 (1995).

[90] F. Zhou and Y. B. Kim, Phys. Rev. B **59**, R7825 (1999).

[91] B. Y. K. Hu, Phys. Scr. T **69**, 170 (1997).

[92] F. von Oppen, S. H. Simon and A. Stern, Phys. Rev. Lett. **87**, 106803 (2001).

[93] M. Abolfath, A. H. MacDonald and L. Radzihovsky, Phys. Rev. B **68**, 155318 (2003).

[94] M. Kellogg, Ph.D. thesis, California Institute of Technology, Pasadena, 2005.

[95] I. B. Spielman, M. Kellogg, J. P. Eisenstein, L. N. Pfeiffer and K. W. West, Phys. Rev. B **70**, R081303 (2004).

[96] N. E. Bonesteel, I. A. McDonald and C. Nayak, Phys. Rev. Lett. **77**, 3009 (1996).

[97] Y. B. Kim, C. Nayak, E. Demler, N. Read and S. D. Sarma, Phys. Rev. B **63**, 205315 (2001).

[98] A. Stern and B. I. Halprein, Phys. Rev. Lett. **88**, 106801 (2002).

[99] E. Papa, J. Schliemann, A. H. MacDonald and M. P. A. Fisher, Phys. Rev. B **61**, 115330 (2003).

[100] S. H. Simon, E. H. Rezayi and M. V. Milovanovic, Phys. Rev. Lett. **91**, 046803 (2003).

[101] Y. N. Joglekar and A. H. MacDonald, Phys. Rev. B **65**, 235319 (2002).

[102] E. Tutuc, S. Melinte, E. P. D. Poortere, R. Pillarisetty and M. Shayegan, Phys. Rev. Lett. **91**, 76802 (2003).

[103] R. Wiersma, J. Lok, S. Kraus, W. Dietsche, K. von Klitzing, D. Schuh, M. Bichler, H.-P. Tranitz and W. Wegscheider, Physica E **in press**, (2005).

Acknowledgements

I would like to thank the following people who have helped in contributing to this work.

- Klaus von Klitzing for giving me the opportunity to work on a truly fascinating project and for keeping me on my toes with intriguing questions and discussions.

- Werner Dietsche for taking the risk of accepting a Canadian in his group. Also for his support and guidance in helping to make this thesis a success.

- Sjoerd Lok for teaching me the art of two-dimensional bilayer systems and for his many insights over the years.

- Rolf Haug for acting as a member on my defense committee and for showing an interest in my work.

- Regensberg MBE Group: W. Wegscheider and P.-T Trantiz for the MBE growth of bilayer wafers capable of showing the ν_T=1 state.

- München MBE Group: M. Bichler and D.Schuh for providing MBE assistance with the design of high quality bilayer systems.

- Stuttgart MBE Group: Werner Dietsche, Sjoerd Lok, Mark Lynass and F. Schwerd for growth of the initial highly Si-doped layer used for constructing back gates.

- The Dietsche Team: Dimitri Dini, Stefan Kraus, Sjoerd Lok, Mark Lynass, Werner Rauscher, Omar Stern, and Lars Tiemann for making my life at MPI a fun and enjoyable experience.

- Jürgen Weis for providing technical help and equipment.

- The Clean Room Team: Thomas Reindl, Monika Riek, Ulli Waizmann for putting up with me in the clean room.

- The vK group for interesting discussions, tea, and a lot of birthday cake. It was a pleasure!

Lebenslauf

Name:	Rodney David Wiersma
Geburtsdatum:	09.06.1976
Geburtsort:	Edmonton, Kanada
Familienstand:	ledig

1995-1996	Advanced High School Diploma with Honors, Bev Facey Community High School, Sherwood Park, Kanada.
1996-1999	Honors Bachelors in Physics, University of Alberta, Edmonton, Kanada.
1999-2002	Masters in Physics, Simon Fraser University, Vancouver, Kanada.
seit 06/2002-	Anfertigung der vorliegenden Dissertation, Max-Planck-Institut für Festkörperforschung, Stuttgart, Deutschland.